MONTE CARLO MODELING OF NON-LOCAL ELECTRON CONDUCTION IN HIGH ENERGY DENSITY PLASMAS

by

Jeffrey John Chenhall

A dissertation submitted in partial fulfillment of the requirements for the degree of

Doctor of Philosophy

(Nuclear Engineering and Engineering Physics)

at the

UNIVERSITY OF WISCONSIN-MADISON

2017

Date of final oral examination: July 26, 2017

The disseration is approved by the following members of the Final Oral Committee:

Gregory A. Moses, Harvey D. Spangler Professor of Nuclear Engineering, Engineering Physics (Advisor)

Douglas L. Henderson, Professor and Department Chair, Engineering Physics

Carl R. Sovinec, Professor, Engineering Physics

Paul P. Wilson, Professor, Engineering Physics

David T. Anderson, Professor, Electrical & Computer Engineering

Abstract

The implicit SNB (iSNB) non-local multigroup thermal electron conduction method of Schurtz et. al. [Phys. Plasmas 7, 4238 (2000)] and Cao et. al. [Phys. Plasmas 22, 082308 (2015)] is adapted into an electron thermal transport Monte Carlo (ETTMC) transport method to better model higher order angular and long mean free path non-local effects. The ETTMC model is used to simulate the electron thermal transport within inertial confinement fusion (ICF) type problems. The new model aims to improve upon the currently used iSNB, in particular by using finite particle ranges in comparison to the exponential solution of a diffusion method and by improved higher order angular modeling. The new method has been implemented in the 1D LILAC and 2D DRACO multiphysics production codes developed by the University of Rochester Laboratory for Laser Energetics. The ETTMC model is compared to iSNB for several direct drive ICF type simulations: Omega shot 60303 a shock timing experiment, Omega shot 59529 a shock timing experiment, Omega shot 68951 a cryogenic target implosion and a NIF polar direct drive phase plate design. Overall, the ETTMC method performs at least as well as the iSNB method and predicts lower preheating ahead of the shock fronts. This research was supported by University of Rochester Laboratory for Laser Energetics, Sandia National Laboratories and the University of Wisconsin-Madison Foundation.

Acknowledgments

I would like thank several people for their support and guidance throughout the duration of this project. First, I thank my advisor Greg Moses for guiding me along my path to getting a graduate degree. Next, I'd like to thank the University of Rochester Laboratory for Laser Energetics, which provided support for my research assistanceship during my first two years of grad school and their continued support in electron thermal transport modeling. Sandia National Laboratories currently is supporting my research through a fellowship and I thank my Sandia mentor Len Lorence for his contribution to the project. My fellow grad students, Duc Cao, Ryan Sacks, and Ryan Wollaeger, have been great friends and were a great resource with their own experiences in their individual research projects. Finally, I'd like to thank my parents, James and Marion Chenhall, and brother, Tyler Chenhall, for their continued love and support throughout the years.

Table of Contents

List of Figures

Chapter 1

Introduction

Nuclear fusion reactions are what stars use as their power source and are the predominate generator of energy in the galaxy. Fusion has the highest energy per fuel mass and is an order of magnitude higher specific yield than fission. Additionally, fusion power sources here on earth would benefit from lack of proliferation concerns that have limited the fission industry.

1.1 Fusion

While fission takes place with a neutral neutron being absorbed by a nucleus, fusion occurs between two charged particles. As such, additional activation energy must be supplied to the reactant nuclei in order to overcome the Coulomb potential and fuse. After an initial input of energy to trigger the fusion process, the released energy can be used to heat the reactants if it is sufficiently contained within the system.

Candidate isotopes for fusion power generation are chosen such that the charges of the nuclei are low to minimize coulombic repulsion and thus activation energy. While stars rely on proton-proton (PP) fusion as the start of their fusion cycle, the PP cross section is several orders of magnitude lower than other low atomic number candidates. The next two candidate reactions are the deuteron-deuteron (DD) and the deuteron-triton (DT) reactions. The DT reaction is preferred as its cross section peaks at lower energy and it releases more energy (Fig. 1.1). To reach ideal fusion conditions, the fuel mixture must be raised to high density and temperatures of several keV [1][2][3].

$$ {}^{1}_{1}p + {}^{1}_{1}p \rightarrow {}^{2}_{1}D + e^{+} + \nu_e \qquad \text{(0.42 MeV)} \tag{1.1a} $$

$$ {}^{2}_{1}D + {}^{2}_{1}D \rightarrow {}^{3}_{2}He + {}^{1}_{0}n \qquad \text{(3.27 MeV)} \quad \text{(50\%)} \tag{1.1b} $$

$$ \rightarrow \ {}^{3}_{1}T + {}^{1}_{1}p \qquad \text{(4.04 MeV)} \quad \text{(50\%)} \tag{1.1c} $$

$$ {}^{2}_{1}D + {}^{3}_{1}T \rightarrow {}^{4}_{2}He + {}^{1}_{0}n \qquad \text{(17.6 MeV)} \tag{1.1d} $$

$$ {}^{2}_{1}D + {}^{3}_{2}He \rightarrow {}^{4}_{2}He + {}^{1}_{1}p \qquad \text{(18.4 MeV)} \tag{1.1e} $$

$$ {}^{1}_{1}p + {}^{11}_{5}B \rightarrow 3 \cdot {}^{4}_{2}He \qquad \text{(8.68 MeV)} \tag{1.1f} $$

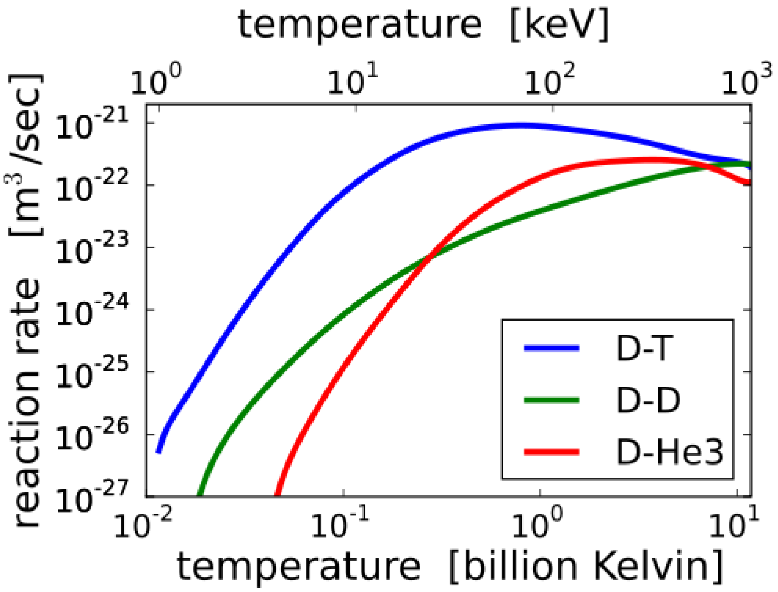

FIGURE 1.1: *This figure shows the fusion cross sections for DD, DT, and D-He3 reactions [Image from [4]].*

In order to sustain the fusion reaction, the plasma must be held together long enough for reactions to occur. In a DT plasma, after the initial energy input, the alpha particle fusion products need to deposit their energy within the plasma in order to provide the activation energy for subsequent reactions. The 14 MeV neutrons produced by DT fusion are neutral consequently they have a long enough collision length to escape the fusion plasma without depositing energy. The rate of this energy transfer between products and reactants increases with plasma density due to the increases in particle collision rates. The required high temperature and densities of the fusion plasma presents a series of confinement challenges since this state is highly unstable. Stars have immense mass and their gravitational forces are sufficient to counterbalance the pressures needed to contain the fusion plasma. For terrestrial fusion application, however, different methods of confinement are necessary.

The two main branches of fusion confinement study are Magnetic Confinement Fusion (MCF) and Inertial Confinement Fusion (ICF). MCF attempts to confine the fusion plasma by application of external electromagnetic fields, which act to control the flow of the plasma. The most prevalent design involves toroidal tokamak reactors whose geometry is conducive to the looping shape of magnetic field lines. Technical challenges with this approach include sustained generation of high Tesla magnetic fields, management of plasma instabilities, and development of robust materials for the reactor structures. MCF aims to establish confinement times of 100's of seconds.

1.2 Inertial Confinement Fusion

ICF achieves fusion by imparting inward momentum on a spherical target of fusion fuel. Beams are used to add energy to the outer shell layer of the target that propels mass inwards via the rocket effect. A shock travels through the target increasing the density and temperature in the center. This creates a hot spot in the center of the target, which acts as a 'spark plug' to ignite the fusion reaction. The fusion propagates outward via alpha particle deposition in the fuel until the target disassembles itself.

The two main ways of achieving ICF are direct and indirect drive. Direct drive is achieved by directly illuminating the fusion target with lasers in a symmetric fashion. The Omega Laser at the University of Rochester Laboratory for Laser Energetics (LLE) is the primary laser system for studying direct drive in the United States. Indirect drive is achieved by aiming the lasers at a hohlraum, which then reemits x-rays in order to illuminate the fuel target. The hohlraum consists of a cylindrical shell of high-Z material (Fig. 1.2). The hohlraum is used so that a more uniform illumination of the target can be achieved from the emitted x-rays in comparison to the finite number of lasers. The National Ignition Facility at Lawrence Livermore National Laboratory (LLNL) in Livermore California is the most powerful laser system and is used to study indirect drive (Fig. 1.3). A downside to using an indirect drive approach is that a lower proportion of the laser energy is transferred to the fuel due to the beams interacting with the hohlraum first. Another downside is that cross beam energy transfer (CBET) can occur between laser beams due to the plasma generated within the hohlraum. CBET can affect the symmetry of laser implosion, which causes seeding of instabilities and consequently a reduction in target yield. In both direct and indirect drive, the fusion target consists of an outer plastic ablator, which blows off during the illumination in order to trigger an inertial rocket effect. The next layers are a layer of DT ice and an inner layer of gaseous DT shown in Fig. 1.2.

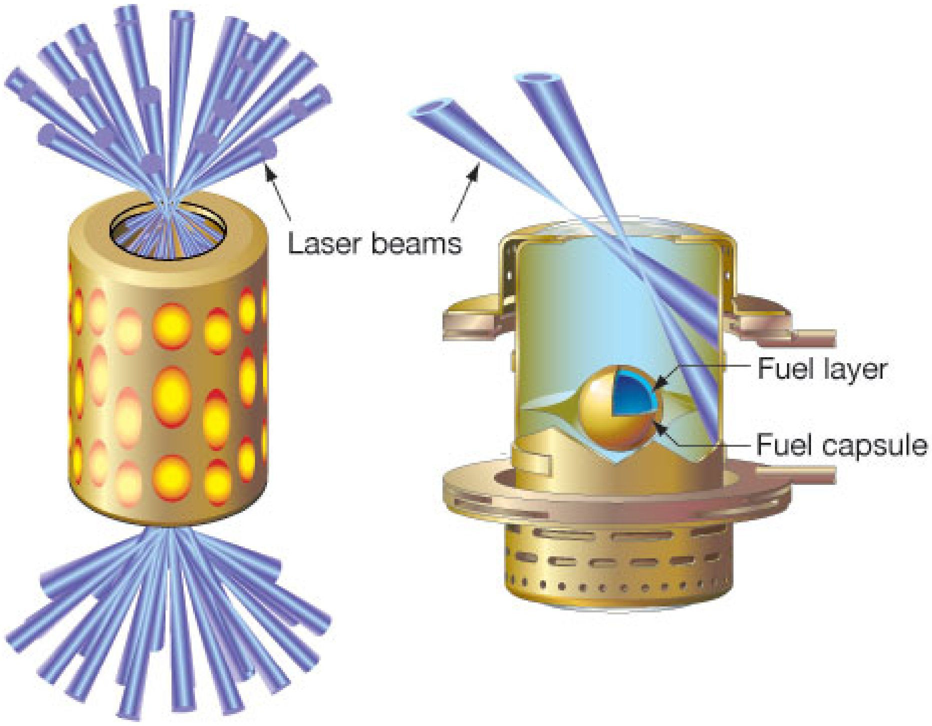

FIGURE 1.2: *Indirect drive in a hohlraum [Image from LLNL [5]].*

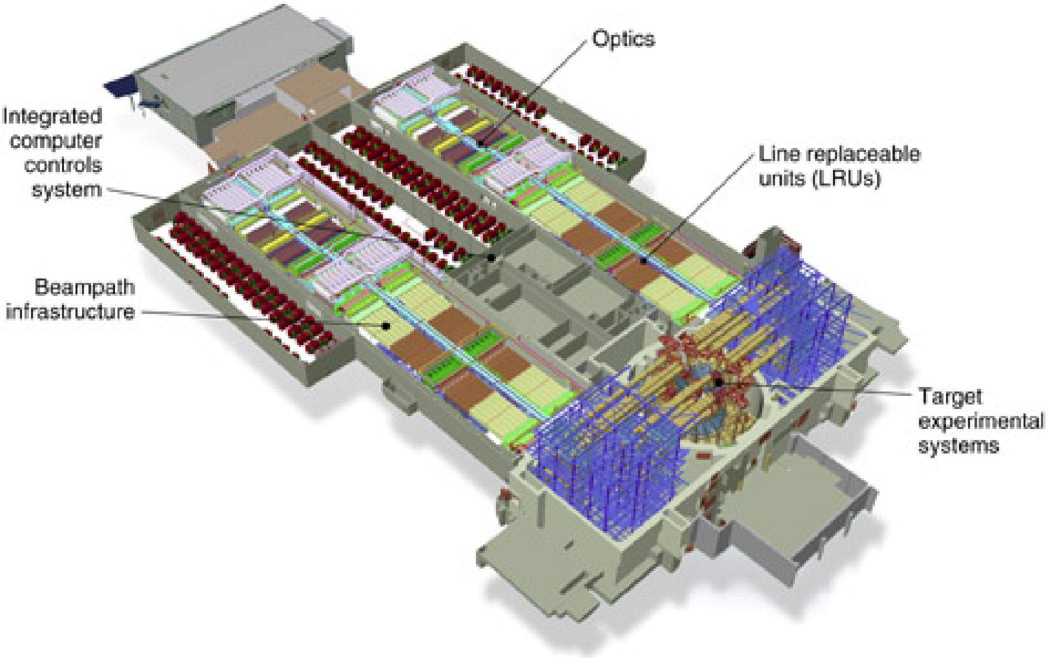

FIGURE 1.3: *Layout of the National Ignition Facility [Image from LLNL [6]].*

During an ICF implosion both target illumination symmetry and isentropic compression are desired. Symmetry is important due to asymmetry seeding fluid instabilities, which can cause mixing of the target layers bringing higher-Z material into the center to quench the fusion reaction. In order to have near adiabatic compression, shaped laser pickets are used followed by a main drive. These pickets are time and energy tuned in order for their produced shockwaves to meet in the center of the target, creating a hot spot. The target then burns outward from the hot spot until disassembly.

An ICF implosion proceeds as follows (Fig. 1.4). First, a series of laser pulses (pickets) illuminate the target in a spherical manner. The absorbed laser energy ablates material from the outer plastic layer of the target, which then via the rocket effect propels energy and matter towards the center of the target. Next, the main drive pulse of the laser further compresses the target, further heating the fuel. The generated shockwaves meet in the center of the target, due to careful tuning of the energy and timing of the laser pulses, to create a hot spot with conditions sufficient to ignite fusion reactions. The fusion reactions produce both alpha particles and neutrons with the alpha particles depositing their energy within the fuel and the neutrons escaping from the system. The alpha particle deposition provides the energy for subsequent fusion reactions and the target burns outwards from the central hot spot until disassembly.

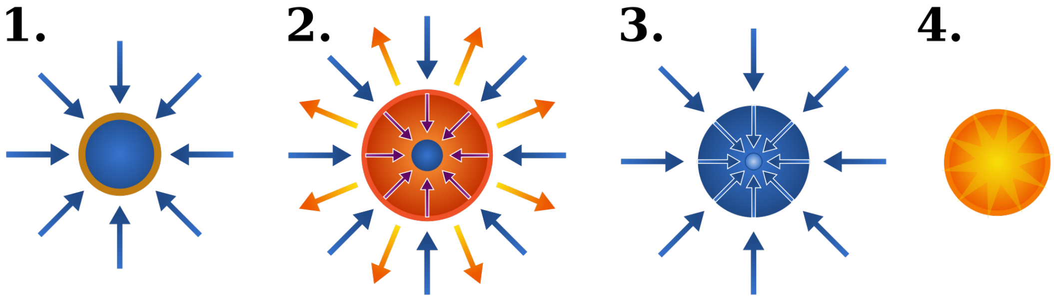

FIGURE 1.4: *Step 1: Lasers illuminate the target. Step 2: Material ablates off the outer surface of the target propelling a shockwave inward via the rocket effect. Step 3: Main drive pulse further compresses the target. Step 4: shockwaves meet in the middle creating a hot spot which ignites the DT fuel [Image from [7]].*

In order to properly time the laser profile sufficiently detailed modeling capabilities are necessary. There are many multi-physics codes being used to study implosion physics, but they often fall short when applied to the high energy shockwaves that travel through the fuel. Modeling these environments, in particular accurately predicting electron thermal conduction, is the primary focus of the remainder of this thesis.

1.3 Thesis Summary

The main purpose of this thesis is to develop and implement an improved method for computing the electron thermal heat flux using Monte Carlo techniques for use in a multi-physics code. Of particular interest is the computation of the heat flux divergence term ($\nabla \cdot \mathbf{Q}$) in the electron temperature hydrodynamics equation:

$$\rho C_v \frac{\partial T_e}{\partial t} = -\nabla \cdot \mathbf{Q} + S_{other} \tag{1.2}$$

where ρ is density, C_v is the specific heat, T_e is the electron temperature, and S_{other} contains all other terms such as the electron-ion coupling and compression heating terms.

This thesis is broken into several chapters. Chapter 2 provides a summary of the relevant background literature on electron thermal conduction modeling. Chapter 3 delves into the theoretical basis for Chenhall's thesis work on developing the electron thermal transport Monte Carlo (ETTMC) model. Chenhall has implemented the ETTMC model into LLE's 1D LILAC and 2D DRACO multiphysics codes. Chapter 4 presents simulation results and comparisons of the new ETTMC model to the previously implemented iSNB and Goncharov models. Finally the appendices delve into some early work done on the thesis project. Appendix A deals with some initial work done in adapting MC methods from radiation transport techniques to electron thermal transport. Results on a 1D MC solution method to the iSNB diffusion method are presented. Appendix B deals with some work on an extension to the iSNB diffusion method via a higher angular order Legendre expansion (simplified P3).

Chapter 2

Electron Thermal Transport Background

2.1 Non-local Electron Transport

The transport of heat throughout the problem domain is important to the study of ICF problems. The Spitzer Harm (SH) heat flux result for a plasma arises from a first order expansion of the electron distribution function $f(\mathbf{r}, v, \mathbf{\Omega}) = f_0(\mathbf{r}, v) + 3\mathbf{\Omega} \cdot \mathbf{f}_1(\mathbf{r}, v)$ where f_0 is taken to be the Maxwell-Boltzmann distribution [8]. Starting with the Boltzmann transport equation SH derive an expression for the electron heat conduction

$$\mathbf{Q}_{sh} = -K_{sh} \nabla T_e \tag{2.1}$$

$$K_{sh} = 0.4 \frac{\bar{Z}}{\bar{Z} + 0.2 \log(\bar{Z} + 3.44)} \frac{20(2/\pi)^{3/2} k_b^{7/2} T_e^{5/2}}{m_e^{1/2} e^4 \bar{Z} \log \Lambda} \tag{2.2}$$

where T_e is the electron temperature, $\bar{Z}$ is the average ion charge, k_b is the Boltzmann constant, e and m_e are the electron charge and mass, and $\log\Lambda$ is the Coulomb logarithm. The SH theory is based on the assumption that the electron distribution function is primarily Maxwellian with a small first order correction term. As such, the SH flux is only applicable in regions where the ratio f_1/f_0 is small. This is equivalent to the length scale of the temperature gradient $|T_e/\nabla T_e|$ greatly exceeding the electron mean free path (MFP) length.

Spitzer-Harm theory has a couple of shortcomings particularly when applied to ICF problems. The approximation that the electron distribution function is largely Maxwellian fails in highly transient problems where there is insufficient time for the plasma to equilibrate to the Maxwellian equilibrium solution. In the presence of strong shockwaves, typical of ICF implosions, the heat out ahead of the shockwave (the preheat) is underpredicted and the heat flux magnitude and the speed of the shockwave are overpredicted. The reason for the underprediction of preheating is because high-energy electrons have a greater MFP length than the length scale of the temperature gradient. This allows some of the electrons to stream out of the gradient zone and contribute to the preheating. Since the SH heat flux result depends only upon the local temperature gradient, the high energy electrons remain in the wave front accounting for the underprediction of preheating. Furthermore as the high-energy electrons remain in the wave front the heat flux is overpredicted, which results in the shockwave propagating with too high of a velocity.

Typically, to combat the overprediction of the heat flux magnitude a flux limiter model is used. The heat flux magnitude is capped at a maximum value proportional to the electron thermal velocity via

$$Q_{fl}(\mathbf{r}) = \min|Q_{SH}, \alpha n_e v_{e,th}| \tag{2.3}$$

where α is the flux limiter, n_e is the electron density, and $v_{e,th}$ is the electron thermal velocity

[9]. The flux limiter is a user defined parameter that is commonly set to a value of 0.06 due to agreement with past experimental data. The downside to such a fix up is that the flux limiter parameter is not predictive and fails to address the problem of preheating. Accurate prediction of the preheating is important because the preheating conditions the (typically cold) material ahead of the shock front, which will resultantly affect shock propagation. As such, a higher fidelity non-local model is necessary to properly calculate preheating and improve predictive capability.

2.1.1 Delocalization Kernel

Luciani, Mora and Virmont (LMV) propose a convolution kernel modification to the SH flux to take into account non-local effects near strong temperature gradients [9]. The kernel takes into account the energy dependence of an electron's MFP length and acts to delocalize the SH flux, in essence allowing for higher energy electrons to escape the local temperature gradient. The modification involves convoluting the delocalization kernel with the SH heat flux expression via

$$Q(x) = \int_{-\infty}^{+\infty} W(x,x') Q_{SH}(x') \frac{dx'}{a\lambda_e(x')}, \tag{2.4}$$

$$\lambda_e = (\lambda_{ei}\lambda_{ee})^{1/2} = (Z+1)^{-1/2} \frac{(k_b T_e)^2}{4\pi n_e e^4 \log \Lambda} \tag{2.5}$$

where $Q(x)$ is the non-local heat flux, $W(x,x')$ is the delocalization kernel, λ_e is the electron MFP length, and a is an adjustable parameter with a recommended value of 32. The kernel itself takes the form

$$W(x,x') = \beta \exp(-\tau(x,x')) \tag{2.6}$$

where β is a normalization constant and $\tau(x, x')$ is a measure of optical depth (the number of MFPs) between points x and x' given by

$$\tau(x, y) = \frac{|\int_x^y n_e(z)dz|}{a n_e(y)\lambda_e(y)}. \tag{2.7}$$

For small MFP lengths relative to the temperature gradient length scale the kernel behaves as a delta function and the SH relation is recovered. Generalization to multiple dimensions is achieved by replacing x and x' by $\mathbf{r}$ and $\mathbf{r} + s\mathbf{\Omega}$ respectively and integrating over $\mathbb{R}^3$ via

$$\mathbf{Q}(\mathbf{r}) = \int_{4\pi} \mathbf{\Omega\Omega} d^2\mathbf{\Omega} \int_0^\infty W_0(\mathbf{r}, \mathbf{r} + s\mathbf{\Omega})\mathbf{Q}_{SH}(\mathbf{r} + s\Omega)\frac{ds}{\lambda_e(\mathbf{r} + s\Omega)} \tag{2.8}$$

where W_0 is the 1D kernel. It should be noted that similar work on non-local electron conduction modeling for use in magnetized plasmas has been done by Held, Callen, Hegna, and Sovinec [10][11][12].

2.1.2 Schurtz, Nicolai, and Busquet Model

In their work, Schurtz, Nicolai, and Busquet (SNB) note that the LMV non-local flux looks like the integral solution to a transport equation [13]. SNB define $q(\mathbf{\Omega}, \mathbf{r})$ as the angular flux solution of the linear steady state transport equation

$$\mathbf{\Omega} \cdot \nabla q(\mathbf{\Omega}, \mathbf{r}) + \frac{1}{\lambda(\mathbf{r})} q(\mathbf{\Omega}, \mathbf{r}) = \frac{1}{\lambda(\mathbf{r})} \left(\frac{3}{4\pi} \mathbf{\Omega} \cdot \mathbf{Q}_{SH}(\mathbf{r}) \right). \tag{2.9}$$

where $\lambda(\mathbf{r})$ is the MFP length. Defining the optical depth (the number of MFP's between $\mathbf{r}$ and $\mathbf{r}'$) as

$$\tau(\mathbf{r}, \mathbf{r}') = \int_{\mathbf{r}}^{\mathbf{r}'} \frac{d\mathbf{r}''}{\lambda(\mathbf{r}'')} \tag{2.10}$$

the solution to Eq. (2.9) is

$$q(\boldsymbol{\Omega},\mathbf{r}) = \frac{3}{4\pi}\int_0^\infty e^{-\tau(\mathbf{r},\mathbf{r}-s\boldsymbol{\Omega}')}\boldsymbol{\Omega}\cdot\mathbf{Q}_{SH}(\mathbf{r}-s\boldsymbol{\Omega})\frac{ds}{\lambda(\mathbf{r}-s\Omega)} \tag{2.11}$$

Taking the first angular moment of the angular flux yields the heat flux expression Eq. (2.8) with delocalization kernel

$$W_0(\mathbf{r},\mathbf{r}') = \exp(-\tau(\mathbf{r},\mathbf{r}')). \tag{2.12}$$

Due to differing plasma conditions between an electron's start and end point the delocalization kernel will be non-symmetric. In order to mitigate the computational issues associated with a non-symmetric kernel a multigroup approach is suggested. Since the asymmetry in the kernel is primarily a temperature driven effect, splitting the kernel into energy groups insures that $W_{0,g}(\mathbf{r},\mathbf{r}') \approx W_{0,g}(\mathbf{r}',\mathbf{r})$. By splitting into energy groups Eq. (2.9) becomes

$$\boldsymbol{\Omega}\cdot\nabla q_g(\boldsymbol{\Omega},\mathbf{r}) = \frac{1}{\lambda_g(\mathbf{r})}\left(\frac{3}{4\pi}\boldsymbol{\Omega}\cdot\mathbf{U}_g(\mathbf{r}) - q_g(\boldsymbol{\Omega},\mathbf{r})\right) \tag{2.13}$$

where $\mathbf{U}_g(\mathbf{r})$ is the multigroup source term

$$\mathbf{U}_g = \frac{1}{24}\int_{E_{g-1}/kT}^{E_g/kT}\beta^4 e^{-\beta}d\beta\;\mathbf{Q}_{SH} \tag{2.14}$$

and λ_g is the multigroup MFP

$$\lambda_g = 2(E_{g-1/2}/kT)^2\lambda_e. \tag{2.15}$$

To recover the heat flux, the first angular moment of $q_g(\boldsymbol{\Omega},\mathbf{r})$ is taken and then summed over all energy groups yielding

$$\mathbf{Q}_t(\mathbf{r}) = \sum_g\int_{4\pi}q_g(\boldsymbol{\Omega},\mathbf{r})\boldsymbol{\Omega}d\boldsymbol{\Omega}. \tag{2.16}$$

SNB suggest using a diffusion approximation to solve the transport equation (2.13). Taking the first two angular moments and combining to get a diffusion equation gives

$$\left(\frac{1}{\lambda_g(\mathbf{r})} - \nabla \frac{\lambda_g(\mathbf{r})}{3} \nabla\right) H_g(\mathbf{r}) = -\nabla \cdot \mathbf{U}_g(\mathbf{r}) \tag{2.17}$$

where $H_g(\mathbf{r})$ is the zeroth angular moment of $q_g(\mathbf{\Omega}, \mathbf{r})$. Substituting the first angular moment of Eq. (2.13) into Eq. (2.16), the heat flux solution becomes

$$\mathbf{Q}_{SNB}(\mathbf{r}) = \mathbf{Q}_{SH}(\mathbf{r}) - \sum_g \frac{\lambda_g(\mathbf{r})}{3} \nabla H_g(\mathbf{r}). \tag{2.18}$$

From this form of the heat flux, it is readily apparent that the SNB method produces a correction term to the SH flux. Furthermore the SH result is recovered for small MFP relative to the spatial gradient scale length.

In order to give a physical meaning to the delocalization kernel results, SNB propose an alternative derivation using the steady state Fokker-Planck equation

$$\mathbf{v} \cdot \nabla f - \frac{e\mathbf{E}}{m_e} \cdot \frac{\partial f}{\partial \mathbf{v}} = C(f). \tag{2.19}$$

The equation is expanded using a first order spherical harmonics expansion

$$f(\mathbf{r}, v, \mathbf{\Omega}) = f_0(\mathbf{r}, v) + 3\mathbf{\Omega} \cdot \mathbf{f}_1(\mathbf{r}, v) \tag{2.20}$$

where

$$f_0 = \frac{1}{4\pi} \int_{4\pi} f(\mathbf{r}, v) d\mathbf{\Omega}, \tag{2.21}$$

$$\mathbf{f}_1 = \frac{3}{4\pi} \int_{4\pi} f(\mathbf{r}, v) \mathbf{\Omega} d\mathbf{\Omega}. \tag{2.22}$$

Taking the zeroth and first order moments of Eq. (2.19) yields

$$v\nabla \cdot \mathbf{f}_1 - \frac{e\mathbf{E}}{m_e v^2} \cdot \frac{\partial(v^2 \mathbf{f}_1)}{\partial v} = C_0 \tag{2.23}$$

$$\frac{v}{3}\nabla f_0 - \frac{e\mathbf{E}}{3m_e}\frac{\partial f_0}{\partial v} = \mathbf{C}^1 \tag{2.24}$$

where it is assumed that C^0 only depends on the isotropic Rosenbluth potentials ($C^0 = C^0(f_0)$) and that $\mathbf{C^1}$ is well approximated by the Lorentz model

$$\mathbf{C}^1 = -\nu'_{ei}\mathbf{f}_1. \tag{2.25}$$

In order to complete the system a zero current condition is applied in order to calculate the electric field term

$$\mathbf{J} = e\int f(\mathbf{v})\mathbf{v}d\mathbf{v} = e\int \mathbf{f}_1 v^3 dv = 0. \tag{2.26}$$

This condition results from Maxwell's equations and the assumptions that the electron transport equation is steady state and magnetic field free. Solving Eq. (2.24) for $\mathbf{f}_1$ and noting that ν'_{ei} is proportional to v^{-3} gives the zero current condition of

$$\int \left(\frac{v}{3}\nabla f_0 - \frac{e\mathbf{E}}{3m_e}\frac{\partial f_0}{\partial v}\right) v^6 dv = 0 \tag{2.27}$$

The system of equations is:

$$F_0(f_0, f_1, \mathbf{E}) = 0 = C^0(f_0) - v\nabla \cdot \mathbf{f}_1 + \frac{e\mathbf{E}}{m_e v^2}\frac{\partial(v^2\mathbf{f}_1)}{\partial v}, \tag{2.28}$$

$$\mathbf{F}_1(f_0, f_1, \mathbf{E}) = 0 = -\nu'_{ei}\mathbf{f}_1 - \frac{v}{3}\nabla f_0 + \frac{e\mathbf{E}}{3m_e}\frac{\partial f_0}{\partial v}, \tag{2.29}$$

$$\mathbf{F}_E(f_0, f_1, \mathbf{E}) = 0 = \int \left(\frac{v}{3}\nabla f_0 - \frac{e\mathbf{E}}{3m_e}\frac{\partial f_0}{\partial v}\right) v^6 dv. \tag{2.30}$$

Writing $F = (F_0, \mathbf{F_1}, \mathbf{F_E})$ and $X = (f_0, \mathbf{f_1}, \mathbf{E})$ the system can be solved iteratively via Newton's method

$$\left[\frac{\partial F}{\partial X}\right]_n \Delta X_n = -F(X_n). \tag{2.31}$$

The Jacobian $\mathcal{J} = [\partial F/\partial X]$ of the system is

$$\begin{bmatrix} \dfrac{\partial C^0(\,)}{\partial f_0} & -\mathbf{v}\nabla\cdot(\,) + \dfrac{e\mathbf{E}}{m_e v^2}\dfrac{\partial v^2(\,)}{\partial v} & \dfrac{e(\,)}{m_e v^2}\dfrac{\partial(v^2\mathbf{f}_1)}{\partial v} \\ -\dfrac{v}{3}\nabla(\,) - \dfrac{e\mathbf{E}}{m_e}\dfrac{\partial}{\partial v}(\,) & -\dfrac{\nu'_{ei}}{3} & -\dfrac{e(\,)}{m_e}\dfrac{\partial f_0}{\partial v} \\ \int\left(v\nabla(\,) - \dfrac{e\mathbf{E}}{m_e}\dfrac{\partial}{\partial v}(\,)\right)v^6 dv & 0 & -\dfrac{e(\,)}{m_e}\int\dfrac{\partial f_0}{\partial v}v^6 dv \end{bmatrix}. \tag{2.32}$$

This Jacobian can be approximated by noting that terms involving the electric field vary as $k_b T_e/m_e v^2$ when compared to collisional and spatial derivative terms. Since f is expected to differ from f_{mb} only at high velocities the electric field terms are dropped. Furthermore it is assumed that $\partial C^0/\partial f_0$ can be well approximated by the electron-electron collision frequency $-\nu_{ee}(v)$. The simplified algorithm is now,

$$\begin{bmatrix} -\nu_{ee}(v) & -v\nabla\cdot \\ -v\nabla/3 & -\nu'_{ei}(v) \end{bmatrix} \begin{bmatrix} \Delta f_0^n \\ \Delta\mathbf{f}_1^n \end{bmatrix} = \begin{bmatrix} -F_0(f_0, f_1, \mathbf{E}) \\ -\mathbf{F}_1(f_0, f_1, \mathbf{E}) \end{bmatrix}. \tag{2.33}$$

SNB recommend taking a single iteration of Eq. (2.33). The initial condition is chosen by setting $f_0^0 = f_0^{mb}$ and then solving Eqs. (2.29) and (2.30) for $\mathbf{f}_1^0 = \mathbf{f}_1^{mb}$ and $\mathbf{E}^0 = \mathbf{E}^{mb}$ respectively. Plugging into Eq. (2.33), $\mathbf{F}_1$ is zero by construction and the equations become

$$\nu_{ee}\Delta f_0 + v\nabla\cdot(\Delta\mathbf{f}_1) = -v\nabla\cdot\mathbf{f}_1^{mb} + \frac{e\mathbf{E}^{mb}}{m_e v^2}\frac{\partial(v^2\mathbf{f}_1^{mb})}{\partial v}, \tag{2.34}$$

$$\nu'_{ei}\Delta\mathbf{f}_1 = -\frac{v}{3}\nabla(\Delta f_0). \tag{2.35}$$

Collecting the coefficients in terms of MFPs

$$\lambda_{ei}(v) = \frac{v}{v'_{ei}} = \left(\frac{v}{v_{th}}\right)^4 \frac{(k_b T_e)^2}{4\pi n_e e^4 \log\Lambda}, \tag{2.36a}$$

$$\lambda_{ee}(v) = Z\lambda_{ei}(v), \tag{2.36b}$$

$$\lambda(v) = \sqrt{\lambda_{ee}(v)\lambda_{ei}(v)} \tag{2.36c}$$

and combining equations (2.34) and (2.35) produces the diffusion equation

$$\left(\frac{1}{\lambda(v)} - \nabla\frac{\lambda(v)}{3}\nabla\right)\left(\frac{\sqrt{Z}m_e}{2}v^5\Delta f_0\right) = -\frac{m_e}{2}\nabla\cdot(v^5\mathbf{f}_1^{mb}) + \frac{e\mathbf{E}^{mb}}{2}\cdot v^2\frac{\partial(v^2\mathbf{f}_1^{mb})}{\partial v}. \tag{2.37}$$

Noting that the velocity integral of the right hand side of Eq. (2.37) is $-\nabla\mathbf{Q}_{SH} + \mathbf{J}\cdot\mathbf{E}$, the expression is reformulated as

$$\left(\frac{1}{\lambda(v)} - \nabla\frac{\lambda(v)}{3}\nabla\right)\left(\frac{\sqrt{Z}m_e}{2}v^5\Delta f_0\right) = -\nabla\cdot(g(v)\mathbf{Q}_{SH}). \tag{2.38}$$

The flux expression is

$$\begin{aligned}\mathbf{Q} &= \frac{m_e}{2}\int f(\mathbf{v})\mathbf{v}^3 d\mathbf{v}\\ &= \frac{m_e}{2}\int \mathbf{f}_1 v^5 dv\\ &= \frac{m_e}{2}\int(\mathbf{f}_1^{mb} + \Delta\mathbf{f}_1)v^5 dv\\ &= \mathbf{Q}_{SH} - \frac{m_e}{2}\int\frac{\lambda}{3}\sqrt{Z}\nabla(\Delta f_0)v^5 dv.\end{aligned} \tag{2.39}$$

By defining

$$H(v) = \frac{1}{2}m_e\sqrt{Z}v^5\Delta f_0, \tag{2.40}$$

$$g(v) = (v/v_{th})^9 e^{-(v/v_{th})^2} \Big/ \int (v/v_{th})^9 e^{-(v/v_{th})^2} dv. \tag{2.41}$$

Eqs. (2.17) and (2.18) are recovered. The SH heat flux contribution can be interpreted as the correction due to the non-Maxwellian part of the zeroth angular moment of the electron distribution function.

Nicolai, Feugeas, and Schurtz have expanded the model by SNB to include self-consistent magnetic effects [14]. The primary result from this study is that magnetic effects reduce the heat flux due to electron transfer perpendicular to the temperature and density gradients.

2.1.3 Implicit SNB

Cao et. al. have worked to improve upon the original method developed in Schurtz et. al, developing an improved implicit SNB (iSNB) algorithm for use in LLE's DRACO radiation hydrodynamics production code [15][16][17]. In order to advance the system in time, the SNB method is coupled to the electron temperature equation

$$\rho C_v \frac{\partial T_e}{\partial t} = -\nabla \cdot \mathbf{Q} + S_{ext} \tag{2.42}$$

where ρ is the density, C_v is the specific heat, $\mathbf{Q}$ is the heat flux, and S_{ext} represents all the other terms in the electron heat equation, such as the work and electron-ion coupling terms. Starting at time step n the iSNB algorithm iteratively solves for the updated temperature at the next time step $n+1$. In contrast to SNB's original algorithm which solves explicitly for $\mathbf{Q}_{nl}$, the iSNB algorithm solves for the easier to compute $\nabla \cdot \mathbf{Q}_{nl}$:

$$\nabla \cdot \mathbf{Q}_{nl} = -\sum_g \frac{H_g}{\lambda_g}. \tag{2.43}$$

Since $\nabla \cdot \mathbf{Q}_{nl}$ is used directly in the temperature equation and does not require the computation of any derivatives of H_g, numerical stability is improved. The iterative algorithm is as follows:

1. Solve the temperature equation for $T_e^{(k)}$

$$\rho C_v \frac{T_e^k - T_e^n}{\Delta t} = -\nabla \cdot \mathbf{Q}_{sh}^k + S_{ext}^n + S_{nl,correction}^{k-1} \tag{2.44}$$

where k is the iterative index, K_{SH}^n is the coefficient in the SH flux, $S_{nl,correction}^{k-1}$ is the SNB correction to the SH flux, and $S_{nl,correction}^0 = 0$.

2. Recompute $\nabla \cdot \mathbf{Q}_{sh}^k$ using T_e^k.

3. If $k > 1$, check for convergence with criterion

$$|\nabla \cdot \mathbf{Q}_{sh}^k - \nabla \cdot \mathbf{Q}_{sh}^{k-1}| \leq \alpha \rho C_{v,e} \frac{T_e^k}{\Delta t} \tag{2.45}$$

where α is a user defined parameter set to $\alpha = 0.01$. Cao recommends only checking convergence in cells with a density greater than 1×10^{-4} g/cm^3. If converged, set $T_e^{n+1} = T_e^{(k)}$, exit the loop, and advance to the next time step.

4. If not converged, solve the SNB diffusion equation for H_g

$$\left(\frac{1}{\lambda_g(\mathbf{r})} - \nabla \frac{\lambda_g(\mathbf{r})}{3} \nabla \right) H_g(\mathbf{r}) = -\nabla \cdot \left(\frac{K_{SH}^n \nabla T_e^k}{24} \int_{\beta_{g-1}}^{\beta_g} \beta^4 e^{-\beta} d\beta \right) = -\nabla \cdot \mathbf{U}_g^k \tag{2.46}$$

where g is the group index and $\beta_g = E_g/kT$.

5. Compute

$$-\nabla \cdot \mathbf{Q}_{nl}^k = \sum_{g=1}^{G} \frac{H_g}{\lambda_g}. \tag{2.47}$$

6. Compute

$$S_{nl,correction}^{(k)} = -\nabla \cdot \mathbf{Q}_{nl}^k + \nabla \cdot \mathbf{Q}_{sh}^k. \tag{2.48}$$

7. Repeat from Step 1 for the next iteration of k.

It is important to use consistent finite differencing when iterating in order to maintain stability in the solution. In particular, consistency is needed when computing $\nabla \cdot \mathbf{U}_g$ and $\nabla \cdot \mathbf{Q}_{sh}$ as both have the form $\nabla \cdot K \nabla T_e$.

Validation of the iSNB method was performed using data from an ICF experiment performed at LLE's OMEGA facility (shot 60303) [18]. The 60303 shot consisted of three picket laser pulses followed by a main laser drive (Fig. 2.1). Shock velocity data was measured using a VISAR (Velocity Interferometer System for Any Reflector) probe and is plotted in Fig. 2.1. The rises in the shock velocity near 2 ns, 2.3 ns, and 3 ns are caused by the laser induced shocks converging. Fig. 2.2 shows the target configuration; the 60303 fuel capsule consists of an outer polystyrene shell of density 1.08 g/cm^3, a DD liquid layer of density 0.198 g/cm^3 and an inner DD gas layer of density 4.5×10^{-4} g/cm^3.

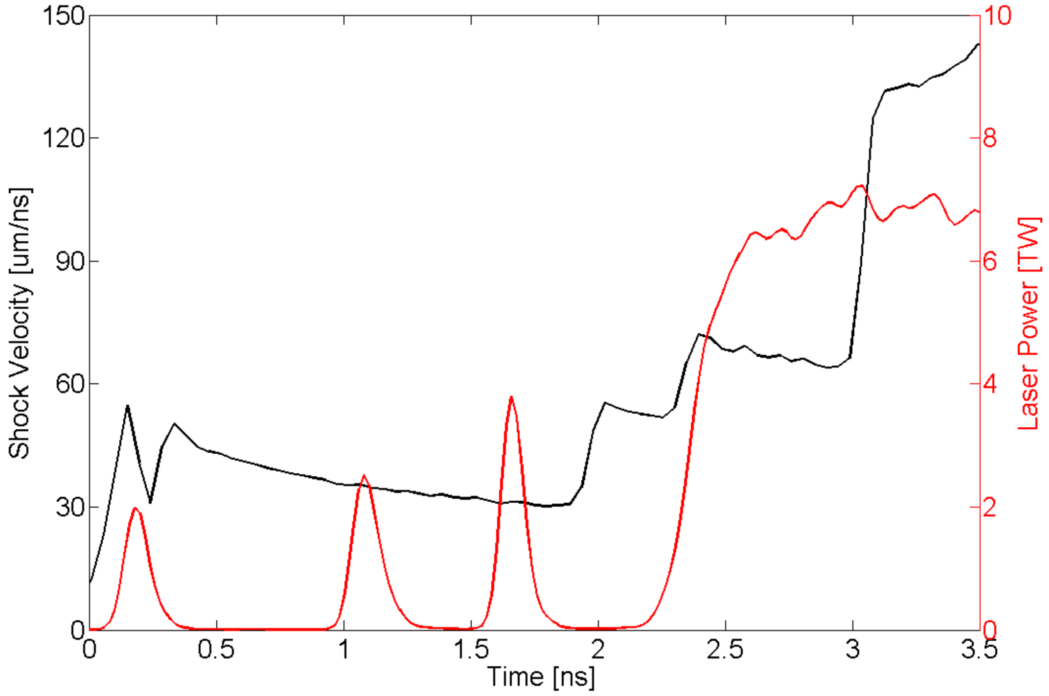

Figure 2.1: *Shock velocity vs. time in shock 60303 as measured by VISAR (black). Laser power profile given in comparison to visualize relationship between laser pulses and shock convergence (red) [Figure obtained from [17]][18].*

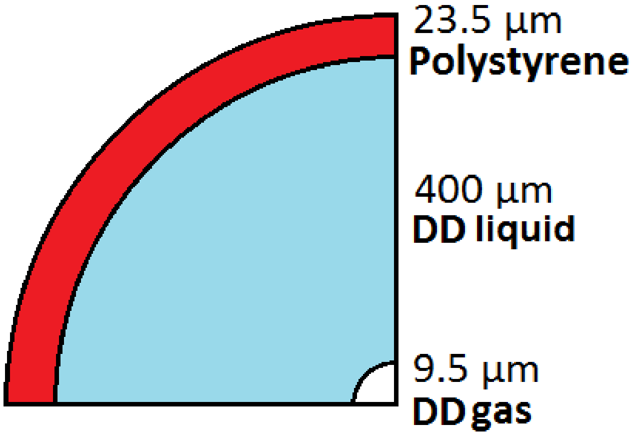

Figure 2.2: *Three layered spherically symmetric fuel capsule for shot 60303 [Figure obtained from [17]].*

The experiment was modeled using the LILAC and DRACO codes using SESAME equation of state values and ASTRO ionization and opacity data. The 1D LILAC code uses a transport method developed by V. Goncharov, described in Section 2.1.4, to calculate the electron heat flux. LILAC, using Goncharov's non-local model, accurately predicts the experimental shock velocities (Fig. 2.3a) and was used as a comparison for DRACO. In initial calculations DRACO iSNB model did not agree well with the LILAC results, but fared better than the flux limited model in predicting the shock timing. The flux-limited calculation missed all three shock convergences while the iSNB model was more successful and predicted the first and third shock timings (Fig. 2.3b). In Fig. 2.4, the temperature profiles computed by DRACO were compared to the LILAC simulation. The flux-limiter model, due to being a local model, underpredicted preheating in the temperature profiles for all times in comparison to LILAC. The iSNB model, on the other hand, overpredicted preheating. The overprediction of preheating can be attributed to erroneous application of the MFP formula used by iSNB. The formula used is only applicable for higher temperatures and becomes inaccurate, growing without bound, as T_e approached zero. Since at early times the fuel capsule is cold, the iSNB method has too high electron MFPs which allow for electrons to stream out of the gradient region, creating excessive preheat. The iSNB MFP formula can be compared to room temperature NIST data, which shows a MFP overprediction by two orders of magnitude at room temperature (Fig. 2.5a). Cao suggests modifying the MFP formula by introducing a multiplicative S-Weighting function that acts to reduce MFPs at low temperatures (Fig. 2.5b). After application of the S-Weight function the temperature profiles calculated by DRACO iSNB agree much better with the LILAC results (Fig. 2.6a). Furthermore, the shock velocities (Fig. 2.6b) are unchanged by the introduction of the modified MFPs.

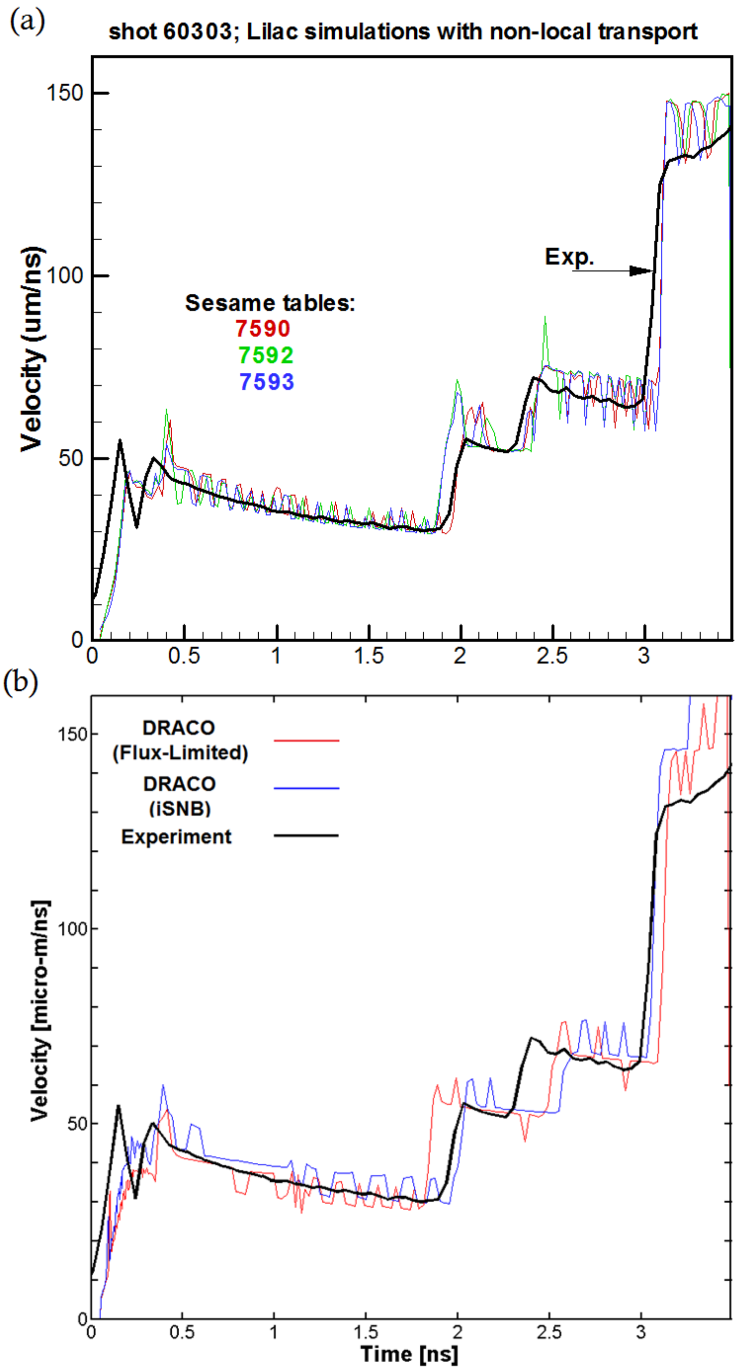

Figure 2.3: *(a) Shock Velocity results using a 1D LILAC simulation of shot 60303. The LILAC solutions (colored) accurately reproduce the shock timings of the experimental data(black) (b) Shock Velocity results using DRACO flux-limited and iSNB simulations of shot 60303. The DRACO models fared worse than the LILAC model in predicting the shock velocity, with the flux-limited calculation missing all three shock convergences and the iSNB model missing the second convergence [Figures obtained from [17]].*

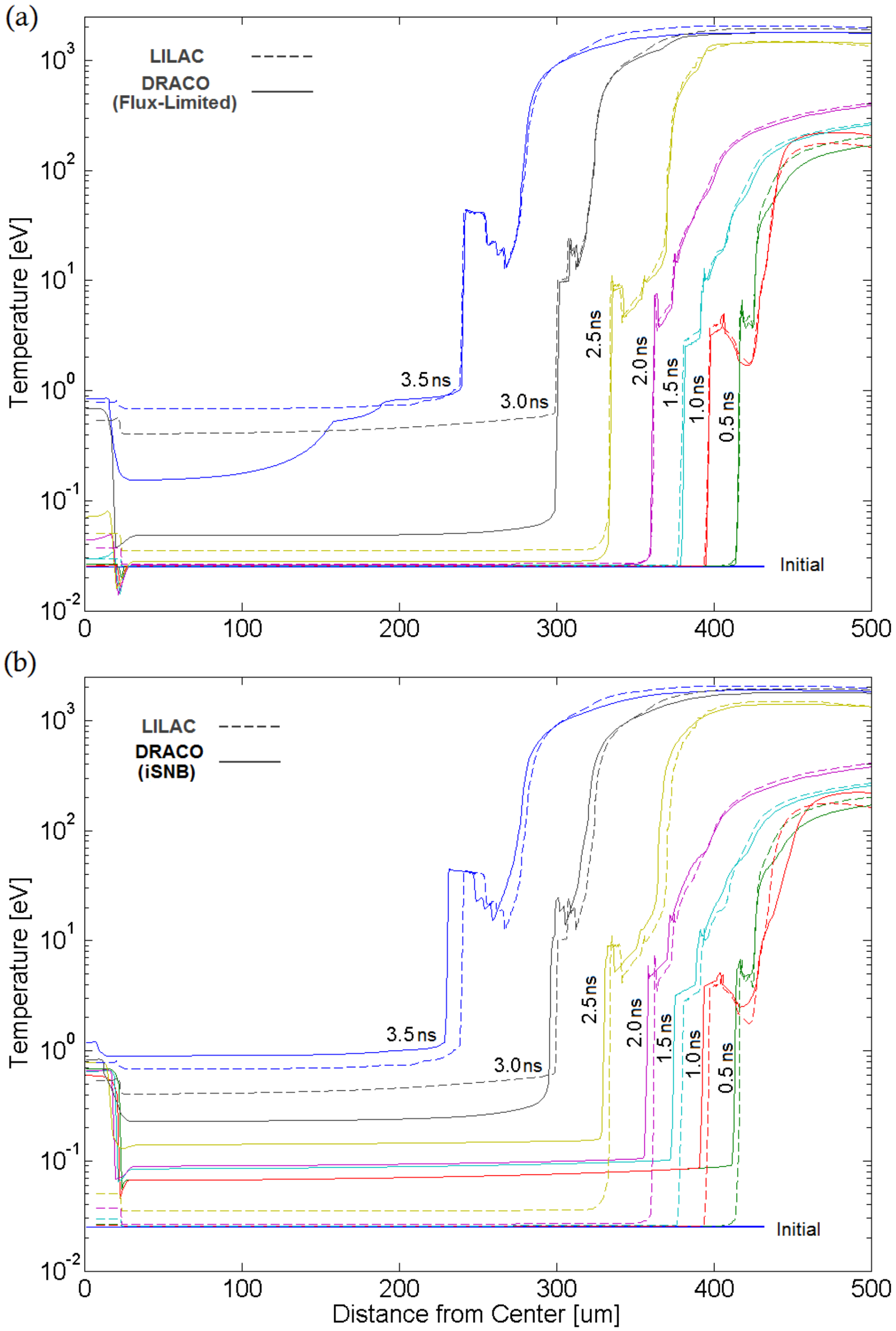

FIGURE 2.4: *(a) DRACO flux-limited temperature profiles (solid) in comparison with LILAC (dashed). (b) DRACO iSNB temperature profiles (solid) in comparison with LILAC (dashed). The iSNB method shows over prediction of the preheating in early times of the simulation in comparison to LILAC [Figures obtained from [17]].*

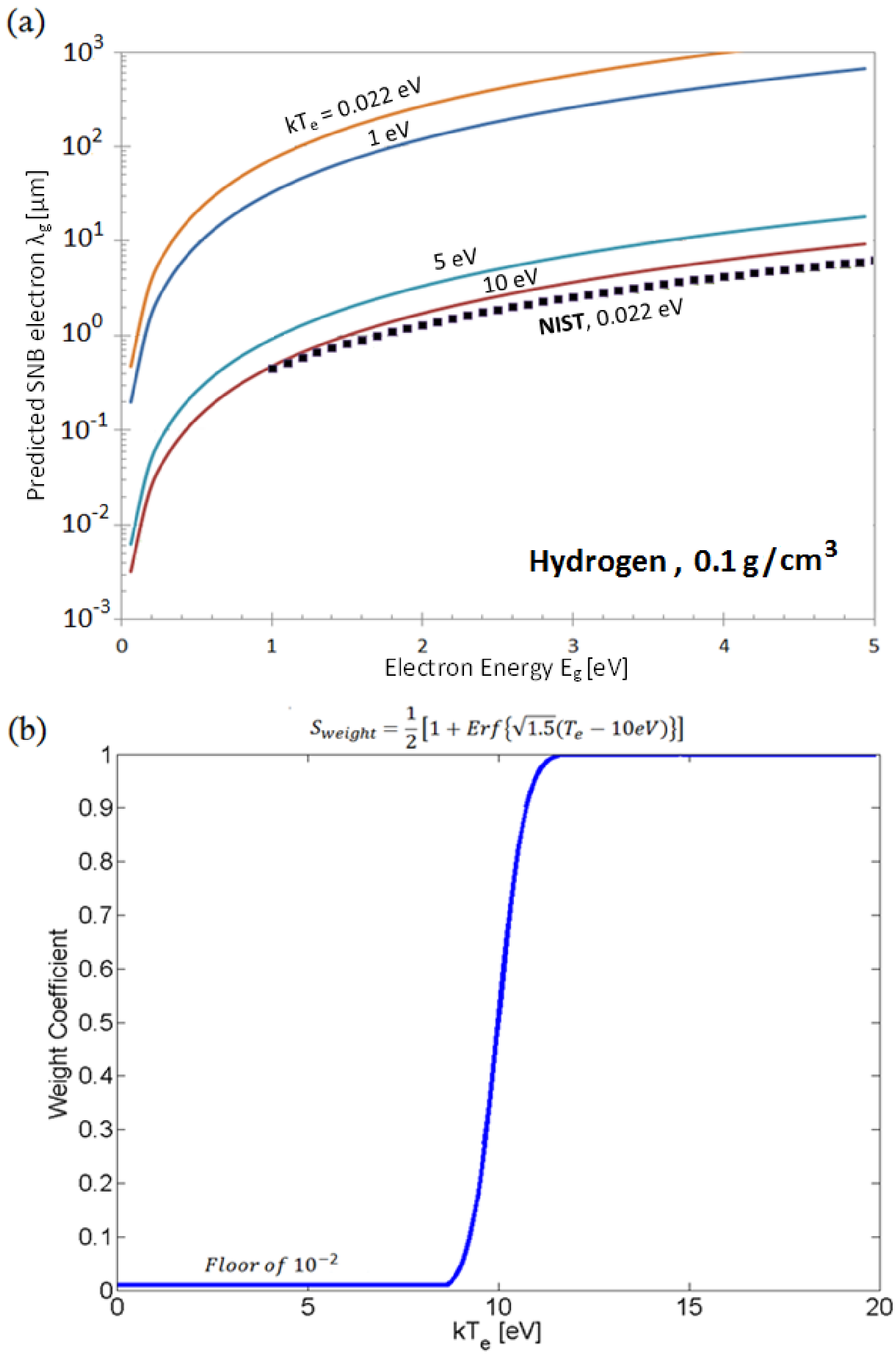

Figure 2.5: *(a) Electron MFP using Eq. (2.36) at varying temperatures (solids) and NIST MFPs at room temperature (dashed) showing disagreement at room temperature background. (b) Plot of S-Weight multiplicative factor used to adjust iSNB MFPs at low temperatures [Figures obtained from [17]].*

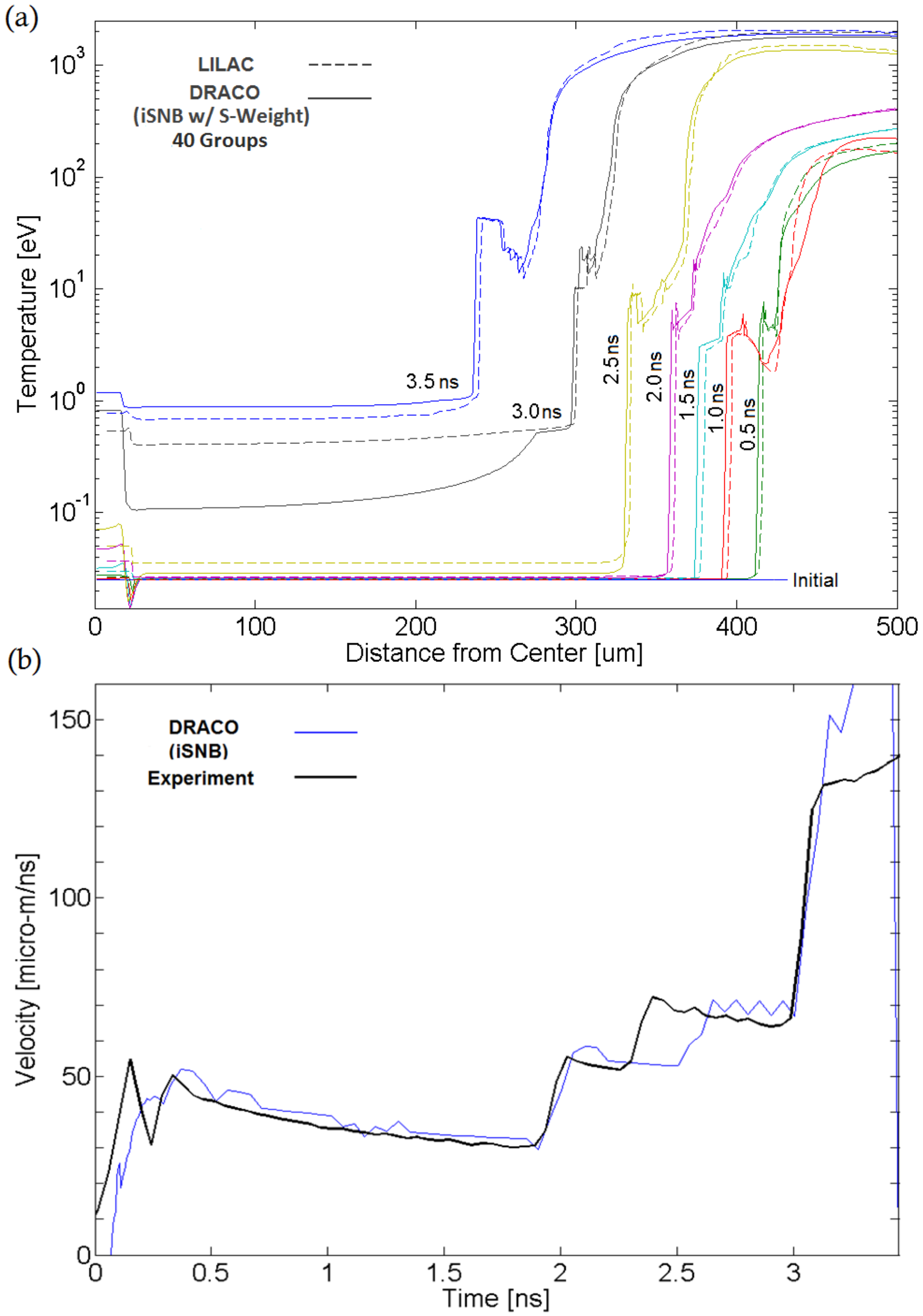

FIGURE 2.6: *(a) DRACO iSNB temperature profiles (solid) in comparison with LILAC (dashed) showing better agreement than with unmodified MFPs (b) The shock velocity profile calculated by DRACO iSNB remains unchanged after MFP modification [Figures obtained from [17]].*

In addition to the S-weight correction, Cao has utilized a range based formula to calculate the iSNB MFPs. The electron slowing down formula is presented in a 2009 paper by Atzeni, Schiavi, and Davies [19]. In a fully ionized plasma of density ρ, atomic number Z, and mass number A, an electron with kinetic energy E experiences a stopping power of

$$\frac{dE}{\rho ds} = -\frac{D}{\beta^2} \tag{2.49}$$

where

$$D = \frac{4\pi e^4}{m_p m_e c^2}\frac{Z}{A}\left[\ln\left(\frac{m_e c^2}{\hbar\omega_{pe}}\right) + \frac{9}{16} - \frac{1}{2}\ln 2 + f(\gamma)\right] \tag{2.50}$$

and

$$f(\gamma) = \ln\left(\beta\sqrt{\gamma - 1}\right) - \frac{(1/8) + \ln 2}{\gamma} + \frac{(1/16) + (1/2)\ln 2}{\gamma^2} \tag{2.51}$$

where m_p is the proton mass, $\hbar$ is the reduced Planck constant, $\omega_{pe} = \sqrt{4\pi n_e e^2/m_e}$ is the electron-plasma frequency, n_e is the electron density, β is ratio of velocity to the speed of light, and γ is the Lorentz factor.

This stopping power equation is used to compute ranges for use as the iSNB λ's. Letting i refer to the cell center and $i - 1/2$ refer to the boundary between cell i and $i - 1$, the algorithm (in 1D) is as follows:

1. Set $k = 0$, $l = i$, $E^0 = E_g$, and $\lambda_{i,g} = 0$ where k is the iterative index, l is the current positional index. E_g is the group energy, and $\lambda_{i,g}$ is the range for cell i energy group g

2. Compute dE/ds for conditions in cell l and energy E^k

3. Compute

   $$E^{k+1/2} = E^k + \Delta s\frac{dE}{ds} \tag{2.52}$$

   where $\Delta s = r_l - r_{l-1/2}$.

If $E^{k+1/2} < 0$, then

$$\lambda_{i,g} = \lambda_{i,g} - \frac{E^k}{dE/ds} \tag{2.53}$$

Stop the iteration

Else

$$\lambda_{i,g} = \lambda_{i,g} + \Delta s. \tag{2.54}$$

4. Compute dE/ds for conditions in cell $l-1$ and energy $E^{k+1/2}$.

5. Compute

$$E^{k+1} = E^{k+1/2} + \Delta s \frac{dE}{ds} \tag{2.55}$$

where $\Delta s = r_{l-1/2} - r_{l-1}$.

If $E^{k+1} < 0$, then

$$\lambda_{i,g} = \lambda_{i,g} - \frac{E^{k+1/2}}{dE/ds} \tag{2.56}$$

Stop the iteration

Else

$$\lambda_{i,g} = \lambda_{i,g} + \Delta s. \tag{2.57}$$

6. Set $l = l - 1$ and continue at Step 2. (Note: in the event l=1, the origin has been reached and marching should continue outward at half-cell intervals until energy is depleted).

2.1.4 Valeri Goncharov's Non-Local Transport Method

Goncharov et. al. develop a 1-D non-local model (hereafter Goncharov's model) to better model shock timing [20]. This model is used in the LILAC code, which was used in the validation of the DRACO iSNB method in the previous section. The derivation starts with the steady state 1-D planar geometry kinetic equation

$$v_x \frac{\partial f}{\partial x} + \frac{eE_x}{m_e}\frac{\partial f}{\partial v_x} = J(f) \tag{2.58}$$

where $J(f)$ is the collision operator, E_x is the electric field, and v_x is the x-direction velocity. The $J(f)$ term is then simplified to only consider electron-ion collisions and is written

$$J(f) = -(f - f_0)\nu_{ei}(v, x) \tag{2.59}$$

where f_0 is the isotropic part of the electron distribution function and ν_{ei} is the electron-ion collision frequency. Assuming the $\frac{\partial f}{\partial v_x}$ term in Eq. (2.58) is well approximated by $\frac{\partial f_0}{\partial v_x}$ and then integrating, an expression for f is calculated

$$f = \int^x \left[f_0(x', v) - \frac{eE_x}{m_e}\frac{\partial f_0}{\partial v_x} \right] W_e(x', x, \mu) \frac{dx'}{\lambda_{ei}(v, x')\mu} \tag{2.60}$$

where $\lambda_{ei} = v/\nu_{ei}$ is the electron-ion MFP, μ is the direction cosine in the x-direction, and the kernel W_e is

$$W_e(x', x, \mu) = e^{-\xi(x',x)/\mu}, \quad \xi(x', x) = \int_{x'}^{x} \frac{dx''}{\lambda_{ei}}. \tag{2.61}$$

The kernel W_e only accounts for electron diffusion due to interactions with ions. Electron-electron collisions and plasma wave excitation will limit electron deposition range to a finite value λ_E. A new kernel that vanishes at $\xi = 1$ can be derived by considering the slowing down formula

$$\frac{dK}{ds} = -\frac{K}{2\lambda_E(K)} \tag{2.62}$$

where K is the electron energy and ds is the differential electron path. Noting $\lambda_E \sim K^2$ and integrating the slowing down formula gives

$$W(x', x, \mu) = C_N \frac{K(x)}{K(x')} = C_N \sqrt{1 - \frac{\xi(x', x)}{\mu}}, \quad \xi(x', x) = \left| \int_{x'}^{x} \frac{dx''}{\lambda_E} \right| \tag{2.63}$$

where $C_N = 3/2$ is a normalization constant. Replacing W_0 with W and λ_{ei} with λ_E in Eq. (2.60) the current $j_x = e \int d^3 v v_x f$ and the heat flux $q_x = m_e \int d^3 v v^2 v_x f/2$ are

$$j_x = 2\pi e \int_0^\infty dv v^3 P(x, v) \tag{2.64}$$

and

$$q_x = \pi m_e \int_0^\infty dv v^5 P(x, v) \tag{2.65}$$

where

$$P(x, v) = \frac{3}{2} \int_{-\infty}^{x} dx' F_0^-(v, x, x') H(1 - \xi) - \frac{3}{2} \int_{x}^{\infty} dx' F_0^+(v, x, x') H(1 - \xi) \tag{2.66}$$

and

$$F_0^\pm = \frac{f_0}{\lambda} I_1(x, x') \pm \frac{eE_x(x')}{T} \frac{\partial f_0}{\partial \hat{\epsilon}} I_2(x, x'), \tag{2.67}$$

$$I_1 = \sqrt{1 - \xi} - \xi \ln \frac{1 + \sqrt{1 - \xi}}{\sqrt{\xi}}, \tag{2.68}$$

$$I_2 = \frac{(1 - \xi)^{3/2}}{2} + \frac{\xi}{4} I_1 \tag{2.69}$$

where $H(x)$ is the Heaviside function and $\hat{\epsilon} = mv^2/2T$. The isotropic distribution function f_0 is assumed to be a Maxwellian. The electric field E_x is defined by applying a zero current condition $j_x = 0$ and then solving the resultant integral equation iteratively for electric field via $E_x^{(n)}(x') = E_x^{(n)}(x) + [E_x^{(n-1)}(x') - E_x^{(n-1)}(x)]$.

Goncharov takes into account collisional and collective effects to calculate the penetration depth λ_E. Considering the electron-electron and collective wave effects gives an electron deposition path of

$$\lambda_K = \frac{K^2}{4\pi e^4 (n_e^T \Lambda_e + n_e^f \Lambda_c)} \tag{2.70}$$

where n_e^f is the free electron density, n_e^T is the total electron density, Λ_e is the electron-electron Coulomb logarithm, and

$$\Lambda_c = \log\left(\frac{1.123v}{\omega_p b_{max}}\right) \tag{2.71}$$

where ω_p is the plasma frequency and b_{max} is the maximum impact parameter. Taking into account electron-ion collisions the 90° scattering path length is

$$\lambda_{90} = \frac{K^2}{2\pi e^4 n_e^T (\Lambda_e + Z\Lambda_i/2)} \tag{2.72}$$

where Λ_i is the electron-ion Coulomb logarithm and Z is the mean ion charge The electron penetration depth is then given via

$$\lambda_E = \sqrt{\lambda_{90}\lambda_K}. \tag{2.73}$$

In Fig. 2.7 Goncharov's model provides good agreement with the experimental VISAR measurements and accurately predicts the shock break out time and shock speed. Goncharov compares his model against flux-limited SH and iSNB non-local models. Fig. 2.8 compares calculated temperature and density profiles for three models at shock breakout for a $40\mu m$ thick CH foil driven by a square laser pulse with peak intensity of 4×10^{14} W/cm^2. The SH (dashed lines) and Goncharov (solid lines) models show similar profiles both showing similarly low preheats. The iSNB model gives a higher preheat and broader density distribution indicating an over-driven plasma. Unfortunately, Goncharov's model does not scale well to

2D DRACO due to too high run times so the faster SNB method is used in multidimensional calculations and hence the desire for improvement upon the multigroup diffusion solution discussed in this thesis.

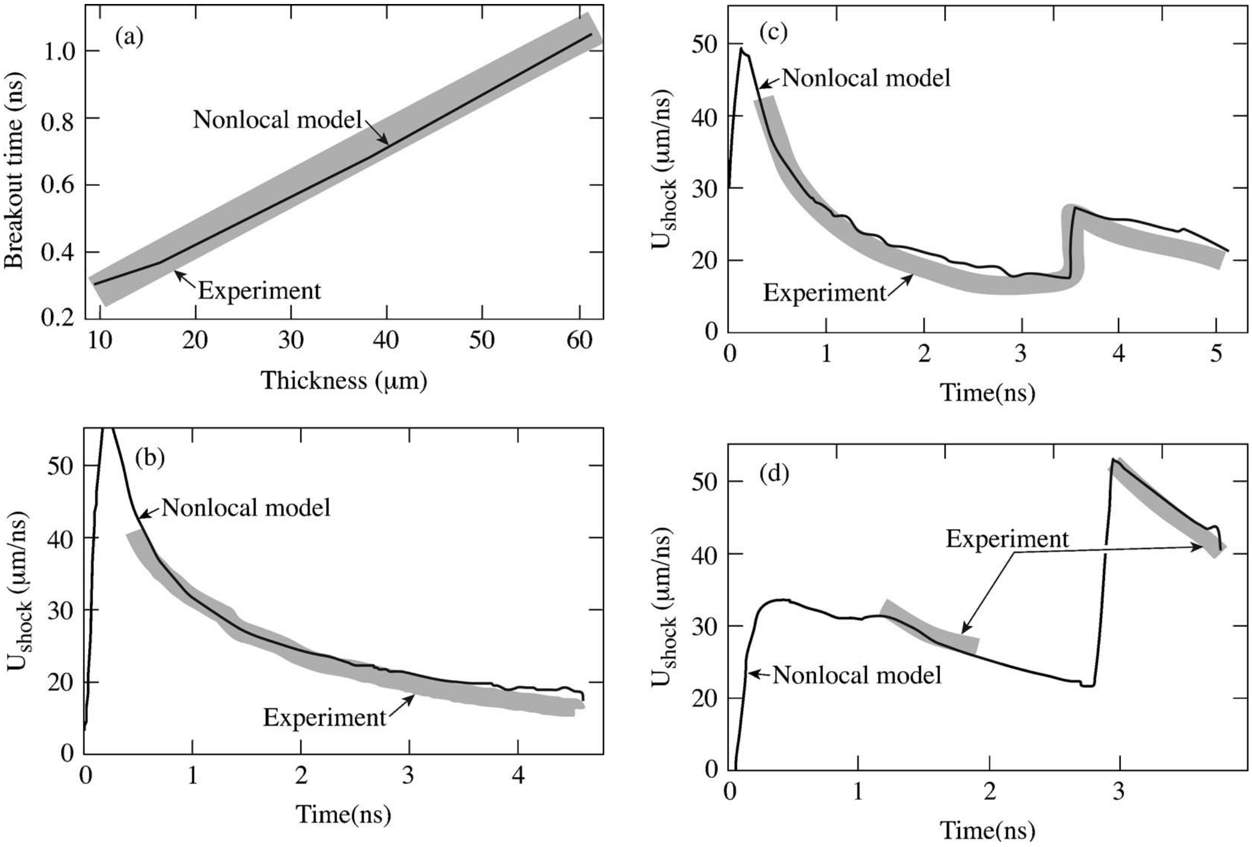

Figure 2.7: *Goncharov's non-local model (solid lines) shows good agreement with CH foil experiment results obtained on the Omega laser system (thick gray lines). (a) Comparison of shock breakout time vs. foil thickness. (b)-(d) Shock velocity over time comparison between simulation and experimental data. (b) Single 100ps picket with peak intensity* 4.9×10^{14} *W/cm*^{2}*. (c) Double 100ps pickets with peak intensities* 2.2×10^{14} *W/cm*^{2} *and* 4.5×10^{14} *W/cm*^{2}*. (d) Double 600ps pulses with peak intensities of* 4.4×10^{13} *W/cm*^{2} *and* 2×10^{14} *W/cm*^{2} *[Figures obtained from [20]].*

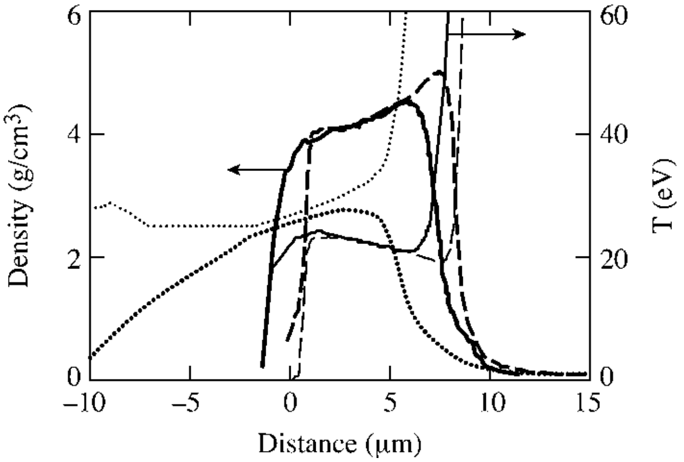

FIGURE 2.8: *Density (thick lines) and temperature (thin lines) profiles calculated at shock break out time with the flux limited SH model (dashed), the non-local Goncharov's model (solid), and the SNB model (dotted) [Figure obtained from [20]].*

2.1.5 Non-Local Model of Manheimer and Colombant

For the local approximation, Manheimer and Colombant begin their derivation with the steady state Boltzmann equation with a Krook collision operator

$$v_x \frac{\partial f}{\partial x} - \frac{e\mathcal{E}_x}{m_e}\frac{\partial f}{\partial v_x} = -(\nu_{ee} + \nu_{ei})(f(v) - f_{mb}(v)) \tag{2.74}$$

where ν_{ei} and ν_{ee} are the electron-ion and electron-electron collision frequencies respectively [21][22]. By writing the distribution function as the sum of a Maxwellian and a correction $f = f_{mb} + f_{1L}$ the local distribution is given by

$$f_{mb} = \frac{n_e}{(2\pi T_e/m_e)^{3/2}} \exp\left(-\frac{m_e v^2}{2T_e}\right) \tag{2.75}$$

and

$$f_{1L} = \frac{1}{\nu_{ee} + \nu_{ei}} \left[\varepsilon(x) + \left(\frac{m_e v^2}{2T_e} - 3/2 \right) \frac{1}{T_e} \frac{dT_e}{dx} \right] v_x f_{mb} \tag{2.76}$$

where

$$\varepsilon(x) = \frac{1}{n} \frac{dn}{dx} + \frac{e\mathcal{E}}{T_e}. \tag{2.77}$$

In order to solve for the electric field term, the zero current condition is applied. The electric field term is found to be

$$\varepsilon(x) = \left[\frac{3}{2} - \frac{Z_4(Z)}{Z_2(Z)} \right] T_e'/T_e \tag{2.78}$$

where

$$Z_n(Z) = \frac{1}{5.4} \int_0^\infty \frac{u^{(n+4)/2} \exp(-u)}{B(u, Z)} du \tag{2.79}$$

and

$$B(y, Z) = \frac{y^{3/2}}{1.3 + y^{3/2}} + \frac{Z}{2}. \tag{2.80}$$

Note that $B(y, Z)$ and $Z_n(Z)$ arise from the functional forms of the collision frequencies. Taking the appropriate moment of the distribution function the local flux is

$$q_{sp} = -K_{sp} T^{5/2} \frac{\partial T}{\partial x} = \int_0^\infty q(x, E) dE \tag{2.81}$$

where q is in erg/cm^2-s, T and E are in eV, and lengths are in cm.

$$q(x, E) = -\frac{K_{sp}}{\beta(\infty, Z)} \frac{E^4 \left[\frac{E}{T} - \frac{Z_4}{Z_2} \right] \frac{\partial T}{\partial x}}{T^{5/2} B(E/T, Z)} \exp(-E/T) \tag{2.82}$$

where E is the particle energy, $q(x, E)$ is an energy dependent flux and

$$\beta(y, Z) = \int_0^y \frac{\left(u - \frac{Z_4}{Z_2} \right) u^4 \exp(-u)}{B(u, Z)} du \tag{2.83}$$

The non-local Krook heat flux is generated by convoluting a delocalization kernel with Eq. (2.82) and adding a non-local correction to the electric field $\delta\varepsilon$. Taking these things into account the non-local flux is

$$q(x) = -\frac{1}{2}\int_{-\infty}^{\infty}\int_{0}^{\infty} \frac{K_{sp}}{\beta(\infty, Z)} \frac{E^4\left(\left[\frac{E}{T} - \frac{Z_4}{Z_2}\right]\frac{\partial f}{\partial x'} + T\delta\varepsilon\right)}{T^{5/2}B(E/T, Z)} \times \left\{k(x', E)\exp(-\left|H(x, x', E)\right|\right\}\exp\left(-E/T\right) dE\, dx' \tag{2.84}$$

where

$$H = \int_{x'}^{x} dx'' k(x'', E) \tag{2.85}$$

and $k(x, E)$ is the inverse MFP, which is well approximated in the high energy limit by

$$k(x, E) = \frac{2.26 \times 10^{-13} n \log\Lambda\sqrt{1 + Z/2}}{E^2}. \tag{2.86}$$

Due to numerical constrains arising from a finite grid discretization, Colombant and Manheimer recommend preforming the convolution integral only above some cutoff energy E_{cr} below which the local approximation is sufficient. To choose an appropriate value of E_{cr}, a set of three conditions is imposed

$$k(x, E_{cr})\Delta x = 0.2, \quad L_T > 5\Delta x \tag{2.87a}$$

$$k(x, E_{cr})L = 1, \quad L_T < 5\Delta x \tag{2.87b}$$

$$E_{cr}/T > 4.2 \tag{2.87c}$$

where Δx is the grid spacing, L_T is the temperature gradient length, and L is the problem scale length. By applying a perturbation expansion to the non-local expression and reapplying the zero current condition, the correction to the electric field term can be evaluated

$$\delta\varepsilon = -\frac{1}{10.8 Z_2 K_{sp}(x) T^{5/2}(x)} \int_{-\infty}^{\infty} \int_{E_{cr}}^{\infty} [j(x', E) - j(x, E)]\{k(x', E) \exp(-|H(x, x', E)|) \, dE \, dx'\} \tag{2.88}$$

where $j(x, E) = q(x, E)/E$. Combining everything the non-local heat flux is

$$q(x) = -\frac{1}{\beta(\infty, Z)} \left[\beta(E_{cr}/T, Z) + \frac{Z_4}{Z_2}\alpha(E_{cr}/T, Z)\right] K_{sp} T^{5/2} \frac{\partial T}{\partial x} + G \tag{2.89}$$

where

$$\alpha(y, Z) = \int_y^{\infty} \frac{\left(u - \frac{Z_4}{Z_2}\right) u^3 \exp(-u)}{B(u, Z)} du \tag{2.90}$$

and

$$G = \frac{1}{2} \int \int_{E_{cr}}^{\infty} q(x', E) \left(1 - \frac{Z_4 T(x)}{Z_2 E}\right) k(x', E) \exp(-|H|) \, dE \, dx'. \tag{2.91}$$

An alternative expression for heat flux can be derived by applying a pressure balance condition to determine the electric field. For gradual gradients, Colombant and Manheimer found that their model accurately reproduce the SH-flux. When applied to a steep gradient (Fig. 2.9a), the non-local model shows flux limiting and preheating in comparison to the SH flux indicating that non-local effects are being accounted for.

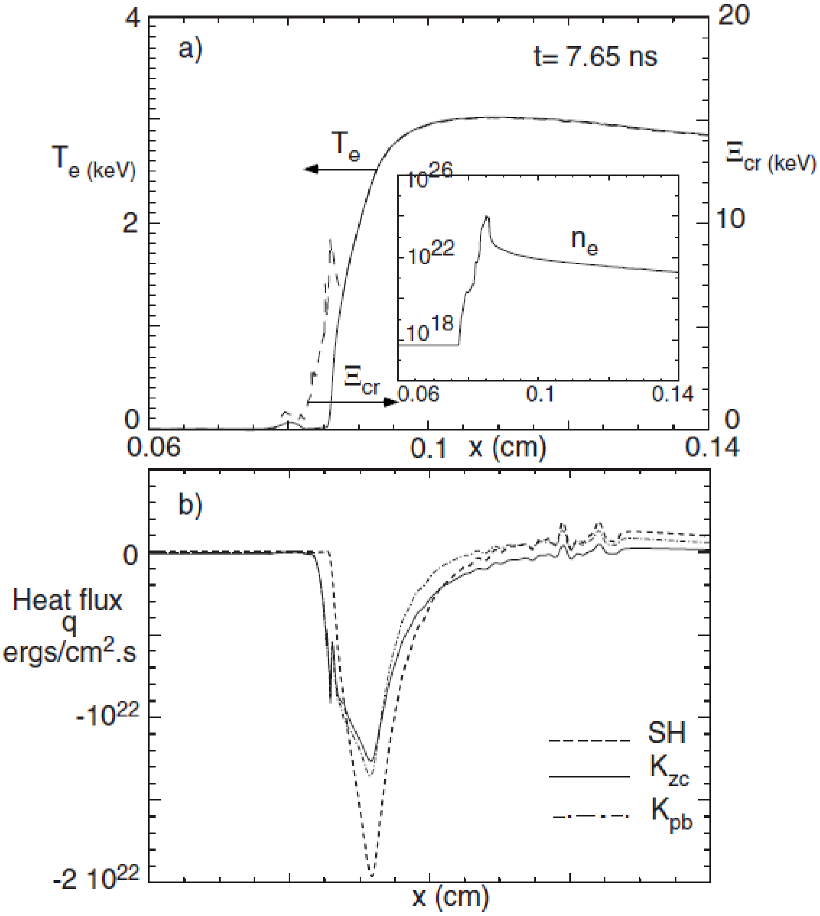

FIGURE 2.9: *(a) Density, temperature, and critical energy plots for simulation problem. (b) Plots of the Krook heat flux for zero current (solid) and pressure balance (dash-dot) conditions in comparison to the Spitzer-Harm flux (dashed) showing flux limiting and preheat [Figures obtained from [22]].*

Chapter 3

Theory

3.1 Derivation from Electron Transport Equation

We wish to derive a transport equation that can be used to compute the electron heat flux. The derivation begins with the steady state transport equation similarly to the second part of SNB paper

$$\mathbf{v} \cdot \nabla f - \frac{e}{m_e}\mathbf{E} \cdot \frac{\partial f}{\partial \mathbf{v}} = C(f) \tag{3.1}$$

where f is the electron distribution function, $\mathbf{E}$ is the electric field, and $C(f)$ is some collision operator. The electron distribution function is expanded as the sum of a the first order Maxwellian dominated solution given by SH theory and an additional correction term (note $\mathbf{r}$ and v dependence is suppressed):

$$f(\boldsymbol{\Omega}) = \Delta f(\boldsymbol{\Omega}) + f_0^{mb} + 3\boldsymbol{\Omega} \cdot \mathbf{f}_1^{mb} \tag{3.2}$$

where

$$\mathbf{f_1^{mb}} = \frac{v}{3\nu'_{ei}(v)}\left(\frac{m_e v^2}{2T_e} - 4\right) f_0^{mb}\frac{\nabla T_e}{T_e}. \tag{3.3}$$

Plugging the expanded distribution function into the transport equation Eq. 3.1 and expanding gives:

$$\begin{aligned} 0 =& - C(\Delta f(\boldsymbol{\Omega})) + v\boldsymbol{\Omega}\cdot\nabla(\Delta f(\boldsymbol{\Omega})) - \frac{e}{m_e}\mathbf{E}\cdot\frac{\partial \Delta f(\boldsymbol{\Omega})}{\partial \mathbf{v}} \\ & - \left[C(f_0^{mb})\right] \\ & + \left[-C(3\boldsymbol{\Omega}\cdot\mathbf{f}_1^{mb}) + v\boldsymbol{\Omega}\cdot\nabla(f_0^{mb}) - \frac{e}{m_e}\mathbf{E}^{mb}\cdot\boldsymbol{\Omega}\frac{\partial f_0^{mb}}{\partial v}\right] \\ & + v\boldsymbol{\Omega}\cdot\nabla(3\boldsymbol{\Omega}\cdot\mathbf{f}_1^{mb}) - \frac{3e\mathbf{E}}{m_e v^2}\frac{\partial v^2\mathbf{f}_1^{mb}}{\partial v} - \frac{e}{m_e}\Delta\mathbf{E}\cdot\boldsymbol{\Omega}\frac{\partial f_0^{mb}}{\partial v} \end{aligned} \tag{3.4}$$

where $\Delta\mathbf{E}$ is the non-local correction to the electric field. The two expressions in square brackets are both equal to zero. The first since collisions of a Maxwellian are in equilibrium and the second by the definition of the $\mathbf{f}_1^{mb}$ quantity, which uses a Lorentz approximation collision operator. Furthermore, we neglect the non-local correction to the electric field ($\mathbf{E} = \mathbf{E}^{mb}$). This simplifies the transport equation to:

$$\begin{aligned} -C(\Delta f(\boldsymbol{\Omega})) + v\boldsymbol{\Omega}\cdot\nabla(\Delta f(\boldsymbol{\Omega})) - \frac{e}{m_e}\mathbf{E}\cdot\frac{\partial \Delta f(\boldsymbol{\Omega})}{\partial \mathbf{v}} & \\ = - 3v\boldsymbol{\Omega}\cdot\nabla(\boldsymbol{\Omega}\cdot\mathbf{f}_1^{mb}) + 3\frac{e\mathbf{E}}{m_e v^2}\frac{\partial v^2\mathbf{f}_1^{mb}}{\partial v}. \end{aligned} \tag{3.5}$$

The transport equation can be further simplified by using a Krook collision operator ($C(\cdot) = -v/\lambda(v)\cdot$) and neglecting the electric field on the LHS of the equation (note these two approximations are made for the purpose of comparison with the SNB model and the more general case will be treated later). Furthermore, it is assumed the source term has the same functional form in velocity as the SNB model. Multiplying through by $\frac{1}{2}m_e v^4$ the equation can be cast into a transport equation in terms of

$$\Delta q(\mathbf{r}, \mathbf{\Omega}, v) = \frac{1}{2} m_e v^5 \Delta f(\mathbf{r}, \mathbf{\Omega}, v) \tag{3.6}$$

where $\Delta q(\mathbf{r}, \mathbf{\Omega}, v)$ is the angular heat flux correction. Namely,

$$\begin{aligned} \mathbf{\Omega} \cdot \nabla(\Delta q(\mathbf{r}, \mathbf{\Omega}, v)) + \frac{1}{\lambda(\mathbf{r}, v)} \Delta q(\mathbf{r}, \mathbf{\Omega}, v) & \\ = & - 3\mathbf{\Omega} \cdot \nabla(g(v)\mathbf{\Omega} \cdot \mathbf{Q}_{SH}(\mathbf{r})) \end{aligned} \tag{3.7}$$

where

$$g(v) = \frac{1}{12 v_{th}} \left(\frac{v}{v_{th}}\right)^9 \exp(-(v/v_{th})^2). \tag{3.8}$$

The heat flux $\mathbf{Q}$ is related to Δq via

$$\mathbf{Q}_{nl} = \mathbf{Q}_{sh} + \int_0^\infty \int_{4\pi} \Delta q(\mathbf{r}, \mathbf{\Omega}, v) \mathbf{\Omega} d\Omega dv. \tag{3.9}$$

Or alternatively

$$\begin{aligned} \nabla \cdot \mathbf{Q}_{nl} &= \nabla \cdot \mathbf{Q}_{sh} - \int_0^\infty \int_{4\pi} \frac{\Delta q(\mathbf{r}, \mathbf{\Omega}, v)}{\lambda(\mathbf{r}, v)} + 3\mathbf{\Omega} \cdot \nabla(g(v)\mathbf{\Omega} \cdot \mathbf{Q}_{SH}(\mathbf{r})) d\Omega dv \\ &= \nabla \cdot \mathbf{Q}_{sh} - \int_0^\infty \int_{4\pi} \frac{\Delta q(\mathbf{r}, \mathbf{\Omega}, v)}{\lambda(\mathbf{r}, v)} d\Omega dv - \nabla \cdot \mathbf{Q}_{sh} + \mathbf{J} \cdot \mathbf{E} \\ &= - \int_0^\infty \int_{4\pi} \frac{\Delta q(\mathbf{r}, \mathbf{\Omega}, v)}{\lambda(\mathbf{r}, v)} d\Omega dv. \end{aligned} \tag{3.10}$$

Putting the transport equation into multi-group form gives:

$$\mathbf{\Omega} \cdot \nabla(\Delta q_g(\mathbf{r}, \mathbf{\Omega})) + \frac{\Delta q_g(\mathbf{r}, \mathbf{\Omega})}{\lambda_g(\mathbf{r})} = -3\mathbf{\Omega} \cdot \nabla(\eta_g(\mathbf{r})\mathbf{\Omega} \cdot \mathbf{Q}_{SH}(\mathbf{r})) \tag{3.11}$$

where

$$\eta_g(\mathbf{r}) = \int_g g(v)dv = \frac{1}{24}\int_{E_{g-1/2}/kT_e(\mathbf{r})}^{E_{g+1/2}/kT_e(\mathbf{r})} \beta^4 \exp\left(-\beta\right)d\beta \tag{3.12}$$

and $E_{g\pm1/2}$ are the upper and lower bounds of energy group g. The heat flux divergence is:

$$\nabla\cdot\mathbf{Q}_{nl} = -\sum_g \int_{4\pi} \frac{\Delta q_g(\mathbf{r},\mathbf{\Omega})}{\lambda_g(\mathbf{r},\mathbf{\Omega})}d\Omega. \tag{3.13}$$

The transport equation mirrors the form of the iSNB equations with a streaming operator replacing the diffusion operator and the source term kept to higher order.

In the prior derivation we used a simple collision operator inversely proportional to the MFP. This operator however gives rise to exponentially decaying solutions similarly to the diffusion solution that result in greater preheat prediction. Charged particles however tend to have finite ranges and deposit most of their effective charge near the end of their range (Fig.˜3.1). This issue necessitates the usage of a different collision operator. Integrating Eq. 3.5 group-wise with $\frac{1}{2}m_e v^4$ and keeping the general collision operator gives

$$-\int_{v_g}^{v_{g+1}} \frac{1}{2}m_e v^4 C(\Delta f(\mathbf{r},\mathbf{\Omega},v))dv + \mathbf{\Omega}\cdot\nabla(\Delta q(\mathbf{r},\mathbf{\Omega},v)) = -3\mathbf{\Omega}\cdot\nabla(\eta_g\mathbf{\Omega}\cdot\mathbf{Q}_{SH}(\mathbf{r})) \tag{3.14}$$

which has a corresponding heat flux divergence given by

$$\nabla\cdot\mathbf{Q}_{nl} = \int_0^\infty \int_{4\pi} \frac{1}{2}m_e v^4 C(\Delta f(\mathbf{r},\mathbf{\Omega},v))d\Omega dv. \tag{3.15}$$

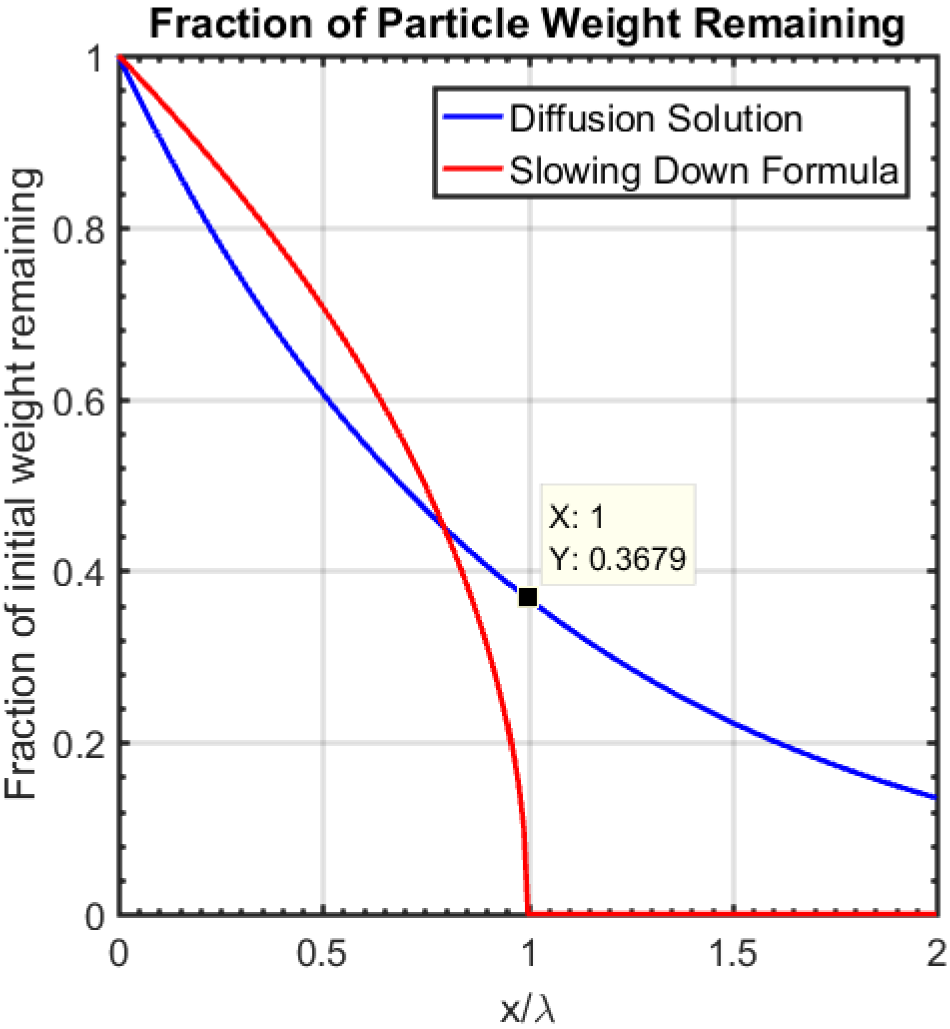

FIGURE 3.1: *Diffusion type solution compared to slowing down formula operator.*

Instead of a proportional collision operator a continuous slowing down operator can be used instead. Such an operator takes the form

$$C(f) = \frac{1}{m_e}\frac{\partial}{\partial v}\left(S(v)f(v)\right) \tag{3.16}$$

where $S(v)$ is the electron stopping power (dE/ds). Substituting in the continuous slowing down operator gives

$$\nabla \cdot \mathbf{Q}_{nl} = \int_0^\infty \int_{4\pi} \frac{1}{2} m_e v^5 \frac{1}{m_e v} \frac{\partial}{\partial v} (S(\mathbf{r}, v) \Delta f(\mathbf{r}, \boldsymbol{\Omega}, v)) d\Omega dv. \tag{3.17}$$

Discretizing the expression in velocity space and assuming the slowing down force varies slowly so that we may assume it constant over a single energy group gives

$$\nabla \cdot \mathbf{Q}_{nl} = -\sum_g \int_{4\pi} \frac{1}{\lambda_{g \to g-1}} (\Delta q_{g+1} - \Delta q_{g-1}) d\Omega. \tag{3.18}$$

Now that we have a transport equation we need a method to solve it. There are several ways in which to solve such equations using deterministic methods such as discrete ordinates or higher order Legendre expansions or statistical methods such as Monte Carlo (MC). We elected to use MC methods to solve our transport equation due to the presence of existing MC framework for radiation transport in the 2D DRACO code, which could be repurposed to our needs and reduce development time. MC methods have the further advantage in that they are highly parallelizable, which is useful for keeping simulation runtimes manageable.

3.2 Monte Carlo Algorithm

Defining the total number of MC particles n_{tot}, cell index i, j, group index g, volume of cell $V_{i,j}$, the transport equation 3.14 is solved via the following MC method.

1. $N_{i,j,g}$ particles are allocated to each energy group/cell in proportion to the isotropic source magnitude $|\nabla \cdot \mathbf{U}_g(\mathbf{r}_{i,j})|$ with a minimum of at least 1 per cell/group.

$$N_{i,j,g} = \left\lfloor N_{tot} \cdot \frac{|\nabla \cdot \mathbf{U}_g(\mathbf{r}_{i,j})|}{\sum_{i,j,g} |\nabla \cdot \mathbf{U}_g(\mathbf{r}_{i,j})|} \right\rfloor + 1 \tag{3.19}$$

2. Each particle is uniformly distributed within its cell volume and its direction $\mathbf{\Omega}_{birth}$ is uniformly sampled in 4π. The particle energy is sampled from the distribution

$$g(E) = \frac{1}{24}\left(\frac{E}{kT_e}\right)^4 \exp\left(\frac{E}{kT_e}\right). \tag{3.20}$$

3. Initial particle weight in cell i, j is given by

$$\frac{s_g(\mathbf{r_{i,j}}, \mathbf{\Omega})}{N_{i,j,g}} \cdot V_{i,j} \tag{3.21}$$

   where s_g is the transport equation source term.

4. The distances to boundary, collision, and downscattering interactions are sampled and the distance to the closest interaction (d_{min}) is selected.

   - Boundary: In $r - z$ the cell boundaries are conical so a quadratic equation is solved to calculate the distance $d_{boundary}$ to intersection between the boundary and the straight line path of the particle. Furthermore, for straight line paths a range is computed for each cell and if the range is less than the distance to boundary the particle history can be terminated (range rejection) improving computational efficiency.
   - Collision: More on this later.
   - Downscattering: The distance to the lower energy group bound $E_{g-1/2}$ is calculated via

$$d_{downscatter} = \frac{E_{g-1/2} - E_{current}}{dE/ds}. \tag{3.22}$$

5. Particle energy is reduced by

$$\Delta E = \frac{dE}{ds}\left(\mathbf{r}_{i,j}, E_g\right) \cdot d_{min} \tag{3.23}$$

using the slowing down formula in Atzeni 2009 [19].

6. The particle's weight is reduced by $|\Delta E/E_{birth}| \cdot W_{birth}$ and the current cell's tally is increased by the same amount.
7. Particle history is terminated when either the particle weight falls below a fixed fraction of its initial weight or its energy is depleted.

After all particles are transported, $\nabla \cdot \mathbf{Q}_{nl}$ is recovered by summation of the tallies over all groups and then dividing the total by the cell volume. The process can then be iterated via the iSNB implicit algorithm [17] until the temperature solution is converged.

3.3 Electric Field Treatment

The transport method differs from the diffusion method in that it can model particle trajectories. As such the transport method is able model electric field effects. The SNB method includes a correction to the diffusion coefficient based on the electric field correction to the LMV kernel in [23] to account for some electric field effects via

$$\frac{1}{\lambda_e'} = \frac{1}{\lambda_e} + \frac{|e\mathbf{E_{mb}}|}{k_b T_e} \tag{3.24}$$

where $\lambda_E = k_b T_e/|e\mathbf{E_{mb}}|$ is the maximum distance an electron of energy T_e can travel in a direction opposed to the electric field. The downside to this correction is that it is non-directional and limits the electron range regardless of whether the particle is traveling with or against the electric field.

For the transport method, we wish to model how the trajectory of the MC particle is modified by the electric field. Two forces act upon the particle. The first is the frictional slowing down force which acts opposed to the direction of motion, the second is the force due to the electric field. For the slowing down force we use the stopping power as before. For the electric field we use the relation derived from SH theory

$$\mathbf{E}_{mb} = \frac{kT_e}{e}\left(\frac{\nabla n_e}{n_e} + \gamma\frac{\nabla T_e}{T_e}\right) \tag{3.25}$$

where $\gamma = 1 + 3/2(Z + 0.477)/(Z + 2.15)$. In the presence of an electric field the MCP will travel in a curved path, which increases the computation cost particularly in computing boundary crossings. In order to mitigate this somewhat we allow the particle to travel in a straight line trajectory and then correct the angle at the end of the Δs step to account for the contribution of $E_\perp$. This necessitates a limit to restrict the angular deflection at each step. For each spatial step the forces acting on the MCP are split into their parallel and perpendicular components. The electric force is

$$\mathbf{F}_E = -e\mathbf{E} \tag{3.26}$$

with parallel component

$$F_{E\parallel} = -e\mathbf{E}\cdot\mathbf{\Omega} = F_E\mu \tag{3.27}$$

and perpendicular component

$$F_{E\perp} = \left|-e\mathbf{E} + (e\mathbf{E}\cdot\mathbf{\Omega})\,\mathbf{\Omega}\right| = F_E\sqrt{1-\mu^2} \tag{3.28}$$

with the perpendicular basis vector of

$$\mathbf{\Omega}_\perp = \frac{-e\mathbf{E} + (e\mathbf{E}\cdot\mathbf{\Omega})\mathbf{\Omega}}{F_E\sqrt{1-\mu^2}}. \tag{3.29}$$

Adding the parallel electric and stopping power forces gives a total force in the parallel direction of

$$F_{\|} = \frac{dE}{ds} + F_{E\|}. \tag{3.30}$$

For $F_{\|}$ negative the particle will be downscattered and for $F_{\|}$ positive the particle will be upscattered. As such, in low density high temperature regions particles can experience orbits.

Computing where the electric force exceeds 1% of the slowing down in Fig 3.2 it is apparent that electric field plays its most significant role in low density regions and in the higher energy groups. As such we expect to see the largest differences in the corona or out ahead of the shell. Figs. 3.3 and 3.4 depict example trajectories for single particles under realistic plasma conditions with and without the influence of an electric field in the coronal plasma (generated via a standalone Matlab script). In Fig. 3.3 the sample particle exhibits a large amount of orbital behavior. In Fig. 3.4, the electric field deflects the particle trajectory inwards bringing it closer to the dense shell resulting in a shorter path length than the trajectory under slowing down only. The single particle tallies for the trajectories in Fig 3.4 are seen in Fig. 3.5 in which there appear to be significant differences between the two treatments.

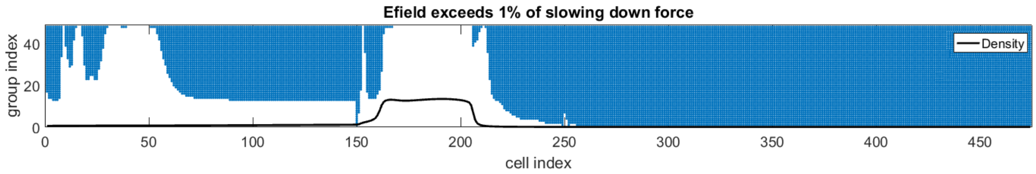

Figure 3.2: *List of cells/groups in which the electric field exceeds 1% of the slowing down force. The electric field has the most influence in regions where the density (black) is lowest in particular the corona and the least influence in the high density shell.*

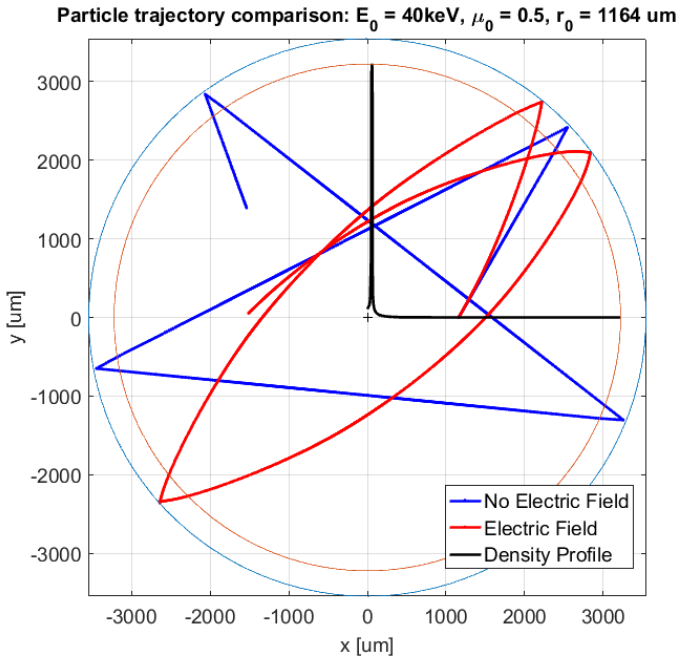

FIGURE 3.3: *Single electron MCP trajectory for an electron starting in the highest energy group (40 keV) depicting a curved trajectory due to the electric field influence and orbiting behavior*

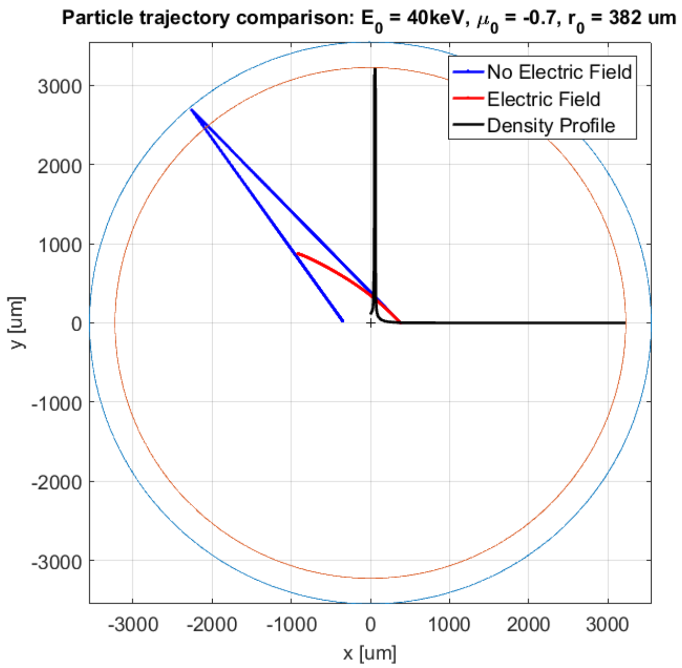

FIGURE 3.4: *Single electron MCP trajectory for an electron starting in the highest energy group (40 keV) depicting a curved trajectory due to the electric field influence. The electric field influenced trajectory has a shorter path due to deflection closer to the high density shell region.*

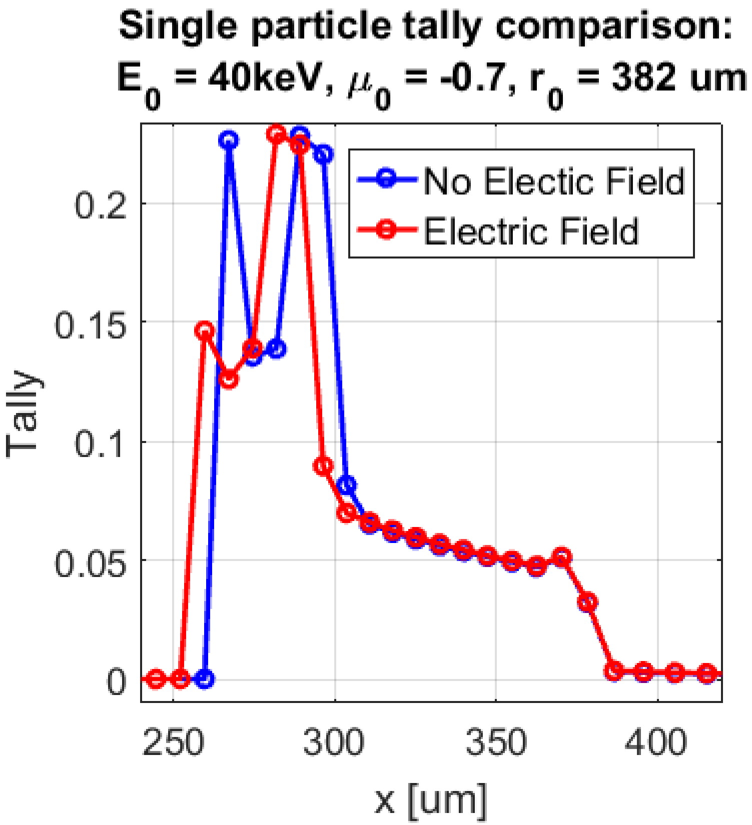

FIGURE 3.5: *Tally comparison for particle trajectories depicted in Fig. 3.4.*

Such orbital behavior can however be undesirable for calculation since it can take multiple orbits for a particle to complete its history and allows for runaway electrons, significantly increasing the computational run time. In order to avoid this issue we allow only decaying orbits to occur by imposing the artificial constraint that $F_{\|}$ is strictly negative. Namely, for each energy group we impose an upper limit on F_E of

$$F_E^g = \min\left(-\frac{dE}{ds}\bigg|_g, F_E\right). \tag{3.31}$$

For a particle in group g, bounded by velocities $v_{g-1/2}$ and $v_{g+1/2}$ and with initial velocity

v_i, the equations of motion are

$$mv_{\parallel}^{f} = mv_i + F_{\parallel}^{g} \cdot t \tag{3.32}$$

and

$$mv_{\perp}^{f} = 0 + F_{\perp}^{g} \cdot t. \tag{3.33}$$

We want to limit the deflection angle to around $\delta = 0.1$ rad (6°) so that the assumption that the slowing down formula is only in the initial particle direction remains valid. Also this limits the fraction of perpendicular kinetic energy to $\delta^2 = 0.01$. (Note: one might want to be more restrictive to take into account energy group spacing). Using the equations of motion, the angular deflection θ is well approximated by

$$\theta \approx \tan(\theta) = \frac{v_{\perp}^{f}}{v_{\parallel}^{f}} = \frac{F_{\perp}^{g} \cdot t}{mv_i + F_{\parallel}^{g} \cdot t} < \frac{F_{\perp}^{g} \cdot t}{mv_{g-1/2}}. \tag{3.34}$$

Setting the limit δ equal to this upper bound gives a time to deflection of

$$t_{\perp} = \delta \cdot \frac{mv_{g-1/2}}{F_{\perp}^{g}}. \tag{3.35}$$

(Note: This is slightly more restrictive than need be since it uses the lower group bound velocity, but doing this avoids the extra computation cost of simultaneously solving the perpendicular and parallel equations. Also, for group 1 the lower group bound is zero so we recommend neglecting the electric field for this group [the stopping force is likely to greatly exceed the electric field there anyway]). In terms of travel distance in the parallel distance the deflection limit is

$$d_{deflection} = t_{\perp} \cdot \left(v_i + t_{\perp} \frac{F_{\parallel}^{g}}{2m} \right). \tag{3.36}$$

Due to the parabolic nature of this distance formula it is possible for invalid distances to occur if $t_\perp$ produces a result after the parabola's peak. Specifically we must require that

$$t_\perp = \delta \cdot \frac{mv_{g-1/2}}{F_\perp^g} < \frac{mv_i}{|F_\parallel^g|} \tag{3.37}$$

or

$$\delta < \left[\frac{v_i}{v_{g-1/2}}\right] \left|\frac{F_\perp^g}{F_\parallel^g}\right|. \tag{3.38}$$

A more restrictive condition can be derived by comparing the time to deflection to the time to downscattering. Namely if

$$\delta < \left[\frac{v_i}{v_{g-1/2}} - 1\right] \left|\frac{F_\perp^g}{F_\parallel^g}\right| \tag{3.39}$$

then deflection is more limiting than downscattering, otherwise downscattering is more restrictive then deflection. If downscattering is limiting the downscattering limit is calculated via the parallel equation to be

$$d_{D.S.} = \frac{E_{g-1/2} - E_i}{F_\parallel^g}. \tag{3.40}$$

Once the most limiting interaction is found the particle is advanced. The energy is updated via

$$\Delta E = F_\parallel^g \cdot d_{min} \tag{3.41}$$

and if a downscattering or a boundary event occurs the appropriate index is modified. The particle direction is deflected by an angle of θ in the plane defined by $\mathbf{\Omega}$ and $\mathbf{\Omega}_\perp$. The scattering angle is well approximated by

$$\theta = \frac{v_\perp^f}{v_\parallel^f} = \frac{F_\perp^g \cdot t}{mv_i + F_\parallel^g \cdot t} \tag{3.42}$$

where t is

$$t = \frac{2 \cdot d_{min}}{v_i + v_f}. \tag{3.43}$$

The updated direction vector is

$$\mathbf{\Omega}_f = \mathbf{\Omega} \cos\theta + \mathbf{\Omega}_\perp \sin\theta. \tag{3.44}$$

Other than these modifications the MC algorithm precedes as described in the previous section. It should be noted that in practice, most of the heat flux divergence is confined to regions near the temperature and density gradients close to the dense shell where the effects of the electric field are relatively weaker. As such, inclusion of the electric field seems to only have a small effect on the overall integrated simulation results.

3.3.1 Specifics for r-z coordinates:

In the DRACO code the MCP position and angular variables are stored in Cartesian coordinates.

$$\mathbf{E} = E_r\hat{\mathbf{r}} + E_z\hat{\mathbf{z}} = E_r(\cos\varphi\hat{\mathbf{x}} + \sin\varphi\hat{\mathbf{y}}) + E_z\hat{\mathbf{z}} \tag{3.45}$$

where $\cos\varphi = x/\sqrt{x^2+y^2}$ and $\sin\varphi = y/\sqrt{x^2+y^2}$. Defining

$$\hat{\mathbf{e}} = -\mathbf{E}/|\mathbf{E}| = e_r\hat{\mathbf{r}} + e_z\hat{\mathbf{z}} \tag{3.46}$$

as the electric force direction and

$$\mathbf{\Omega} = \mu_x\hat{\mathbf{x}} + \mu_y\hat{\mathbf{y}} + \mu_z\hat{\mathbf{z}} \tag{3.47}$$

as the particle direction:

$$F_E = e\sqrt{E_r^2 + E_z^2} \tag{3.48}$$

and

$$\mu = \hat{\mathbf{e}} \cdot \mathbf{\Omega} = e_r(\mu_x \cos\varphi + \mu_y \sin\varphi) + e_z\mu_z. \tag{3.49}$$

The directional component of the electric force perpendicular to the particle's direction is

$$\mathbf{\Omega}_\perp = \frac{\hat{\mathbf{e}} - \mu\mathbf{\Omega}}{\sqrt{1-\mu^2}}, \tag{3.50}$$

For the scattering of the particle by an angle of θ in the $\mathbf{\Omega}$ $\mathbf{\Omega}_\perp$ plane we have

$$\mathbf{\Omega}' = \mathbf{\Omega}\cos\theta + \mathbf{\Omega}_\perp \sin\theta \tag{3.51}$$

which expands to

$$\begin{aligned}
\mu'_x &= \mu_x \cos\theta + \frac{(e_r\cos\varphi - \mu\mu_x)}{\sqrt{1-\mu^2}}\sin\theta, \\
\mu'_y &= \mu_y \cos\theta + \frac{(e_r\sin\varphi - \mu\mu_y)}{\sqrt{1-\mu^2}}\sin\theta, \\
\mu'_z &= \mu_z \cos\theta + \frac{(e_z - \mu\mu_z)}{\sqrt{1-\mu^2}}\sin\theta.
\end{aligned} \tag{3.52}$$

3.4 Hybrid Modeling

In order to maximize code efficiency it is important to only run transport for cells/groups in which the MFP is larger than the cell size length. Doing this allows for low energy short MFP particles to be run with the faster iSNB diffusion algorithm while freeing up MCPs for use in long MFP regions. In Fig. 3.6 a couple of metrics are plotted in order to show where transport is most important spatially. For this plot in each energy group the MFP was compared to the cell size and then the total fraction of the source term in each cell requiring a transport treatment (bottom left) and the number of energy groups in each cell requiring a transport treatment (bottom right) were plotted. As can be seen, transport is least important in regions near to the dense shell and most important in low density or high temperature regions such as the corona. As $\nabla \cdot \mathbf{Q}$ tends to be greatest near the spatial gradients close to the dense shell, it appears that significant savings may be gained by hybrid method usage.

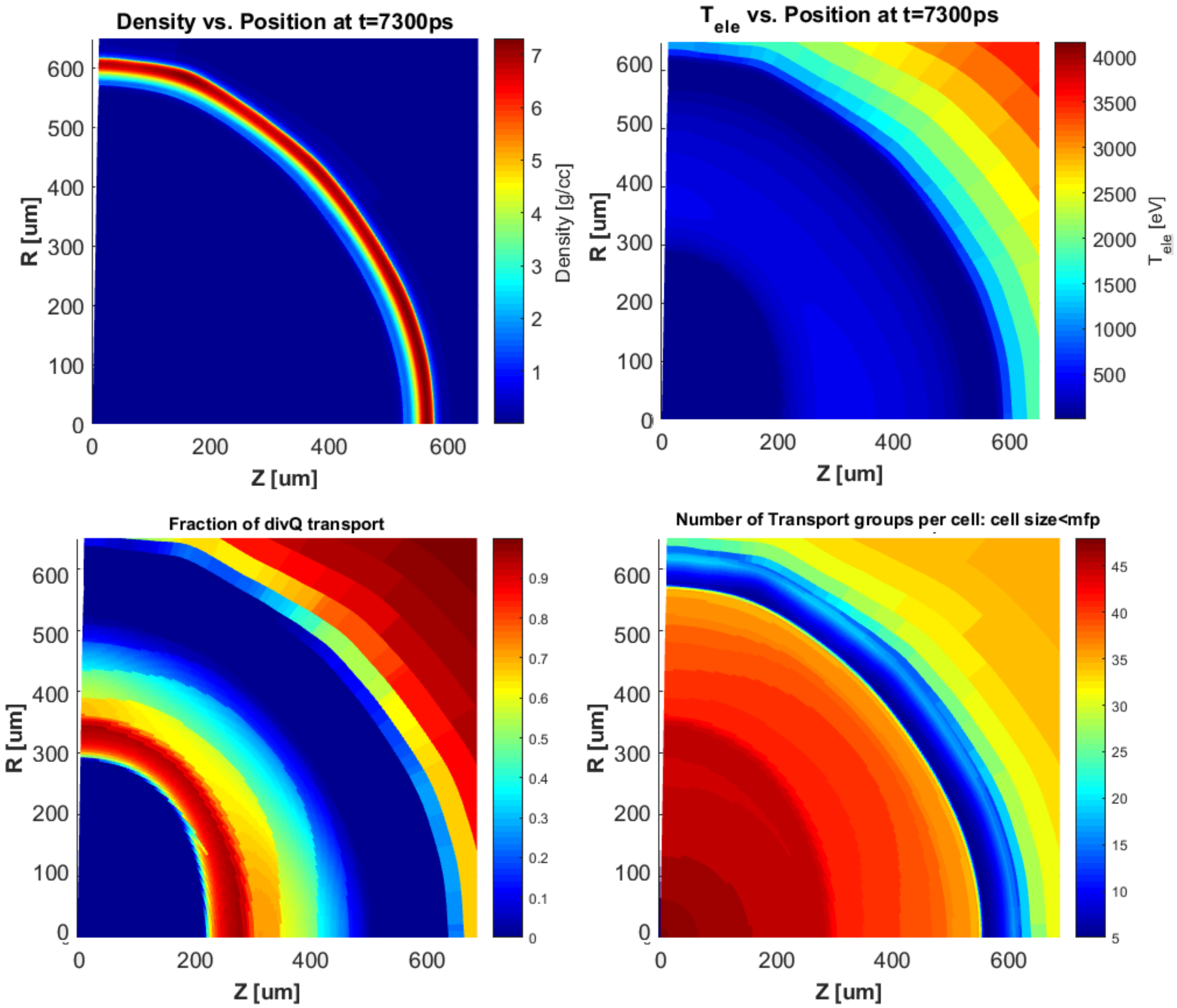

FIGURE 3.6: *Density distribution (top left), electron temperature distribution (top right), the proportion of the heat flux divergence in each cell requiring transport treatment (bottom left), the number of groups in each cell requiring transport treatment (bottom right).*

For the hybrid method, in each cell and energy group the MFP $\lambda_{i,j,g}$ is compared to the cell size $L_{i,j}$ (defined as the minimum side or diagonal length of the quadrilateral cell in RZ geometry). For $L_{i,j}/\lambda_{i,j,g}$, ratios greater than some cutoff ratio (a minimum of 3 seems to work) particles will largely remain within the influence of their source cell and will consequently behave diffusively. For low ratios the cell is optically thin and the particle will exhibit transport like behavior instead. The hybrid method is accomplished via replacement of step 4 and 5 of the iSNB iterative algorithm (Section 2.1.3) with the following.

- For each cell/group determine

$$\delta^{tr}_{i,j,g} = \begin{cases} 0 & \text{if} \quad \lambda_{i,j,g} \cdot \tau_{cutoff} < L_{i,j} \\ 1 & \text{otherwise} \end{cases} \tag{3.53}$$

  where τ_{cutoff} is a user set parameter (≥ 3) that defines the minimum optical depth for diffusion to occur.

- Solve the diffusion equation with reduced source term

$$\left(\frac{1}{\lambda_g(\mathbf{r})} - \nabla\frac{\lambda_g(\mathbf{r})}{3}\nabla\right) H_g(\mathbf{r}) = -(1-\delta^{tr}_{i,j,g}) \cdot \nabla \cdot \mathbf{U}^k_g. \tag{3.54}$$

- Solve the transport equation with reduced source term

$$\begin{aligned} &\mathbf{\Omega} \cdot \nabla(\Delta q_g(\mathbf{r},\mathbf{\Omega})) + \frac{1}{\lambda_g(\mathbf{r})}\Delta q_g(\mathbf{r},\mathbf{\Omega}) \\ &\qquad\qquad = -3 \cdot \delta^{tr}_{i,j,g} \cdot \mathbf{\Omega} \cdot \nabla(\mathbf{\Omega} \cdot \mathbf{U}_g(\mathbf{r})). \end{aligned} \tag{3.55}$$

- Calculate the hybrid $\nabla \cdot \mathbf{Q}$ solution by adding the reduced source diffusion and transport solutions

$$\nabla \cdot \mathbf{Q}^k_{nl}(\mathbf{r}) = -\sum_g \frac{1}{\lambda_g(\mathbf{r})}\left(H_g(\mathbf{r}) + \int_{4\pi} \Delta q_g(\mathbf{r},\mathbf{\Omega}) d\Omega\right). \tag{3.56}$$

The solutions can be combined linearly like this because of the mirrored forms of the iSNB and transport equations. Note the diffusion equation is solved via deterministic diffusion solver and the transport equation is solved via Monte Carlo. As such MCPs originating in the transport regions that travel to diffusive regimes continue to receive full MC treatment instead of a simplified diffusion treatment.

3.5 Theory Summary

In summary, the transport equation

$$-\int_{v_g}^{v_{g+1}} \frac{1}{2} m_e v^4 C(\Delta f(\mathbf{r}, \mathbf{\Omega}, v)) dv + \mathbf{\Omega} \cdot \nabla(\Delta q(\mathbf{r}, \mathbf{\Omega}, v)) = -3\mathbf{\Omega} \cdot \nabla(\eta_g \mathbf{\Omega} \cdot \mathbf{Q}_{SH}(\mathbf{r})) \tag{3.57}$$

is solved for non-local heat flux divergence given by

$$\nabla \cdot \mathbf{Q}_{nl} = \int_0^\infty \int_{4\pi} \frac{1}{2} m_e v^4 C(\Delta f(\mathbf{r}, \mathbf{\Omega}, v)) d\Omega dv \tag{3.58}$$

via the following MC algorithm.

Defining the total number of MC particles n_{tot}, cell index i, j, group index g, volume of cell $V_{i,j}$, and the parallel and perpendicular forces acting on a particle with energy in group g as $F_{\parallel}^g$ and $F_{\perp}^g$, the transport equation 3.57 is solved via MC method as follows:

1. $N_{i,j,g}$ particles are allocated to each energy group/cell in proportion to the isotropic source magnitude $|\nabla \cdot \mathbf{U}_g(\mathbf{r}_{i,j})|$ with a minimum of at least 1 per cell/group.

$$N_{i,j,g} = \left\lfloor N_{tot} \cdot \frac{|\nabla \cdot \mathbf{U}_g(\mathbf{r}_{i,j})|}{\sum_{i,j,g} |\nabla \cdot \mathbf{U}_g(\mathbf{r}_{i,j})|} \right\rfloor + 1 \tag{3.59}$$

Note: in the hybrid method we only compute this in cells which are optically thin enough (<3 MFPs wide) to require transport.

2. Each particle is uniformly distributed within its cell volume and its direction $\mathbf{\Omega}_{birth}$ is uniformly sampled in 4π. The particle energy is sampled from the distribution

$$g(E) = \frac{1}{24}\left(\frac{E}{kT_e}\right)^4 \exp\left(\frac{E}{kT_e}\right). \tag{3.60}$$

3. Initial particle weight in cell i, j is given by

$$W_{birth} = \frac{s_g(\mathbf{r}_{i,j}, \mathbf{\Omega}_{birth})}{N_{i,j,g}} \cdot V_{i,j} \tag{3.61}$$

   where s_g is the transport equation source term.

4. The distances to boundary, angular deflection, and downscattering interactions are sampled and the distance to the closest interaction (d_{min}) is selected.

   - Boundary: The distance to cell boundary is calculated using the particle's straight line trajectory.
   - For the downscattering and electric field angular deflection interactions the choice of limiting interaction is related.
     - If

$$\delta < \left[\frac{v_i}{v_{g-1/2}} - 1\right]\left|\frac{F_\perp^g}{F_\parallel^g}\right| \tag{3.62}$$

       where δ is the angular deflection limit (recommend value 0.1) then angular deflection due to the electric field is more limiting than downscattering and we use

$$d_{deflection} = t_\perp \cdot \left(v_i + t_\perp \frac{F_\parallel^g}{2m}\right) \qquad \text{Deflection Limit} \tag{3.63}$$

where

$$t_\perp = \delta \cdot \frac{mv_{g-1/2}}{F_\perp^g}. \tag{3.64}$$

- Otherwise downscattering is more limiting than electric field angular deflection and we use

$$d_{D.S.} = \frac{E_{g-1/2} - E_i}{F_\parallel^g} \qquad \text{Downscattering Limit} \tag{3.65}$$

5. The particle is moved by d_{min} in its initial direction.

6. Particle energy changes by

$$\Delta E = F_\parallel^{i,j,g} \cdot d_{min}. \tag{3.66}$$

7. Particle direction is rotated by an angle of θ in the plane of $\mathbf{F}_\parallel^g$ and $\mathbf{F}_\perp^g$.

$$\theta = \frac{v_\perp^f}{v_\parallel^f} = \frac{F_\perp^g \cdot t}{mv_i + F_\parallel^g \cdot t} \tag{3.67}$$

where t is

$$t = \frac{2 \cdot d_{min}}{v_i + v_f}. \tag{3.68}$$

8. The particle's weight is reduced by $|\Delta E / E_{birth}| \cdot W_{birth}$ and the current cell's tally is increased by the same amount.

9. Particle history is terminated when either the particle weight falls below a fixed fraction of its initial weight or its energy is depleted.

After all particles are transported, $\nabla \cdot \mathbf{Q}_{nl}$ is recovered by summation of the tallies over all groups and then dividing the total by the cell volume. The process can then be iterated via the iSNB implicit algorithm (repeated below) [17] until the temperature solution is converged.

The iSNB iterative algorithm for the transport equation is as follows:

1. Solve the temperature equation for $T_e^{(k)}$

   $$\rho C_v \frac{T_e^k - T_e^n}{\Delta t} = -\nabla \cdot \mathbf{Q}_{sh}^k + S_{ext}^n + S_{nl,correction}^{k-1} \tag{3.69}$$

   where k is the iterative index, K_{SH}^n is the coefficient in the SH flux, $S_{nl,correction}^{k-1}$ is the SNB correction to the SH flux, and $S_{nl,correction}^0 = 0$.

2. Recompute $\nabla \cdot \mathbf{Q}_{sh}^k$ using T_e^k.

3. If $k > 1$, check for convergence with criterion

   $$|\nabla \cdot \mathbf{Q}_{sh}^k - \nabla \cdot \mathbf{Q}_{sh}^{k-1}| \leq \alpha \rho C_{v,e} \frac{T_e^k}{\Delta t} \tag{3.70}$$

   where α is a user defined parameter set to $\alpha = 0.01$. Cao recommends only checking convergence in cells with a density greater than 1×10^{-4} g/cm^3. If converged, set $T_e^{n+1} = T_e^{(k)}$ and exit the loop and advancing to the next time step.

4. If not converged

   - For pure transport: solve the transport equation via the above MC algorithm

     $$-\int_{v_g}^{v_{g+1}} \frac{1}{2} m_e v^4 C(\Delta f(\mathbf{r}, \mathbf{\Omega}, v)) dv + \mathbf{\Omega} \cdot \nabla(\Delta q(\mathbf{r}, \mathbf{\Omega}, v)) = -3\mathbf{\Omega} \cdot \nabla(\eta_g \mathbf{\Omega} \cdot \mathbf{Q}_{SH}(\mathbf{r})) \tag{3.71}$$

     where g is the group index and $\beta_g = E_g/kT$.

   - For the hybrid method: solve the reduced source term transport and diffusion equations via their respective solvers

$$-\int_{v_g}^{v_{g+1}} \frac{1}{2} m_e v^4 C(\Delta f(\mathbf{r}, \mathbf{\Omega}, v))dv + \mathbf{\Omega} \cdot \nabla(\Delta q(\mathbf{r}, \mathbf{\Omega}, v)) = -3 \cdot \delta^{tr}_{i,j,g} \cdot \mathbf{\Omega} \cdot \nabla(\eta_g \mathbf{\Omega} \cdot \mathbf{Q}_{SH}(\mathbf{r})) \tag{3.72}$$

$$\left(\frac{1}{\lambda_g(\mathbf{r})} - \nabla \frac{\lambda_g(\mathbf{r})}{3} \nabla \right) H_g(\mathbf{r}) = -(1 - \delta^{tr}_{i,j,g}) \cdot \nabla \cdot \mathbf{U}^k_g \tag{3.73}$$

where $\delta^{tr}_{i,j,g}$ is 0 for cells/groups that are optically thick enough for diffusion and 1 otherwise.

5. Compute $\nabla \cdot \mathbf{Q}_{nl}$

   - For pure transport: the solution is given via the tallied solution to the MC algorithm
   $$\nabla \cdot \mathbf{Q}^k_{nl}(\mathbf{r}) = -\sum_g \frac{1}{\lambda_g(\mathbf{r})} \int_{4\pi} \Delta q_g(\mathbf{r}, \mathbf{\Omega}) d\Omega. \tag{3.74}$$

   - For the hybrid method: the solution is the sum of the reduced source deterministic diffusion and MC transport solutions
   $$\nabla \cdot \mathbf{Q}^k_{nl}(\mathbf{r}) = -\sum_g \frac{1}{\lambda_g(\mathbf{r})} \left(H_g(\mathbf{r}) + \int_{4\pi} \Delta q_g(\mathbf{r}, \mathbf{\Omega}) d\Omega \right). \tag{3.75}$$

6. Compute
$$S^{(k)}_{nl,correction} = -\nabla \cdot \mathbf{Q}^k_{nl} + \nabla \cdot \mathbf{Q}^k_{sh}. \tag{3.76}$$

7. Repeat from Step 1 for the next iteration of k.

Chapter 4

Simulations and Results

The MC model, hereafter ETTMC (Electron Thermal Transport Monte Carlo), was tested with several realistic simulations in both the 1D LILAC and 2D DRACO codes against currently existing methods in the code, the iSNB diffusion method in 1D and 2D and Goncharov's method in 1D. The integrated results of these simulations indicate that the diffusion based iSNB method is adequate for these experimental conditions. This is because the ETTMC transport method yields similar results to the iSNB method.

4.1 1D Simulations

4.1.1 Omega shot 60303: shock timing experiment

Shot 60303 was a cryogenic target shot on LLE's OMEGA laser system [18]. The primary purpose of this experiment was to measure the shock convergence within a target. Shock velocity was measured using a Velocity Interferometer System for Any Reflector (VISAR) device on which the target was mounted (Fig. 4.1). The target consisted of a deuterated plastic shell and an inner liquid deuterium layer. The laser profile consisted of three laser pickets followed by a main drive (Fig. 4.2). Since each laser picket is successively larger the shocks catch up to each other at which point there is a marked increase in the shock velocity.

Simulation of this shot was done in LLE's 1D LILAC code, the simulation in 1D spherical geometry consisted of an innermost 23.5 micron thick 10 cell region of DD gas at 4.5×10^{-4} g/cm^3 density, followed by a middle layer of 400 micron thick 400 cell region of DD liquid at 0.17 g/cm^3 density, and an outermost 9.5 micron thickness layer consisting of 220 cell region of deuterated plastic at density 0.985 g/cm^3 (Fig. 4.3).

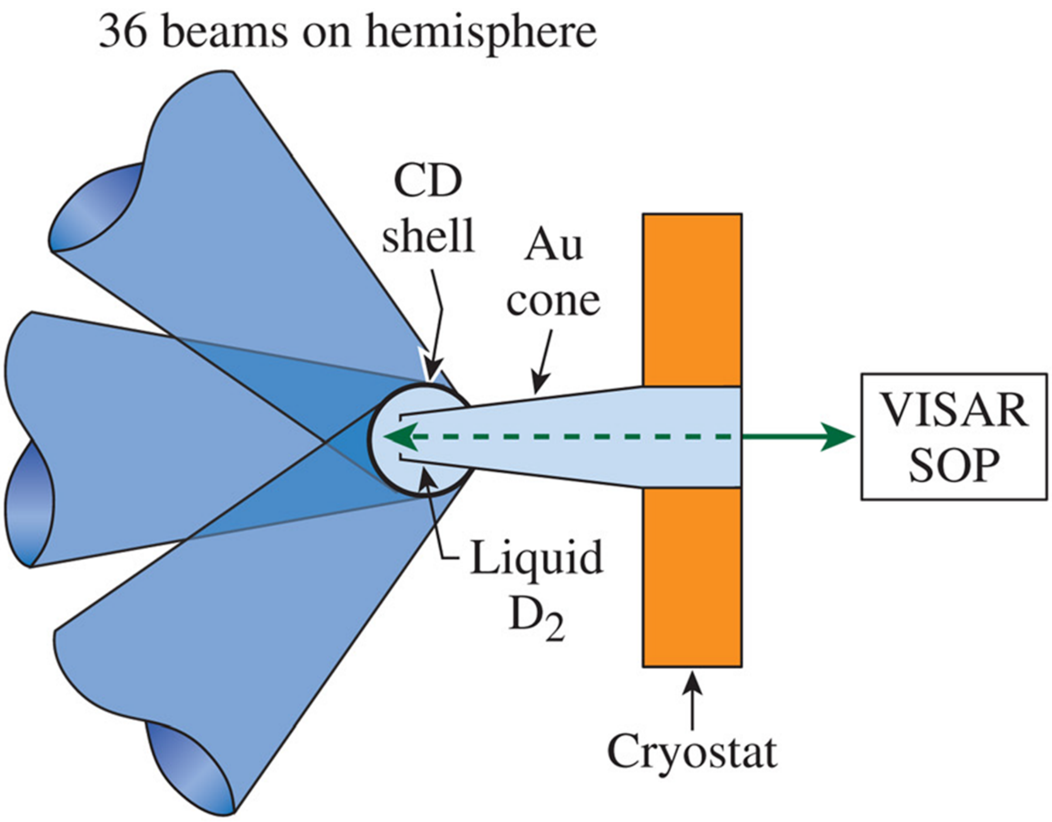

Figure 4.1: *Diagram depicting the experimental setup for the Omega shot 60303 shock timing experiment. 36 beams illuminate a hemisphere of the target[Figure obtained from Boehly 2011[18]].*

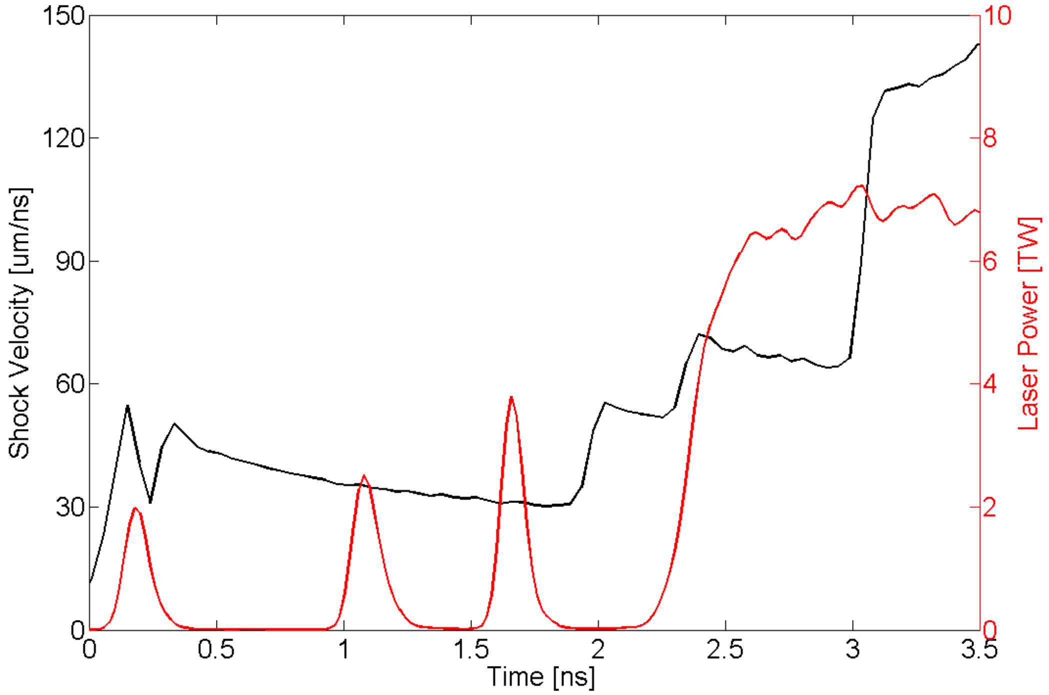

Figure 4.2: *Measured shock velocity (black) and laser power (red) for Omega shot 60303 [Figure obtained from Cao 2015 [17]].*

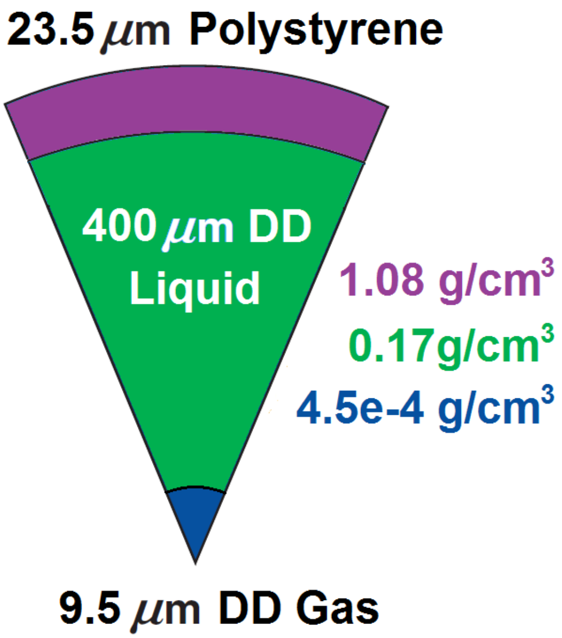

FIGURE 4.3: *Cross section of the target capsule for Omega shot 60303.*

Simulations seem to indicate that an average of 10 MCP per cell/group minimum is sufficient for a convergent solution of the $\nabla \cdot \mathbf{Q}_{nl}$ quantity. The effect of number of source MCPs on the statistical convergence of $\nabla \cdot \mathbf{Q}$ is demonstrated in Fig. 4.4. For this comparison a single time step of the shot 60303 simulation was computed with a differing number of source MCPs and the resultant non-local heat flux divergence is plotted. As can be seen, the statistical noise in the $\nabla \cdot \mathbf{Q}$ quantity decreases with a higher particle count. Near the outer edge of the dense cell (near 273 μm), there is a significant difference between the 1 MCP/cell-group and higher particle count calculations. As this region contributes to heating the dense shell and thus preheating it is important to model correctly. The 10 MCP/cell-group and above calculations produce similar results across the entire domain therefore we recommend a minimum of at least a 10 MCP per cell/group average in order to achieve converged results. Ideally the more particles used the better the MC statistics (Error $\sim 1/\sqrt{\#MCPs}$), however this must be balanced with considerations for the total simulation runtime (Runtime $\sim \#MCPs$). Note that since many of the cells fall outside of the gradient region they have a low importance to calculating the solution and as such have less than the average number of MCP. Since $\nabla \cdot \mathbf{Q}_{nl}$ is orders of magnitude larger nearest to the material gradients the low number of MCP in the other cells (and resultant higher variance) does not appreciably affect the overall solution.

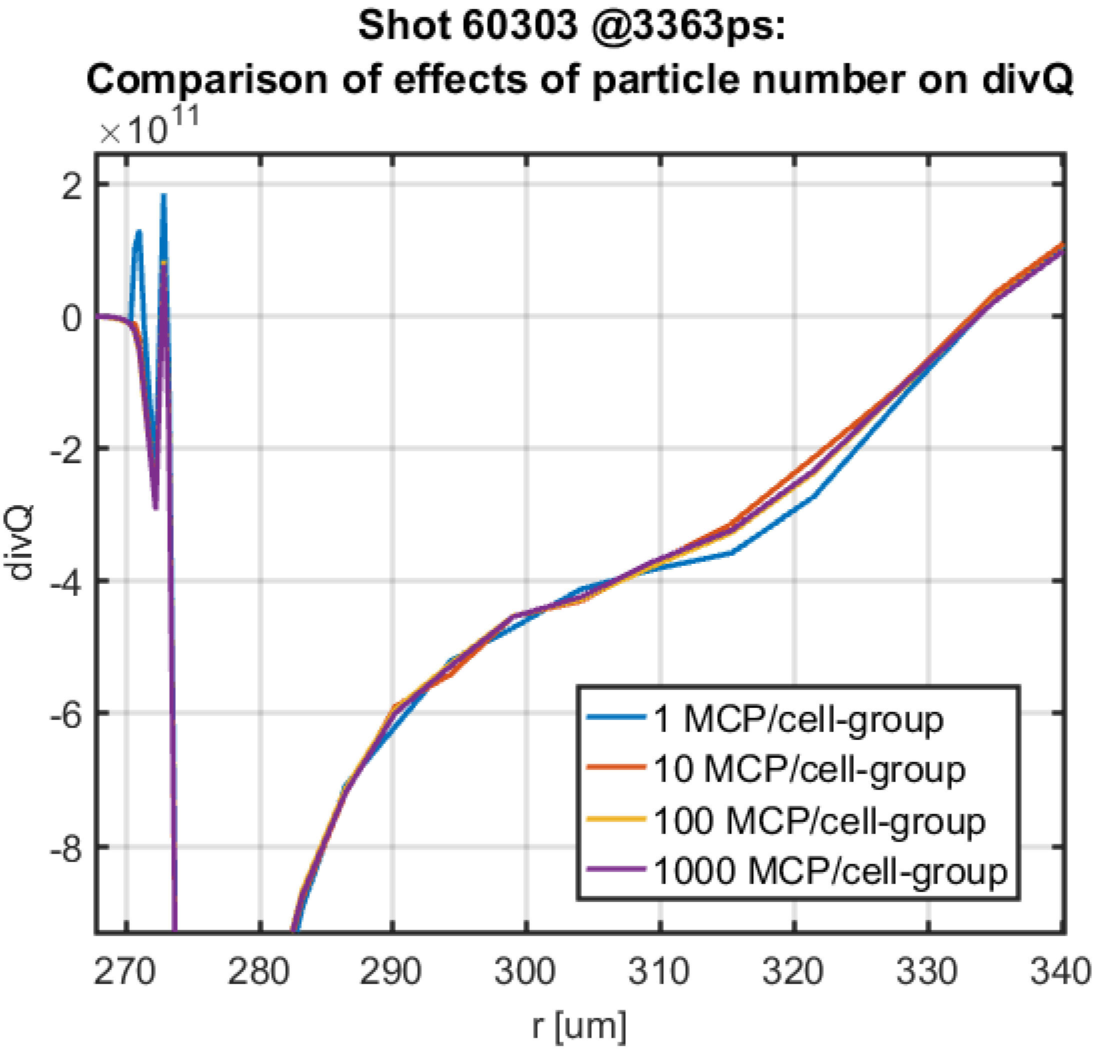

FIGURE 4.4: *Comparison of* $\nabla \cdot \mathbf{Q}$ *for single time step for 1, 10, 100, and 1000 MCPs/cell-group displaying differing statistical variation.*

The 1D Omega shot 60303 simulation was run with three methods in the LLE's 1D LILAC multiphysics code: the iSNB method, Chenhall's new ETTMC transport method and a third 1D method by Valeri Goncharov [20]. The simulations were run on a single core as LILAC is a non-parallelized code. The ETTMC transport model was run with run with 2.5×10^6 MCPs per time step which is an average of about 100 MCP per cell/group. The three models were run to 3.5 ns and the shock front position was extracted from the code as the innermost point where the density had risen to about twice the liquid deuterium density (0.34 g/cm^3). The shock velocity was computed via the numerical derivative of the shock position. The shock velocity was compared between models and against the experimental VISAR measurement (Fig. 4.5). The ETTMC transport and iSNB shock timing curves are the closest together and the Goncharov method most closely matches the experimental model. It should be noted that all three models miss the second shock convergence due to the overprediction of the shock speed after the first shock convergence. This is likely a consequence of the overprediction of laser absorption in the code.

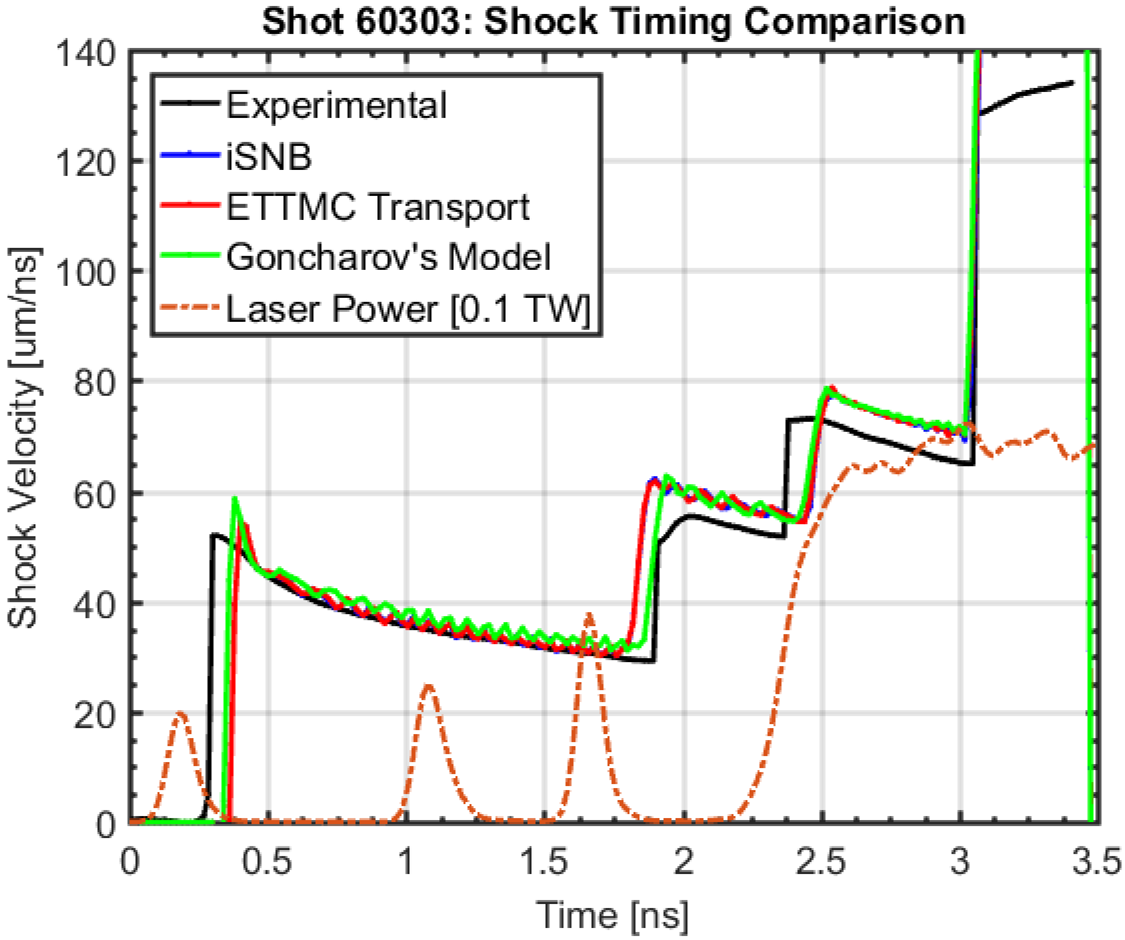

FIGURE 4.5: *Shock timing comparison for iSNB, ETTMC transport, and Goncharov electron thermal transport methods with experimental VISAR data.*

4.1.2 Omega shot 59529: shock timing experiment

Shot 59529 was another experiment preformed on LLE's Omega laser system [18] that used a VISAR to measure the shock velocity (Fig. 4.6). This target consisted of an outer aluminum ablative layer followed by a plastic (CH) shell and an inner deuterium fuel region. The laser consisted of a succession of three laser pickets (Fig. 4.7). Simulation of this shot was done in the 1D LILAC code. The simulation geometry consisted of an outer 50-cell 0.099 μm 2.7 g/cm^3 aluminum ablative layer, a 220-cell 8.91 μm, 1.097 CH shell (43% carbon), a 400-cell 406.5 μm, 0.173 g/cm^3 deuterium fuel layer, and an inner 10-cell 30 μm deuterium gas 4.5×10^{-4} g/cm^3.

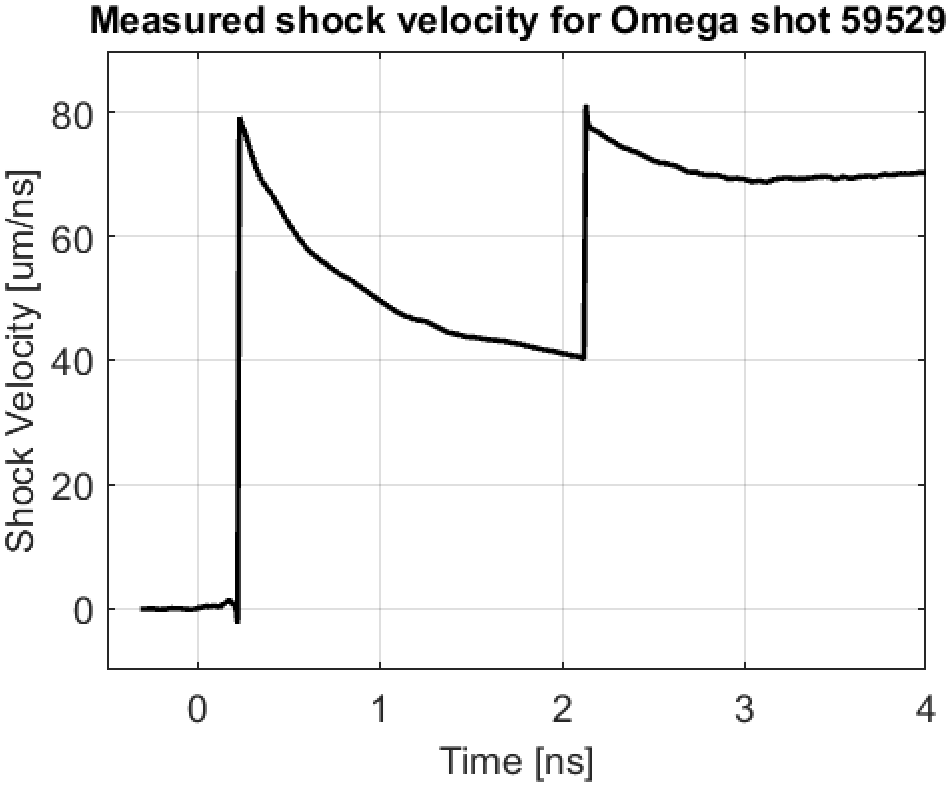

Figure 4.6: *VISAR measured shock velocity for Omega shot 59529.*

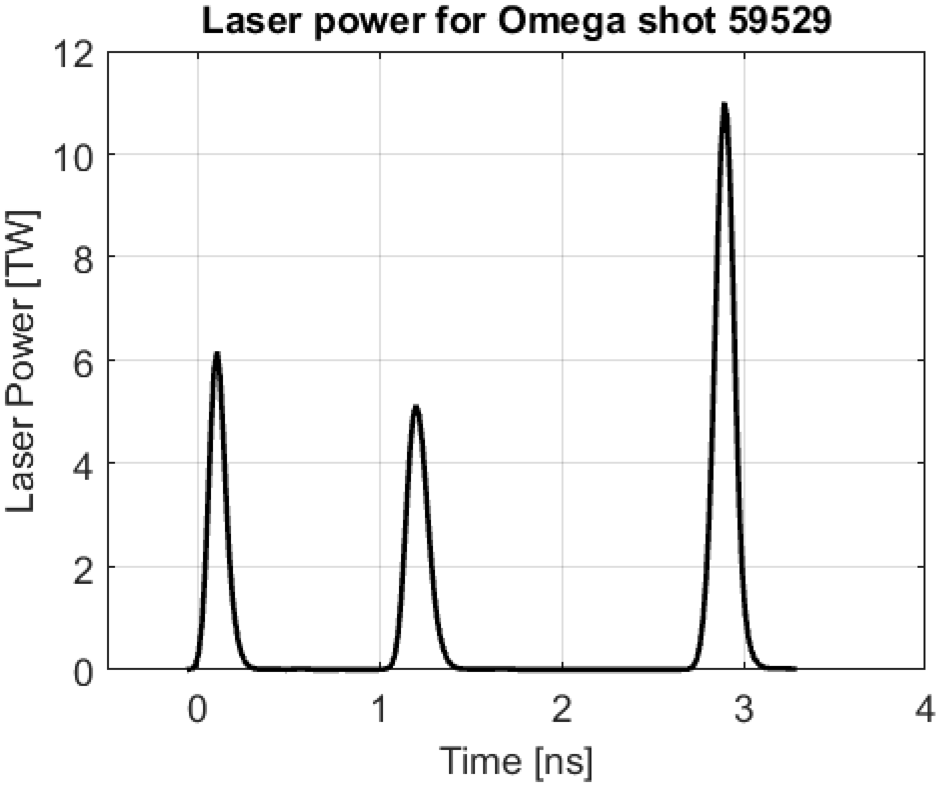

Figure 4.7: *Laser power for Omega shot 59529.*

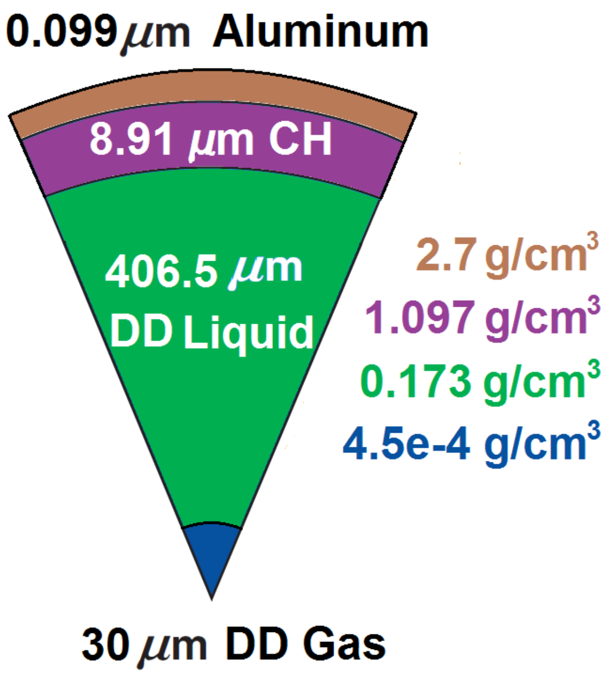

FIGURE 4.8: *Cross section of the target capsule for Omega shot 59529.*

The 1D Omega shot 59529 simulation was run with the non-local iSNB and ETTMC transport models. The non-local models are only turned on in the code after the first picket (before which a flux limiter of 0.06 is used) in order to compensate for inaccuracies in the codes ability to predict the target's cold start-up. In particular, the codes overpredict the laser absorption. Additionally, a flux limiter simulation with a flux limit of 0.06 and an iSNB simulation without the delayed non-local start-up were run. For this simulation the iSNB, ETTMC, and flux limiter methods produced similar results while the iSNB method with no delay over predicted the shock velocity (Fig. 4.9). While the no delay iSNB simulation correctly predicts the shock break out time near 220 ps it overpredicts the shock velocity by about 15%. The other simulations more accurately reproduce the shock velocity but the shock break out time is somewhat delayed. A study of adjusting the flux limiter parameter during the first picket seems to indicate that it is not possible to match both the shock timing and shock velocity near the shock break out at 220 ps. The overprediction of the shock velocity in the no delay simulation means that there is a longer time until the second shock catches up resulting in the 250 ps lag behind the measured shock convergence at 2100 ps. The other methods predict a shock convergence 100 ps too early, which is a result of a too fast of a second shock as seen by the higher predicted shock speed after 2100 ps.

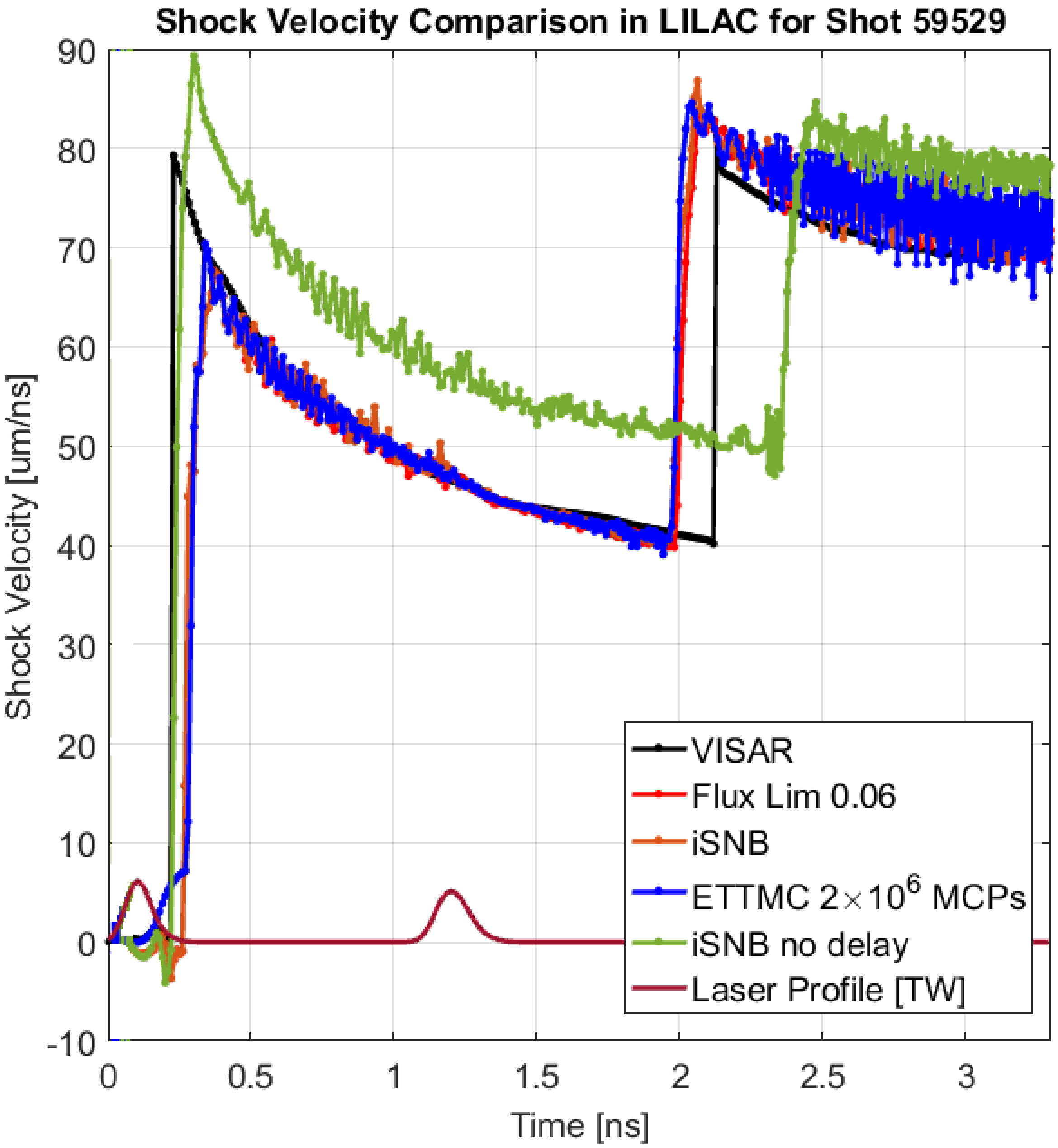

FIGURE 4.9: *Omega shot 59529 shock timing comparison for iSNB, ETTMC transport and flux limiter electron thermal transport methods with experimental VISAR data.*

Another thing of note is that the experimental data indicates a sharper jump in the shock velocity at the first convergence (10 ps vs 90 ps). This issue can be resolved by refinement of the grid used in the simulation. In order to study the effect of spatial convergence in the simulations, 1x, 2x, and 4x grids were compared for the iSNB method. By increasing the grid resolution the simulation was able to better predict the sharp jump in shock velocity at the shock convergence (Fig. 4.10). Furthermore, increasing the grid resolution decreases the noise in the calculated shock timing curve. The reason for these improvements can be seen by looking at the density plot. Fig. 4.11 shows that the 4x grid is able to better produce sharper gradients than the 1x grid, as such the shock position is better defined allowing for better calculation of the shock velocity. It should be noted that while spatial gradients are better resolved, the conditions near the critical density are largely unaffected so laser energy deposition and consequently overall shock velocity magnitude are not greatly affected by grid refinement.

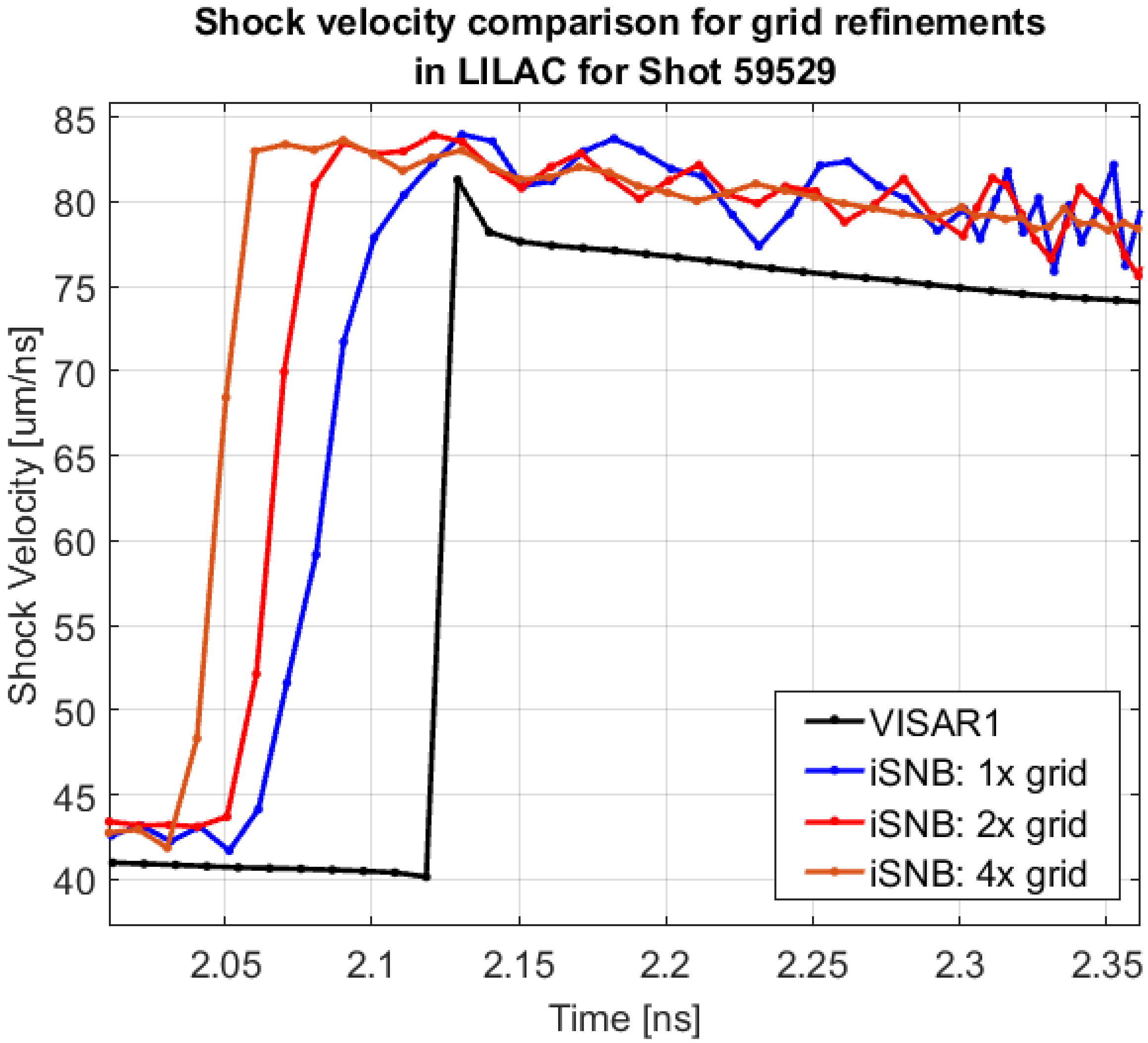

FIGURE 4.10: *Omega shot 59529 shock timing comparison for iSNB simulations with 1x, 2x, and 4x grid refinements and experimental VISAR data.*

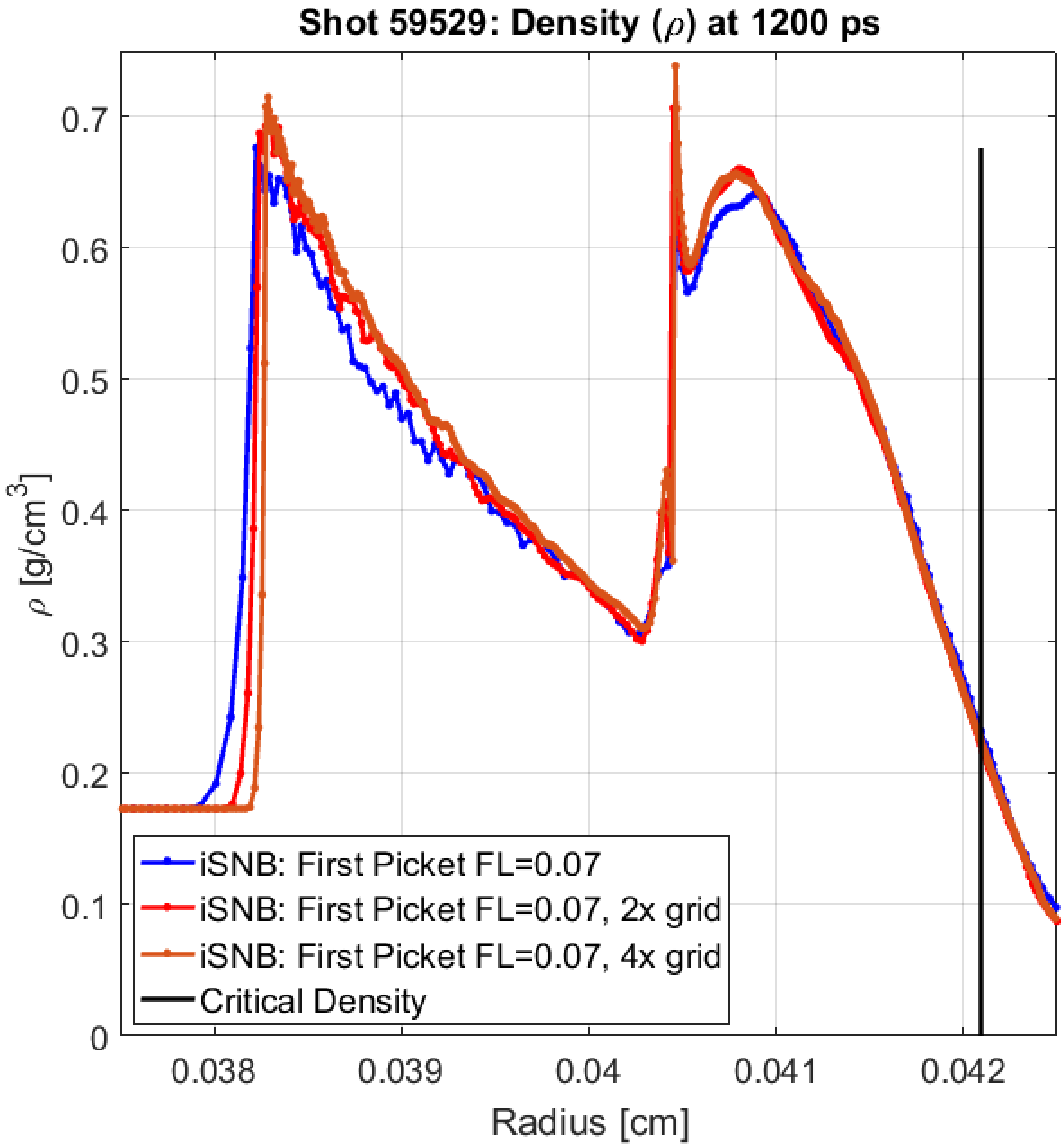

FIGURE 4.11: *Omega shot 59529 density comparison for iSNB simulations with 1x, 2x, and 4x grid refinements.*

4.1.3 Omega shot 68951: cryogenic target implosion experiment

Simulation of Omega shot 68951 was done in LLE's 1D LILAC code [24]. The simulation in 1D spherical geometry consisted of an innermost 379 micron thick 150-cell region of DT gas (41.16% tritium) at 6.8×10^{-4} g/cm^3 density, followed by a middle layer of 47 micron thick 300-cell region of DT ice (43% tritium) at 0.237 g/cm^3 density, and an outermost 8.4 micron thickness layer consisting of 100-cell region of deuterated plastic (40% carbon) at density 1.08 g/cm^3 (Fig. 4.12). The laser profile consisted of three picket laser pulses followed by a main drive for a total laser energy of 26.9 kJ (Fig. 4.13).

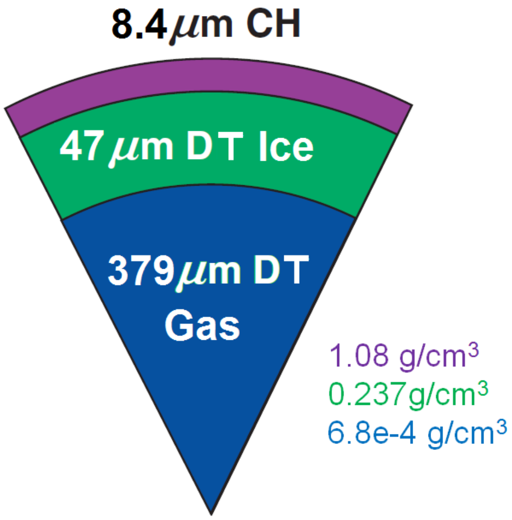

FIGURE 4.12: *Cross section of fuel capsule for Omega shot 68951.*

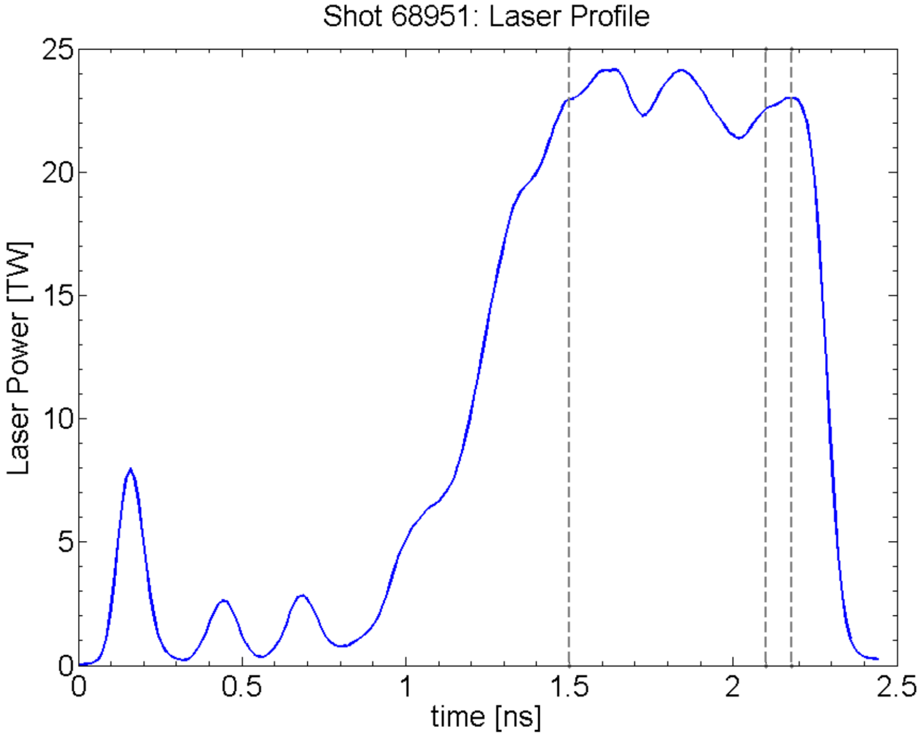

FIGURE 4.13: *Omega shot 68951 laser profile.*

The 1D Omega shot 68951 simulation was run with the ETTMC transport method, the iSNB method, and Goncharov's method. The ETTMC transport model was run using 2×10^5 MCP per time step. The electron temperature and density profiles were compared at a number of time steps. The time steps chosen to display are at 1.5 ns when the laser initially hits full power (Figs. 4.14, 4.15), 2.1 ns near the end of main laser drive (Figs. 4.16, 4.17), and 2.18 ns at the bang time of the implosion (Figs. 4.18, 4.18). For each time step the ETTMC transport solution most resembles the iSNB solution. At 1.5 ns the dense shell in the ETTMC solution is slightly inward of the iSNB result. At 2.1 ns the dense shell in the ETTMC solution is about 10 ps ahead of the iSNB result. This is most likely the result of a slightly lower preheating of the shell in ETTMC allowing for easier compression. The Goncharov solution lags behind the iSNB and ETTMC solutions at both time steps. One possible reason for this is that the Goncharov model uses a leaky outer boundary condition due to numerical constraints whereas iSNB and ETTMC use a reflective condition. The leaky boundary condition in the Goncharov simulation means there is less energy in the problem and thus accounts for the slower inward shell speed. One important figure of merit to ICF implosions is the adiabat (defined as pressure divided by the Fermi pressure), which is a measure of idealness of the target's compression. Often this is quoted as a single number for an implosion, taken to be the minimum value of the adiabat in the high density shell at bang time. The ETTMC transport simulation had an adiabat of 3.798, the iSNB had 3.874, and the Goncharov had 3.941 (Fig. 4.18). Furthermore, shell shape at bang time is nearly identical across all three models (Fig. 4.19) with the small difference likely caused by differing timing (±10 ps).

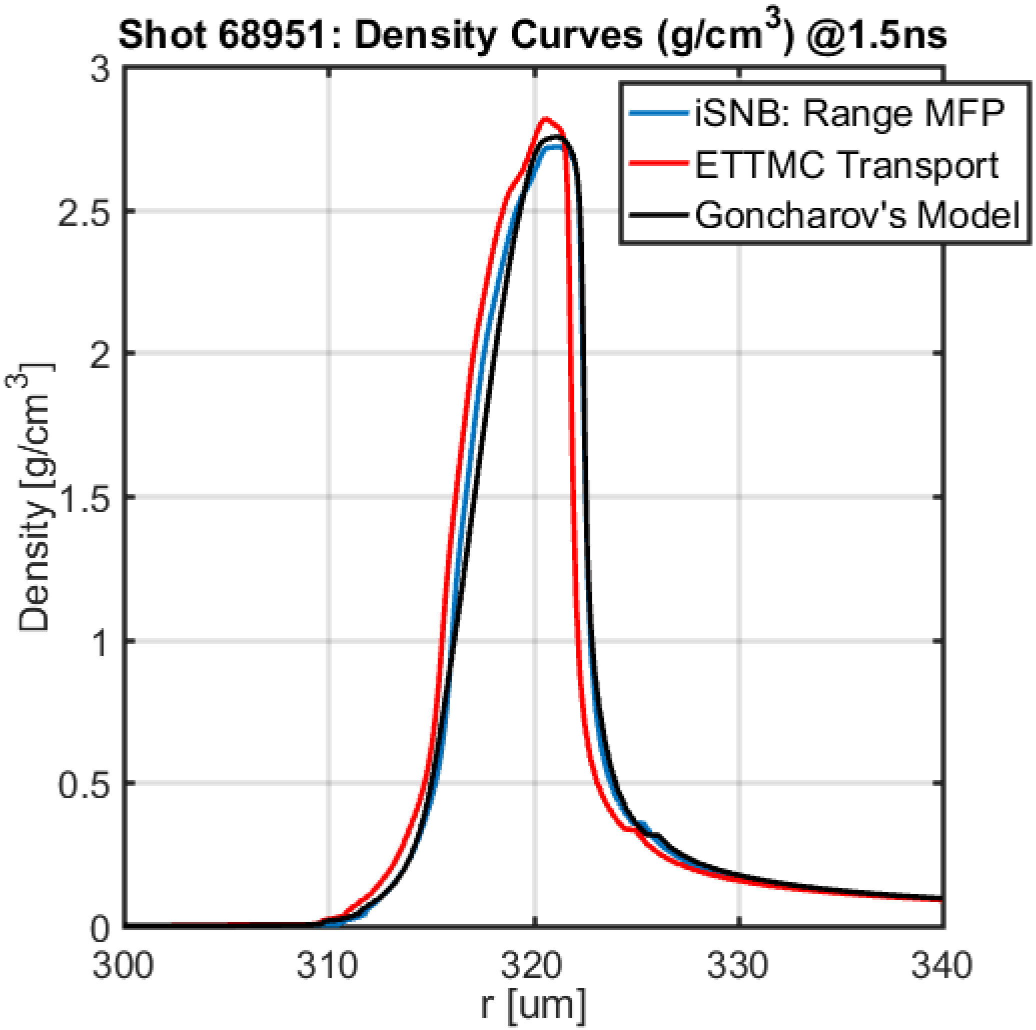

FIGURE 4.14: *Shot 68951 density comparison at 1.5 ns.*

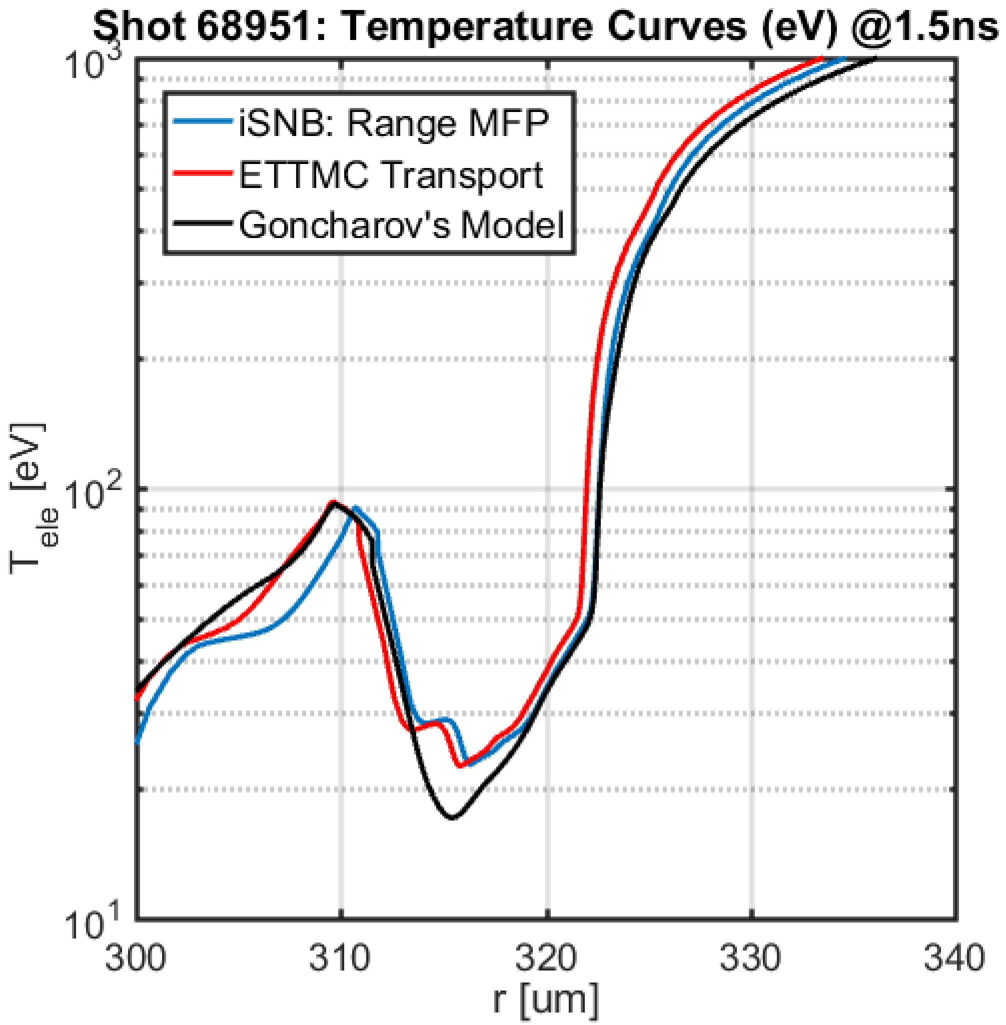

FIGURE 4.15: *Shot 68951 electron temperature comparison at 1.5 ns.*

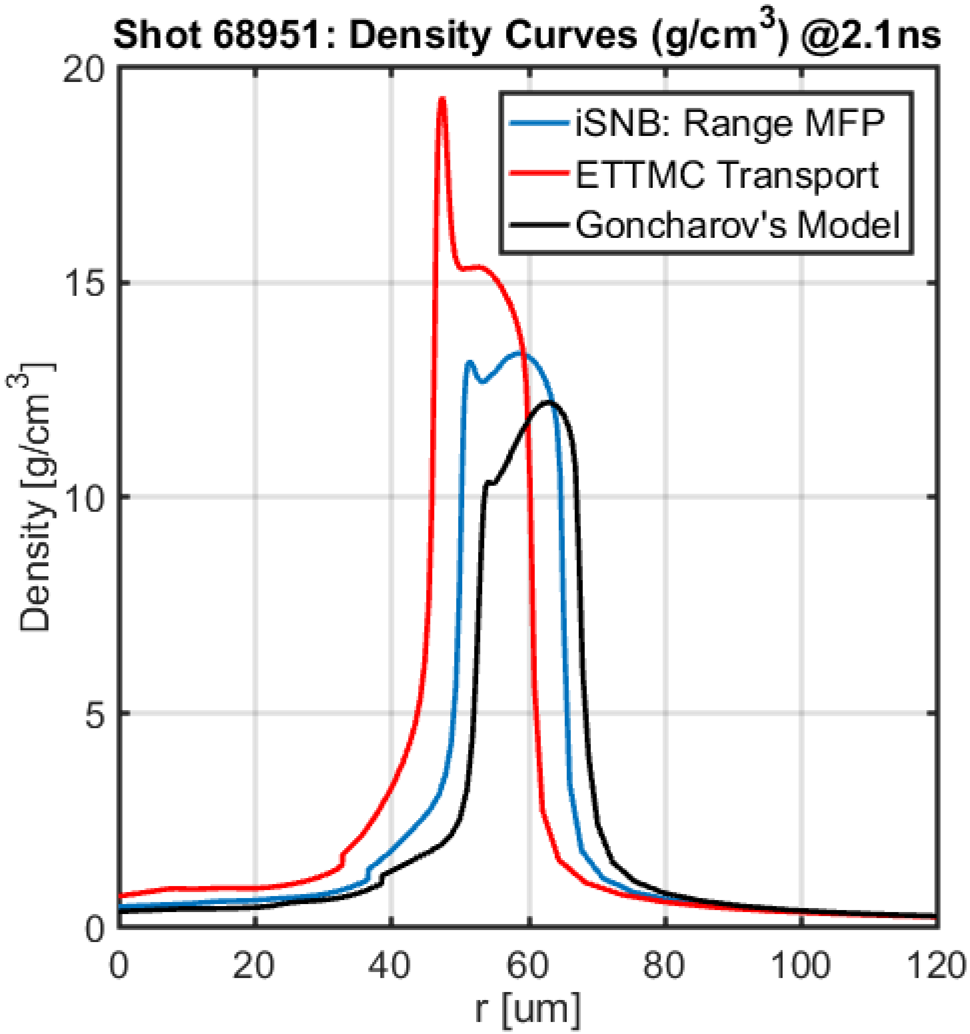

Figure 4.16: *Shot 68951 density comparison at 2.1 ns.*

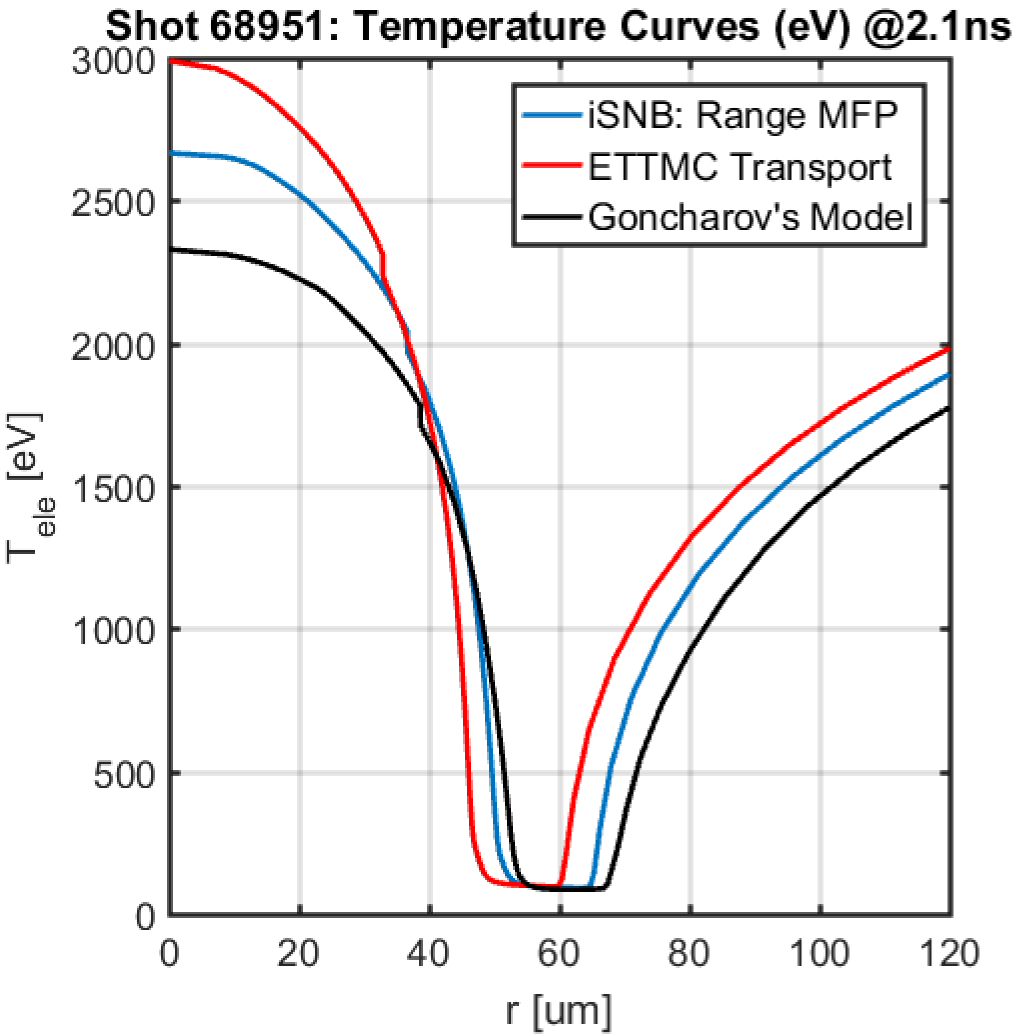

FIGURE 4.17: *Shot 68951 electron temperature comparison at 2.1 ns.*

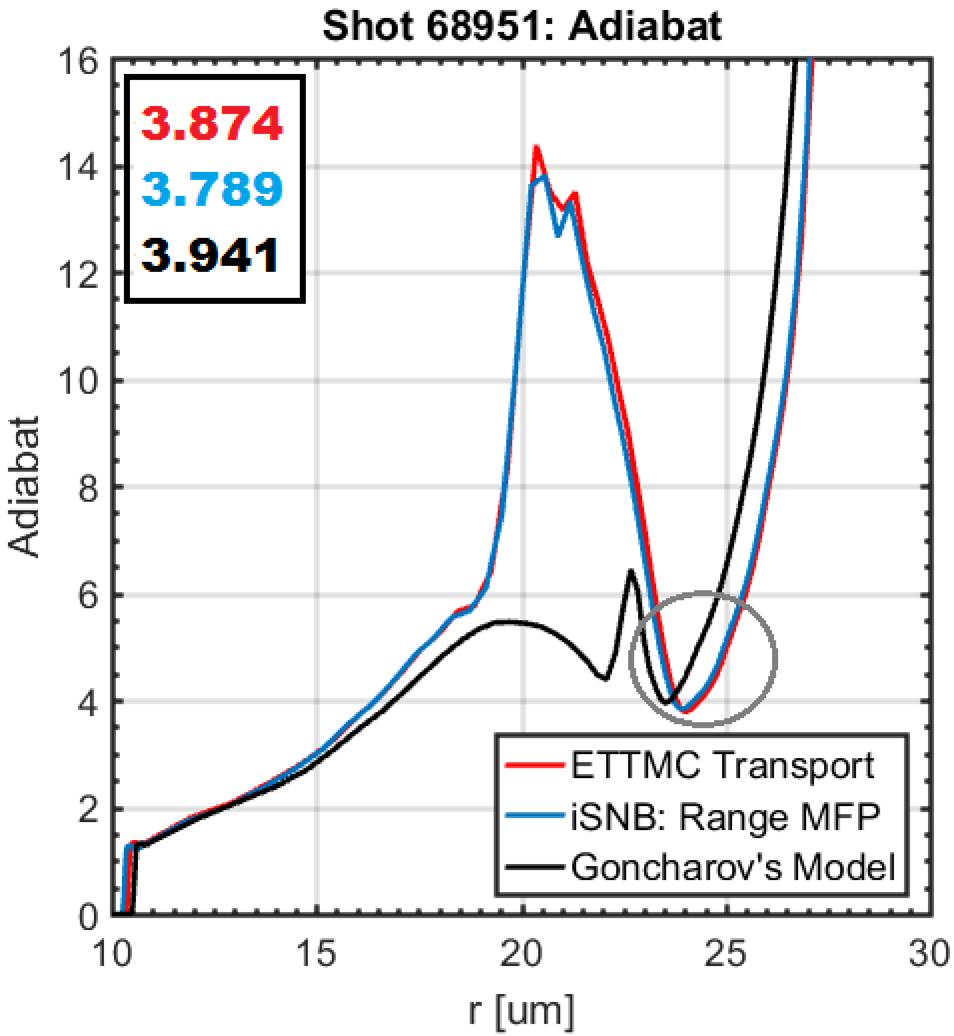

FIGURE 4.18: *Shot 68951 adiabat curves at bang time for ETTMC transport, iSNB, and Goncharov's model.*

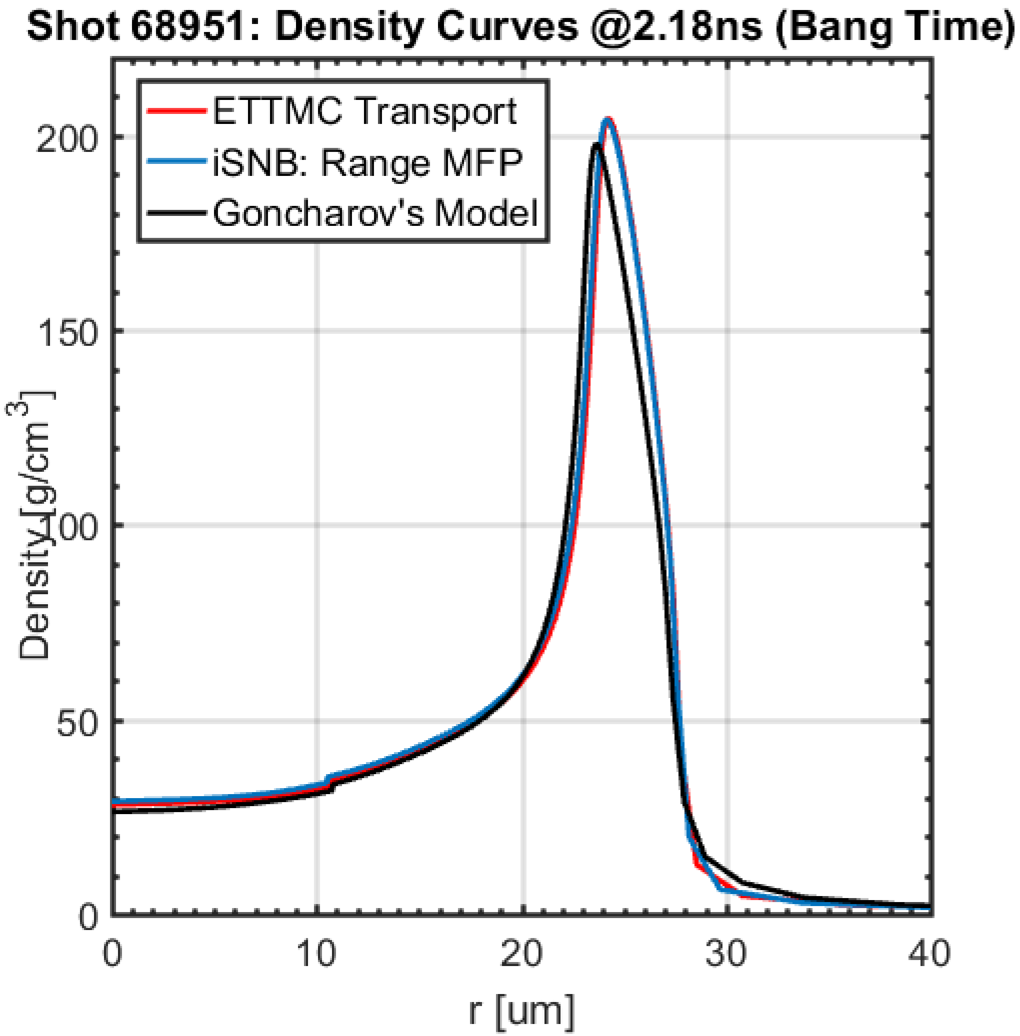

FIGURE 4.19: *Shot 68951 density curves at bang time for ETTMC transport, iSNB, and Goncharov's model.*

4.2 2D Simulations

4.2.1 Omega shot 60303: shock timing experiment

The 2D simulation of shot 60303 consisted of a wedge in RZ coordinates using the same configuration as the 1D simulation in the radial direction and 4.5° 10-cell wedge in the transverse direction with reflective boundary conditions along the edge of the cone. Since the 2D simulation only models a small wedge in the azimuthal direction it can be considered to be a nearly 1D result.

The 2D Omega shot 60303 simulation was run in LLE's 2D DRACO multiphysics code using the iSNB method and the ETTMC method. The ETTMC transport model was run using 2.5×10^7 MCP per time step. As was the case in the 1D LILAC results, the 2D DRACO shock timing results for the ETTMC transport and iSNB methods were quiet similar to each other (Fig. 4.20). Comparing the 1D LILAC solution (Fig. 4.5) to the 2D DRACO solution (Fig. 4.20) it can be seen that both codes produce similar results with the first shock convergence being too early and the second being too late. This agreement is good as it shows that LILAC and DRACO behave similarly for near 1D results.

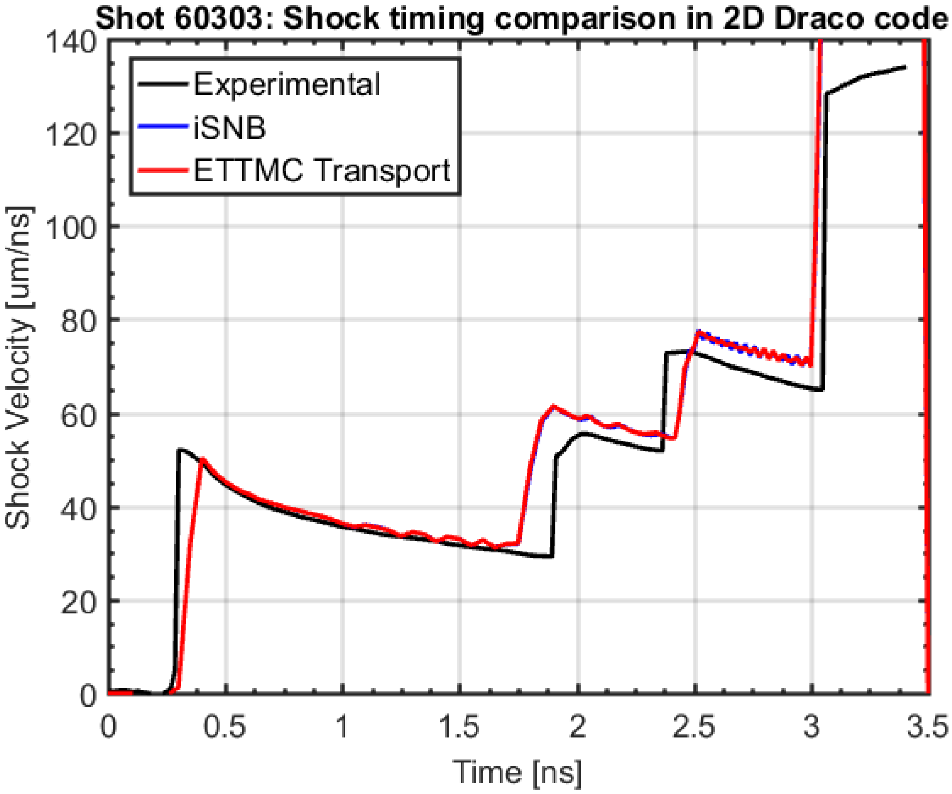

FIGURE 4.20: *Comparison of shock timing in the iSNB and ETTMC transport simulations of shot 60303 to experimental VISAR result.*

4.2.2 NIF polar direct drive (PDD) phase plate design

The polar direct drive (PDD) phase plate target design produced by LLE is an example of a direct drive ICF shot that could be fielded on the NIF laser system [25]. Since NIF is designed to illuminate indirect drive hohlraum targets the beams are positioned towards the poles of the target. As such, if a direct drive target were to be shot on NIF the laser drive would require balancing to account for the non-ideal laser positioning (Fig. 4.21). The laser profile for this simulation consists of two laser pickets followed by a main drive pulse for a total of 700 kJ of laser energy (Fig. 4.23). The laser spot shapes for each ring can be viewed in Fig. 4.22.

Radially the simulation consists of an innermost DD gas region at 15 atm pressure 400 microns in radius consisting of 40 cells; this is followed by a DD gas region at 15 atm pressure, 820 microns thick consisting of 87 cells; this is followed by a plastic (CH) solid ablation layer at 1.03 g/cm^3 density 79.85 microns thick consisting of 130 cells; and an outermost CH ablation layer at 1.03 g/cm^3 density, 0.15 microns thick consisting of 2 cells (Fig. 4.24). In the transverse direction the simulation consists of 90 equally spaced cells.

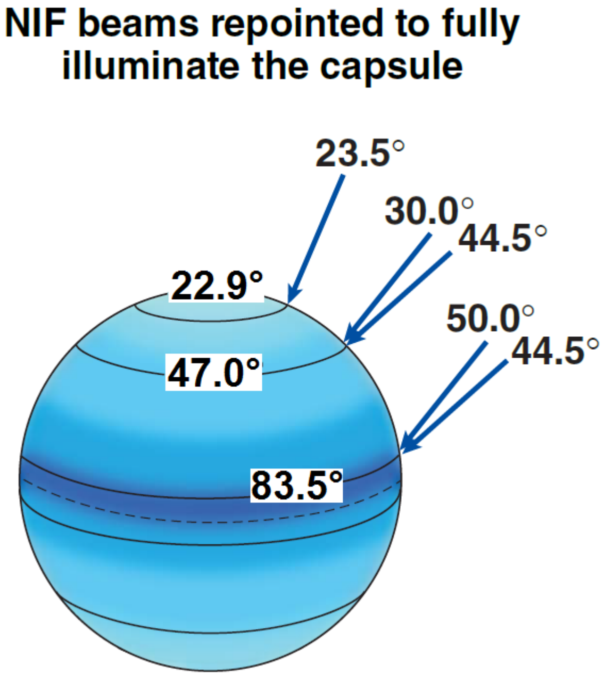

Figure 4.21: *Laser pointing scheme optimized for NIF phase plate PDD design [Figure obtained from Collins 2012 [26]].*

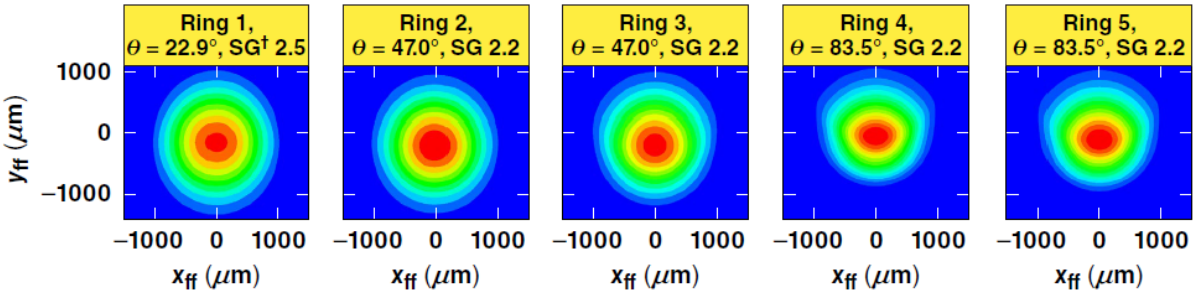

FIGURE 4.22: *Laser spot shapes for NIF phase plate PDD design [Figure obtained from Cao 2015 [25]]*

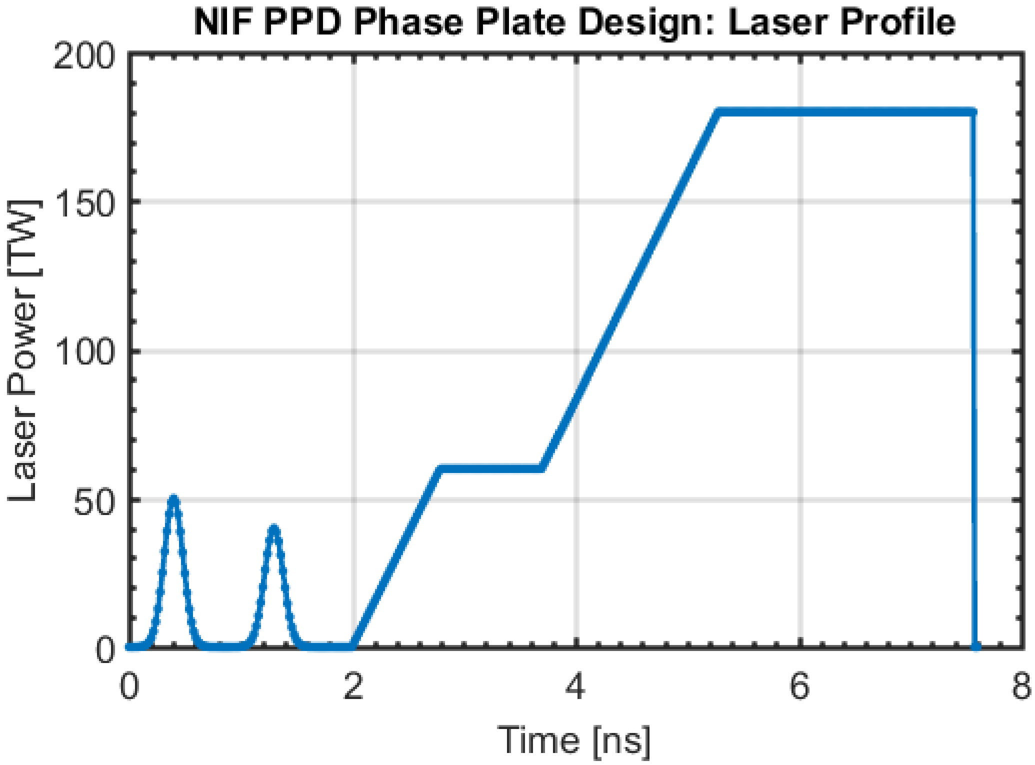

FIGURE 4.23: *NIF PDD phase plate laser profile consisting of two pickets and a ramp up to full power.*

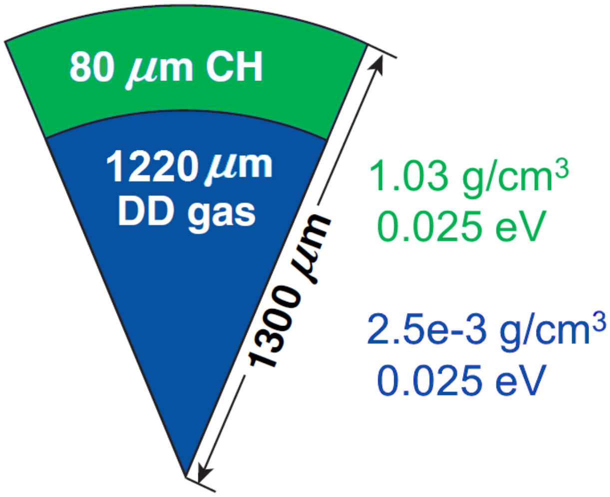

FIGURE 4.24: *Cross section of target capsule for NIF PDD phase plate design.*

The phase plate simulation was run in LLE's 2D DRACO code using the iSNB method and the ETTMC transport method. The ETTMC transport model was run using 1.2×10^7 MCP per time step. Both the iSNB and ETTMC simulations were run to 7.6 ns which is the end of the main laser drive. The electron temperature and density profiles, taken along the r-axis for ease of comparison, are compared for each model at 7.45 ns (Figs. 4.25 and 4.26). At 7.45 ns the iSNB and ETTMC results are nearly identical except for a slight temperature difference in the corona and near the inner shock front. At the inner temperature front near 120 μm (Fig. 4.26) the ETTMC solution is slightly inward of the iSNB solution. Furthermore, we note that the iSNB temperature has a longer exponential-like tail into the cold material ahead of the front. The ETTMC solution has a sharper temperature drop off. The reason for this difference is likely due to how the models handle particle deposition. Diffusion equations, such as those used in the iSNB method, have characteristically exponential solutions ($\sim \exp(-x/\lambda)$). Consequently, at 1 MFP or range the particle will not be completely depleted (1/e will remain) and energy will be further transported thus contributing to preheating. This increase of preheating will allow the cold material ahead of the front to push back retarding the motion of the front. On the other hand, the ETTMC model is able to treat charged particle deposition correctly and stops particles at their range resulting in lower preheating and thus less resistance to compression. The effect of preheating is consistent with Fig. 4.26 in that the higher preheating iSNB solution is delayed in comparison to the ETTMC solution. Of further note, the preheated temperatures ahead of the temperature front are of order 10 eV, which is close to the hydrogen ionization energy. Consequently the preheating can have a significant effect on the material state out ahead of the shock front.

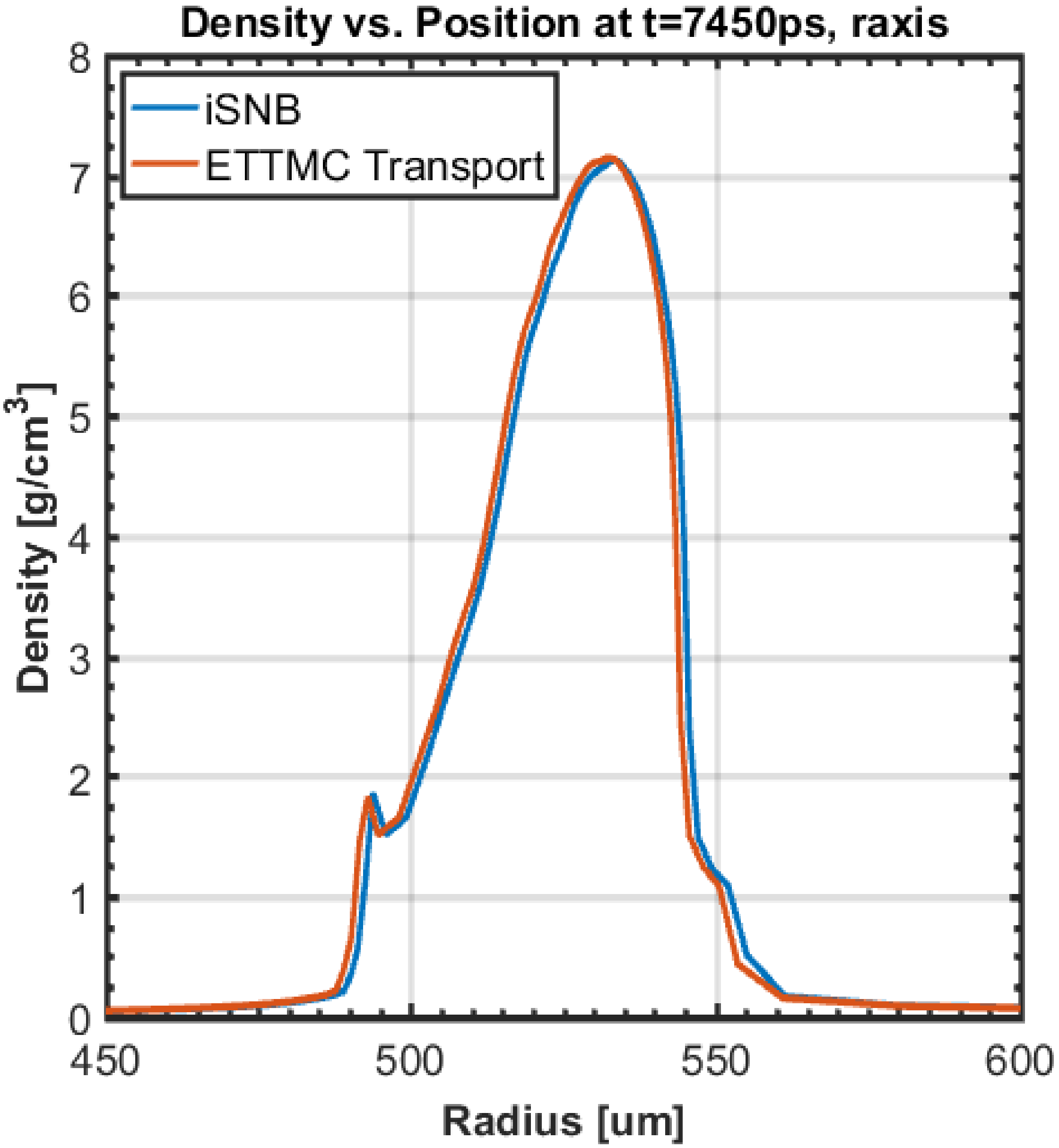

Figure 4.25: *Density profile comparison for the NIF PDD phase plate simulation for iSNB and ETTMC transport methods at 7450 ps.*

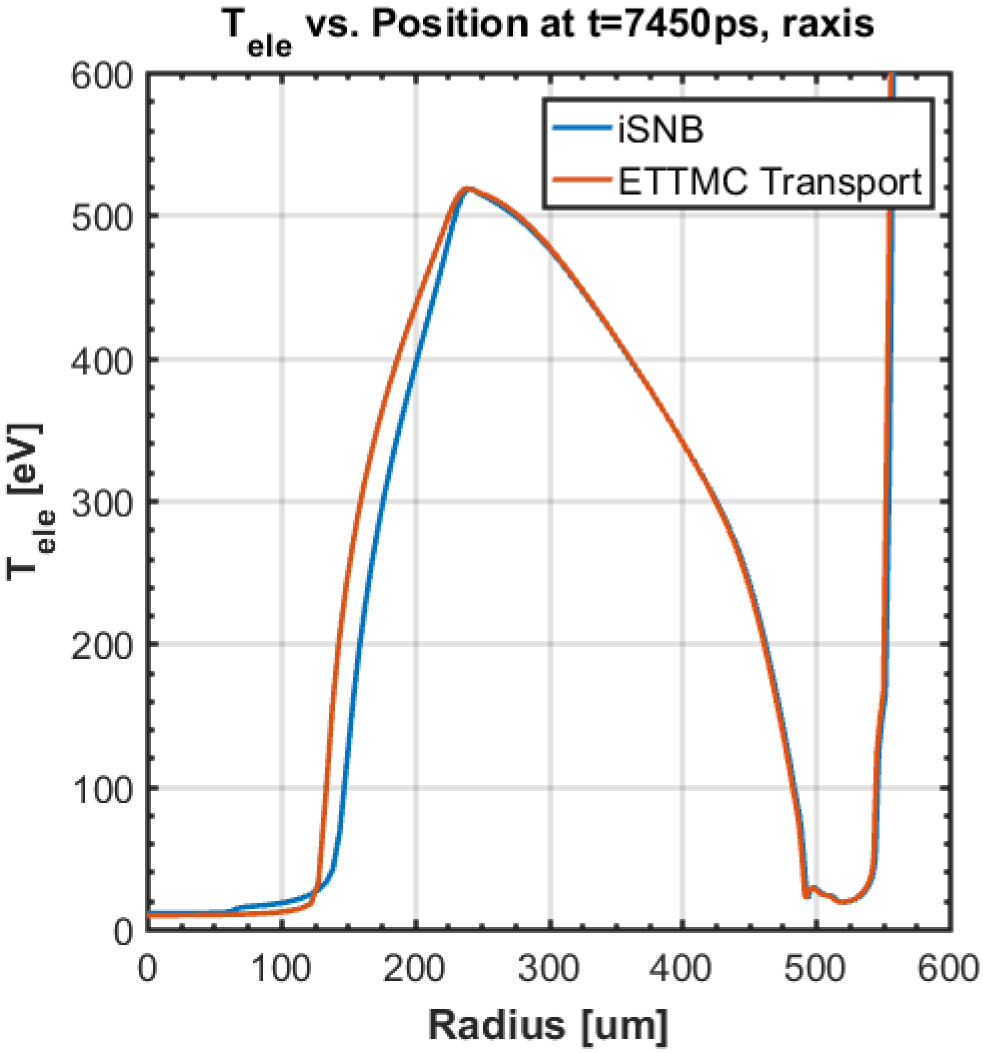

FIGURE 4.26: *Electron temperature profiles for iSNB and ETTMC transport simulations at 7450 ps showing a decrease in preheating in the ETTMC method at the inner shock front at 120 μm.*

4.2.3 NIF PDD phase plate design with drive asymmetry

In order to get a better understand the difference between iSNB and ETTMC a non-ideal symmetry problem was tried. This simulation is a modified version of the NIF PDD phase plate design with the difference that laser rings 2 and 3 have their power increased by 10% and rings 4 and 5 have their power decreased by 10% resulting in a more ’pancaked’ implosion.

Once again the iSNB and ETTMC simulations produce similar results. Looking at the density at the end of the laser pulse at 7600 ps we see that asymmetric laser drive does produce a slightly pancaked implosion (Fig. 4.27). In order to better compare the differences in the dense shell, the shell thicknesses at full width half maximum (FWHM) for the iSNB and ETTMC simulations have been plotted in Fig. 4.28. The iSNB model predicts a slightly higher shell thickness than the ETTMC model. This is likely due to the exponential nature of the iSNB diffusion solution depositing additional preheat energy in the dense shell, increasing its temperature and causing it to expand slightly. Looking at the electron temperature prior to the inner shock waves reaching the origin at 7450 ps (Fig. 4.29) we see similar preheating behavior to that seen in our discussion in the previous section. Again the iSNB solution produces an exponential tail into the cold material ahead of the front while the ETTMC solution produces a sharper cutoff. Furthermore, due to the lower preheating the ETTMC temperature front is further advanced than the iSNB front.

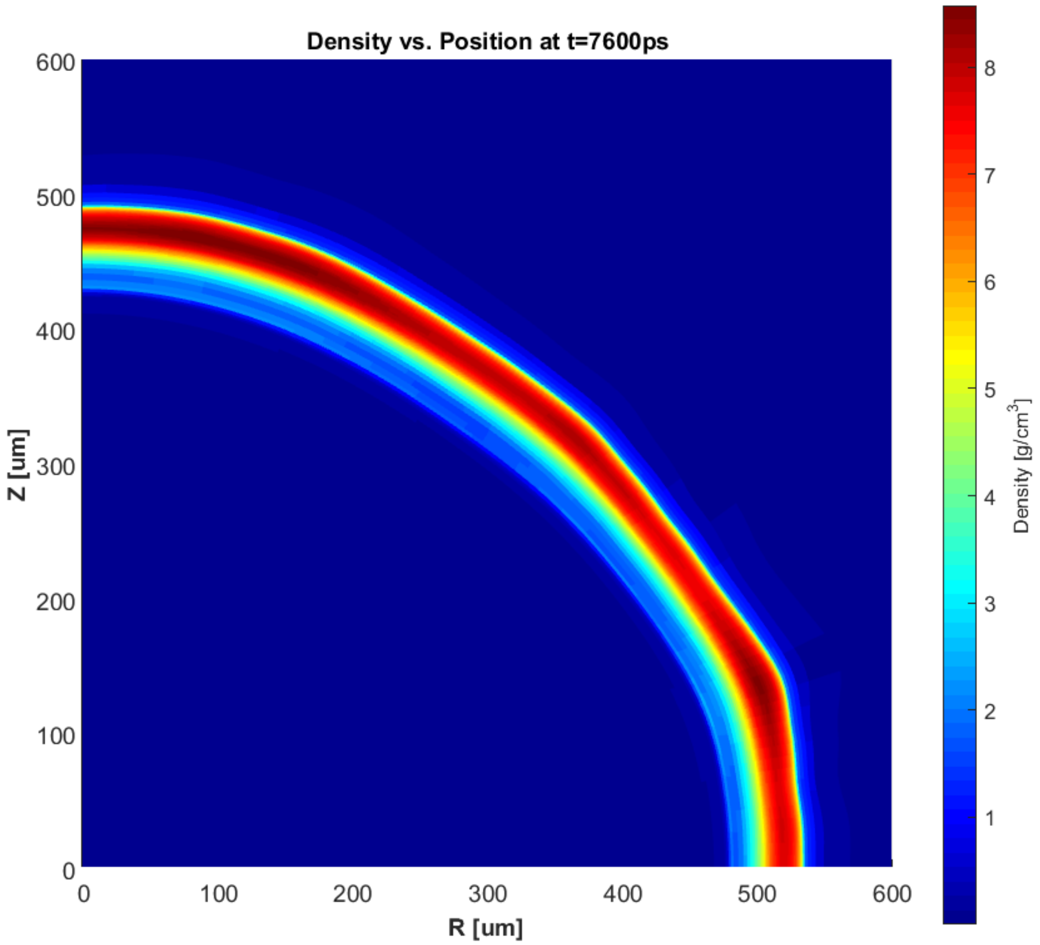

Figure 4.27: *Density distribution at 7600 ps for the NIF PDD phase plate asymmetry problem.*

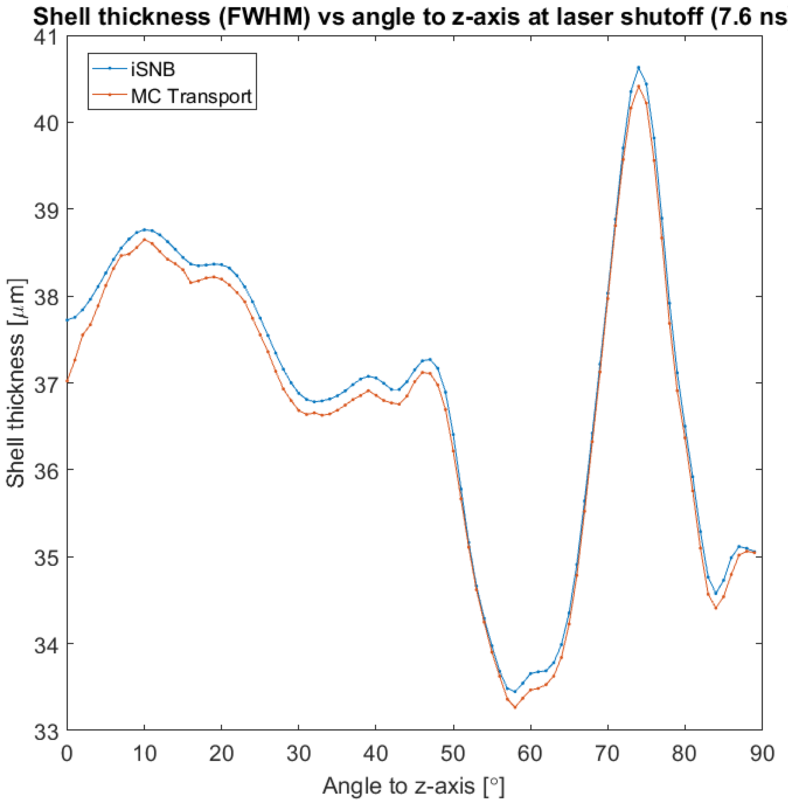

Figure 4.28: *Shell thickness comparison for iSNB and ETTMC at 7600 ps for the NIF PPD phase plate asymmetry problem.*

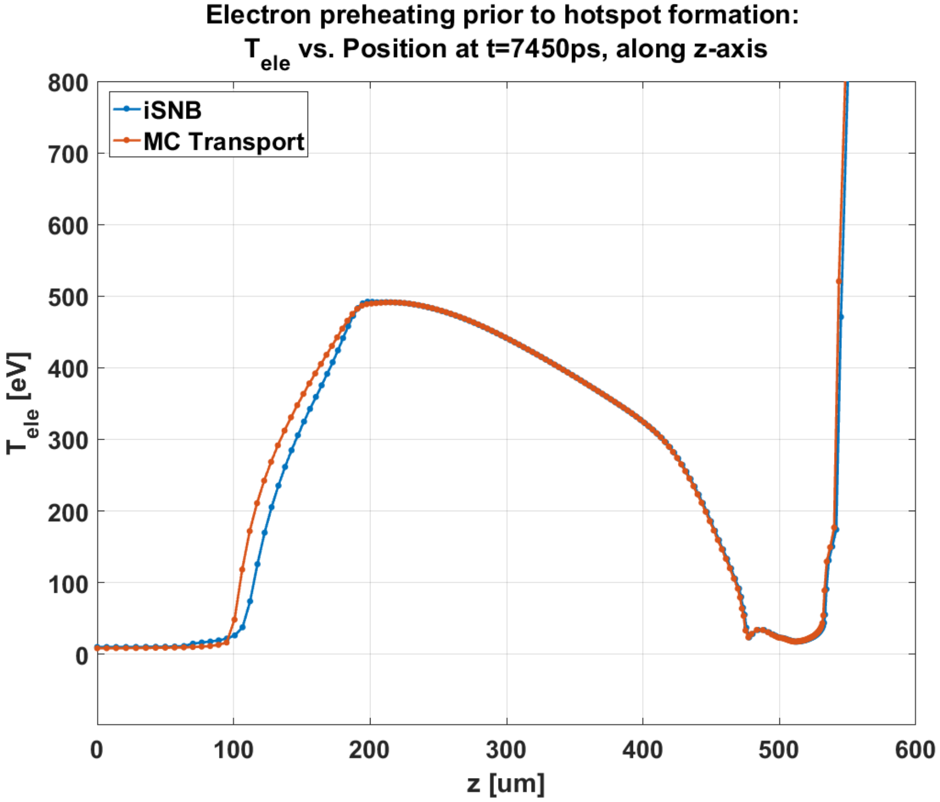

FIGURE 4.29: *Electron temperature distribution comparison iSNB and ETTMC models at 7.45 ns along the z-axis for the NIF PDD phase plate asymmetry problem.*

4.2.4 Hybrid Modeling in DRACO

In order to characterize the hybrid method the shot 60303 simulation was run with cell widths of 0.1, 1.0 and 10 MFPs as the minimum optical depth for diffusion to occur. Over the run time of the simulation the fraction of the source term (in magnitude) was computed in order to see how the importance of transport behavior varied over time. Fig. 4.30 shows a comparison of the transport fraction for 0.1, 1.0, and 10 MFP cutoffs. As expected higher proportion of the calculation is devoted to transport as the minimum optical depth for diffusion increases. Furthermore, the fraction of the source devoted to transport increases at the beginning of each of the laser pulses. This is likely due to the energy deposition raising the temperature and consequently average MFP at a faster rate than the grid expands. After the peak of the laser pulse the fraction devoted to transport tends to taper off likely due to the hydrodynamics allowing for expansion of the grid and consequently a decrease in the average optical depth of the cells.

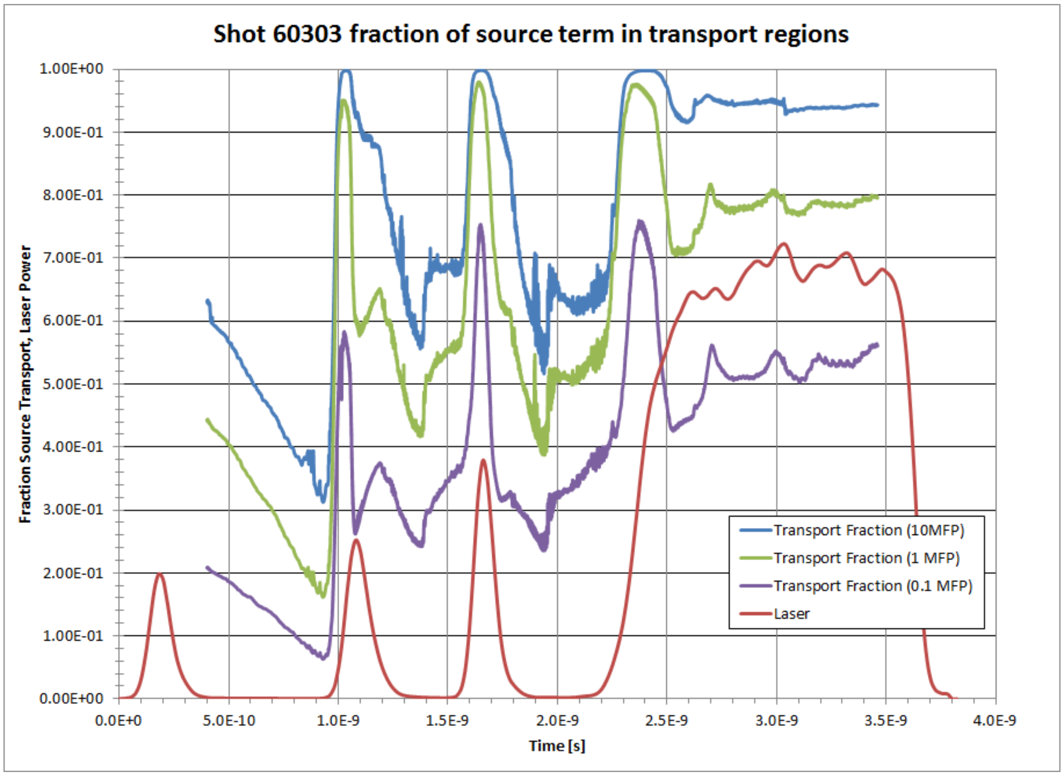

Figure 4.30: *The fraction of the source term in transport regions for cutoffs of 0.1, 1.0, and 10 MFPs for the 60303 hybrid diffusion-transport simulation.*

Next we look at specific differences between the hybrid model's effects. For this investigation the NIF phase plate asymmetry problem was used as it has higher energy which allows for greater difference between the iSNB and transport models. Of particular interest is the differences in energy dependence of $\nabla \cdot \mathbf{Q}$ between the models. The phase plate asymmetry problem was run using the hybrid model with a diffusion cutoff of 10 MFPs and 1.2×10^7 MCPs per time step up to 6000 ps (a point at which the laser has reached full power) in order to provide a developed initial condition for model comparison. At 6000ps, the simulation was run for a single time step with models iSNB, ETTMC, and Hybrid with diffusion cutoffs of 1, 3, and 10 MFPs. The ETTMC models used 1.2×10^9 MCP (a cost prohibitive number of particles for an integrated calculation, but useful for getting better statistics for a single time step). The heat flux divergence energy distributions were compared at three points: near the outer edge of the shell, at 955 μm, and at the critical density marked by vertical dashed lines in Figs. 4.31 and 4.32.

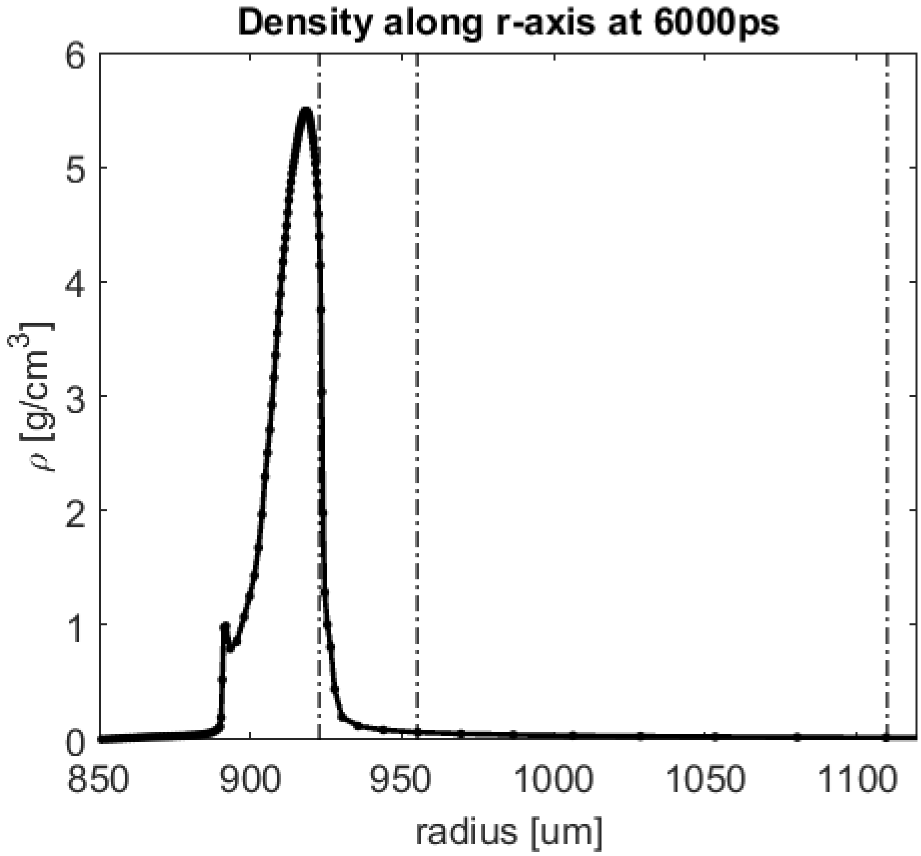

FIGURE 4.31: *Density along the r-axis of the phase plate asymmetry simulation at 6000ps with marked points of interest (dash dot lines) for hybrid* $\nabla \cdot \mathbf{Q}$ *comparison.*

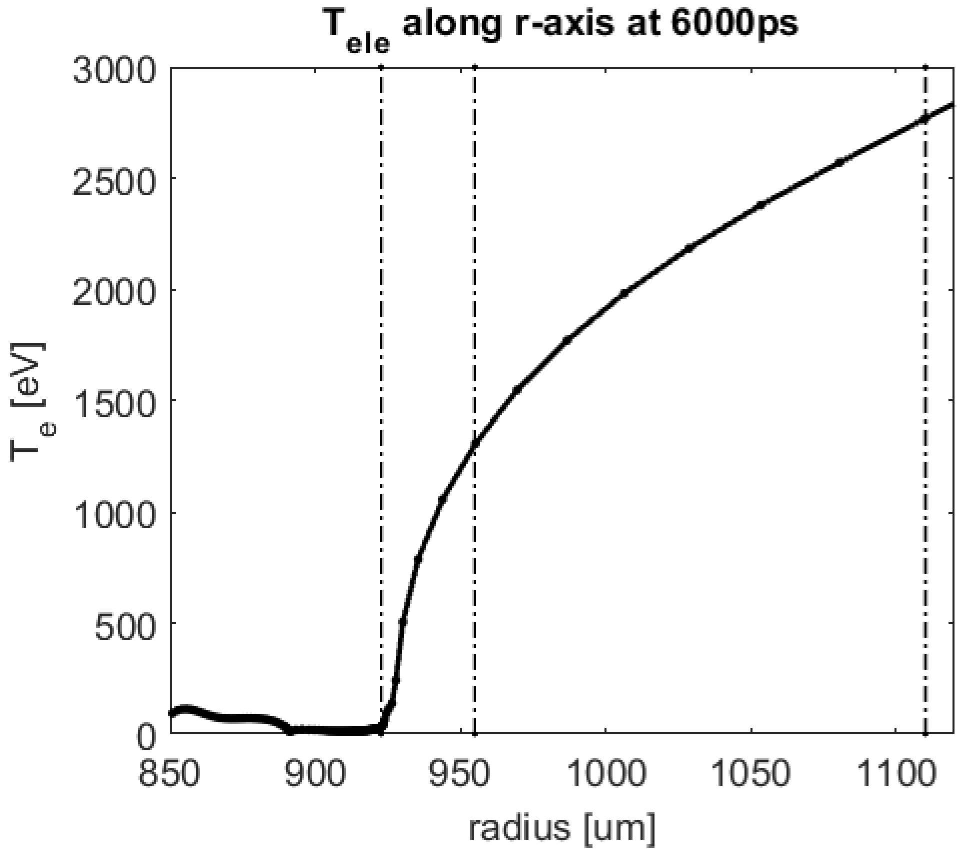

Figure 4.32: *Electron temperature along the r-axis of the phase plate asymmetry simulation at 6000ps with marked points of interest (dash dot lines)for hybrid $\nabla \cdot \mathbf{Q}$ comparison.*

Looking at the total $\nabla \cdot \mathbf{Q}$ (Fig. 4.33) the iSNB diffusion method's $\nabla \cdot \mathbf{Q}$ differs from the hybrid and transport method by around 5% for much of the range between the critical density and peak $\nabla \cdot \mathbf{Q}$.

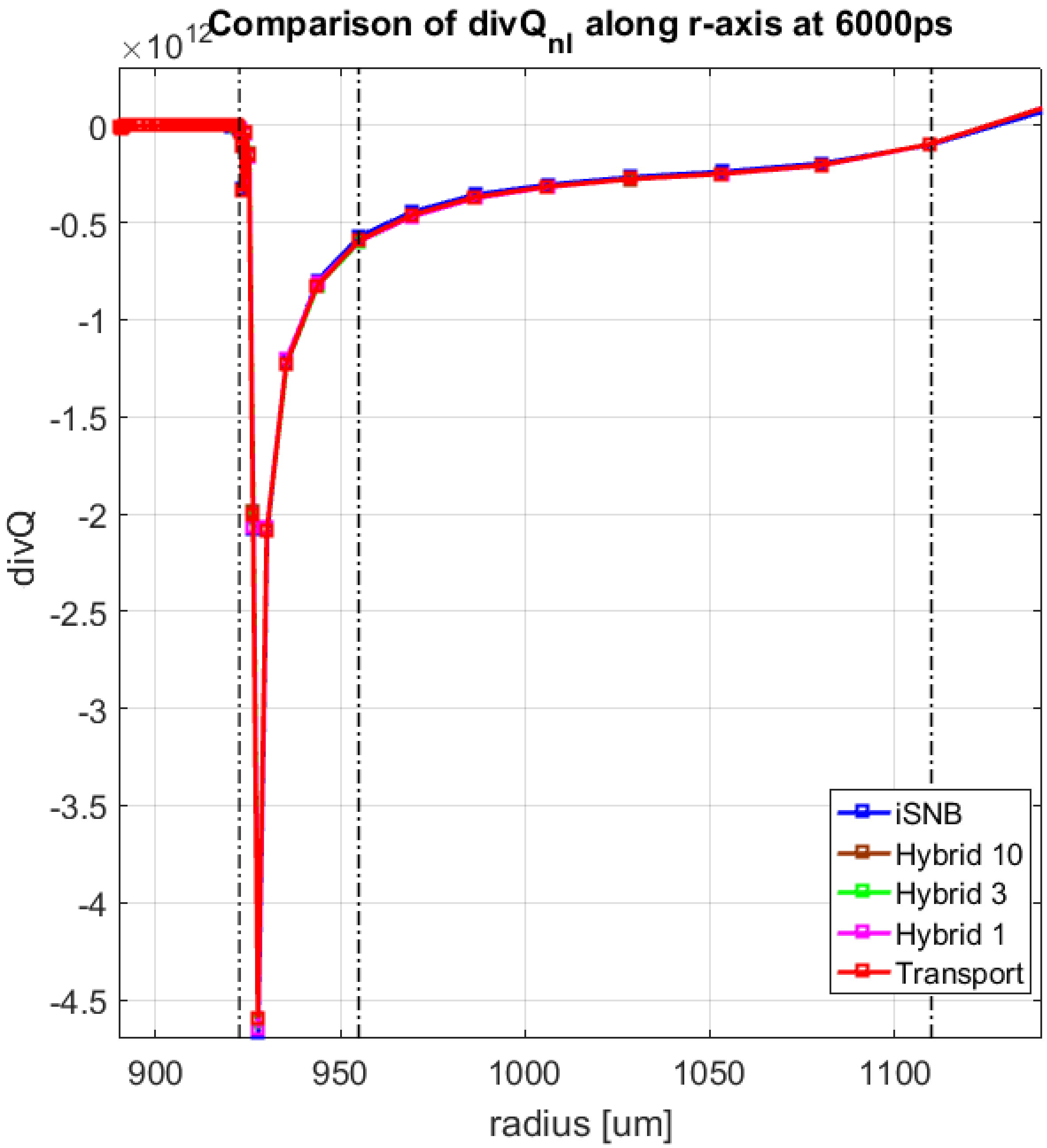

FIGURE 4.33: $\nabla \cdot \mathbf{Q}$ *along the r-axis of the phase plate asymmetry simulation at 6000ps with marked points of interest (dash dot lines) for hybrid* $\nabla \cdot \mathbf{Q}$ *comparison.*

The energy distribution of $\nabla \cdot \mathbf{Q}$ at 955 μm is plotted in Fig. 4.34 for the iSNB, ETTMC pure transport, and hybrid methods. Below around 6.5 keV all models produce nearly identical distributions. Above this energy the hybrid and pure transport solutions diverge from the iSNB result differing by up to 25% in the highest energy group. Of particular interest is the choice of minimum cell optical depth for diffusion to occur. Ideally we want to use the minimum possible optical depth as our cutoff for diffusion as it allows for the most particles to be devoted to a truly transport-like regime thus improving statistics (or alternatively allowing the total number of particles to be reduced thus reducing simulation run time). Zooming in on the distribution in Fig. 4.35, the hybrid 1 distribution has an abrupt transition near 7.5 keV between the higher energy transport solution and the lower energy iSNB diffusion solution. This is in contrast to the hybrid 3 and 10 distributions which remain nearly identical to the transport solution, which smoothly approaches the iSNB diffusion solution at lower energy (In fact, the hybrid 3 and 10 solution have their own transitions at lower energies but at those energies the transport and diffusion solutions are nearly identical and the transitions are tolerable). The abruptness of the jump in the hybrid 1 solution indicates that a choice of 1 MFP optical depth is too thin for the diffusion solution to be correct.

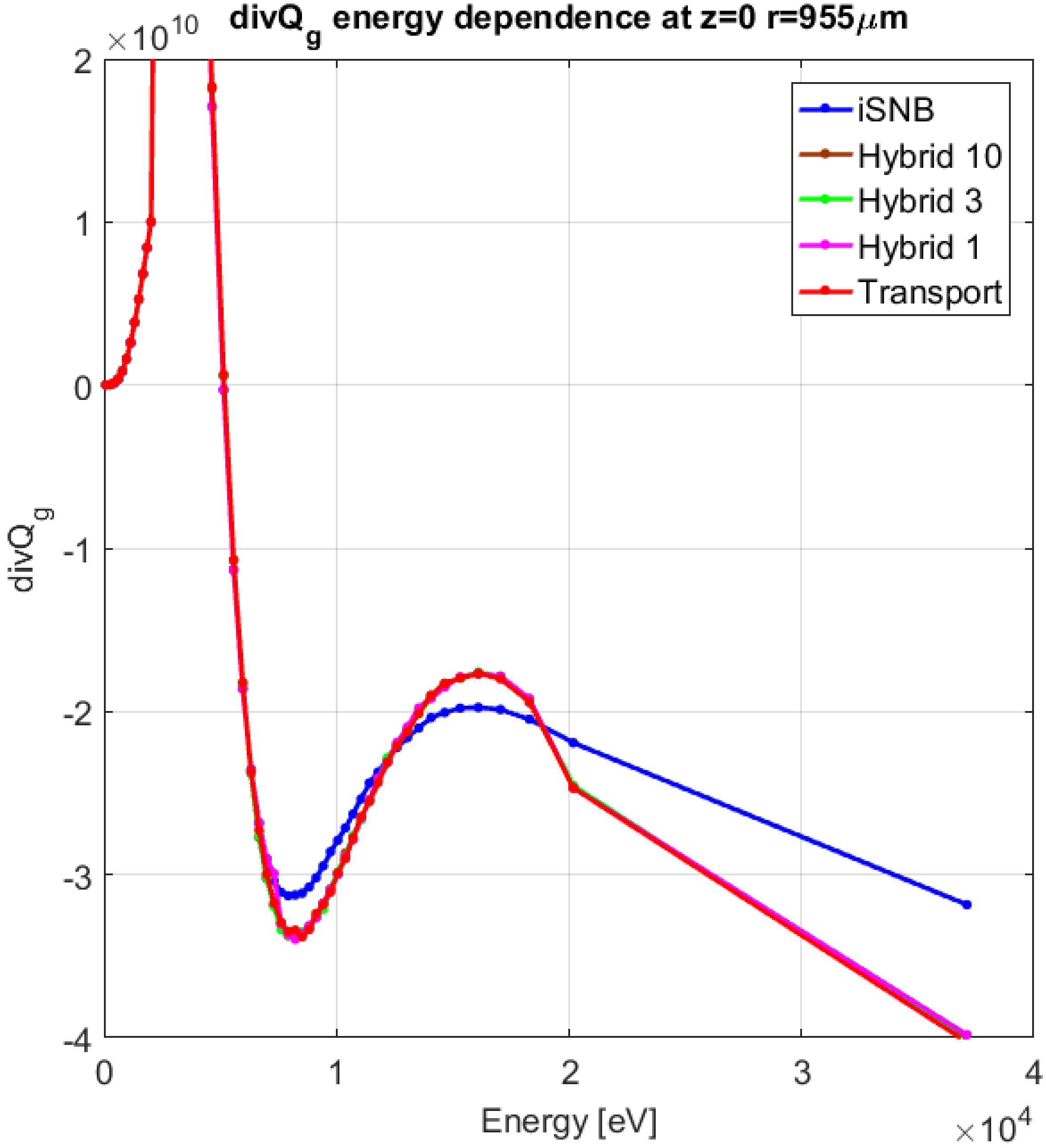

FIGURE 4.34: *Energy dependence of* $\nabla \cdot \mathbf{Q}$ *comparison for iSNB, pure transport and hybrid model with cutoffs of 1, 3, and 10 MFPs.*

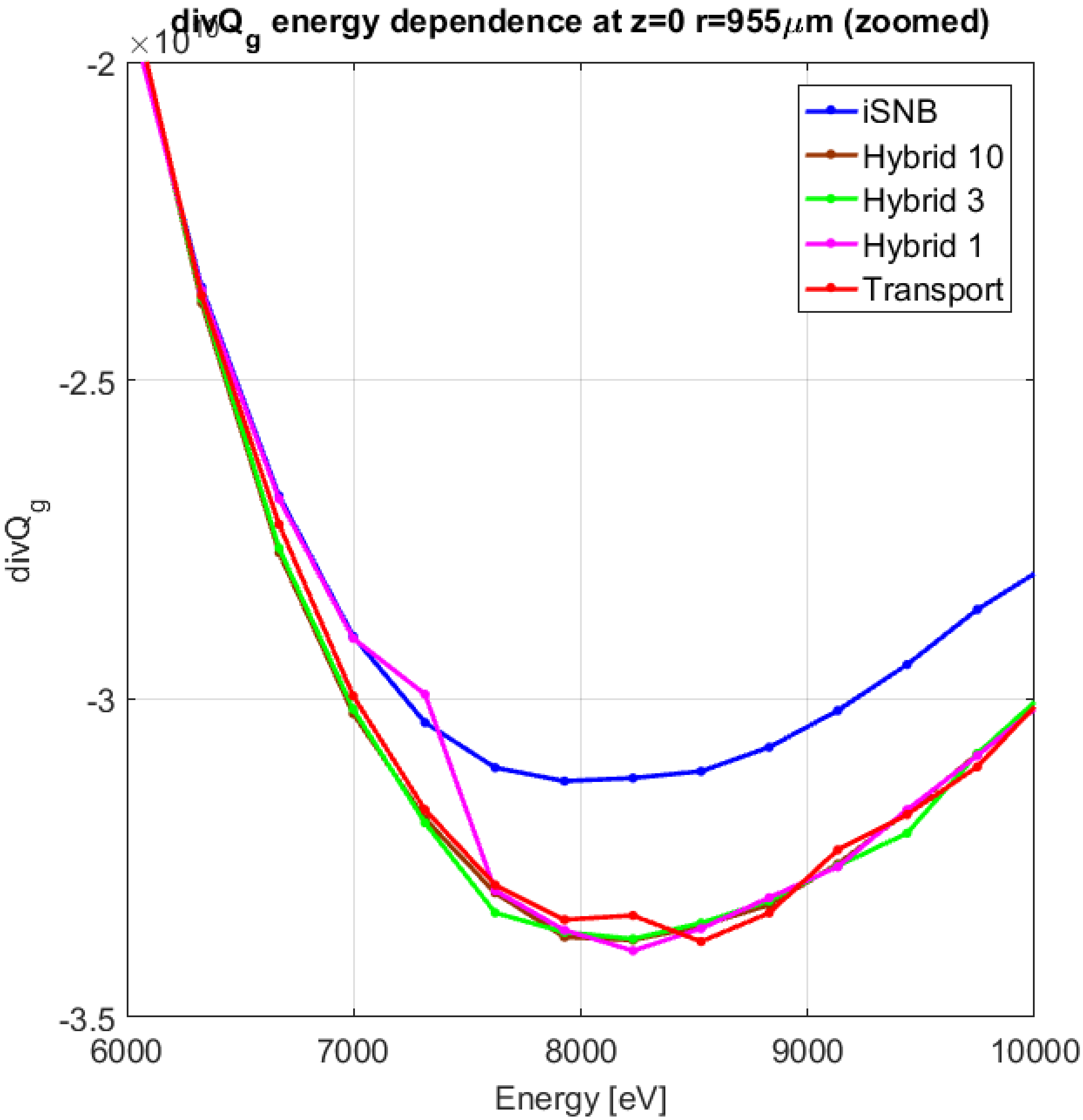

FIGURE 4.35: *Energy dependence of* $\nabla \cdot \mathbf{Q}$ *comparison for iSNB, pure transport and hybrid model with cutoffs of 1, 3, and 10 MFPs depicting the transition region between the high energy transport solution and low energy diffusion solution.*

At the critical density near 1110 μm the three hybrid solutions are nearly identical (aside for statistical variations due to differing effective numbers of particles) with the pure transport solution (Fig. 4.36). Below 3 keV the hybrid and pure transport solutions are nearly identical to the iSNB diffusion solution. Again transitions between the iSNB and pure transport solution can be seen upon zoom (not pictured), which can be used to gauge the effectiveness of the hybridization. At this spatial point the hybrid 1 solution has a transitional jump at 4 keV for about 3% of its value.

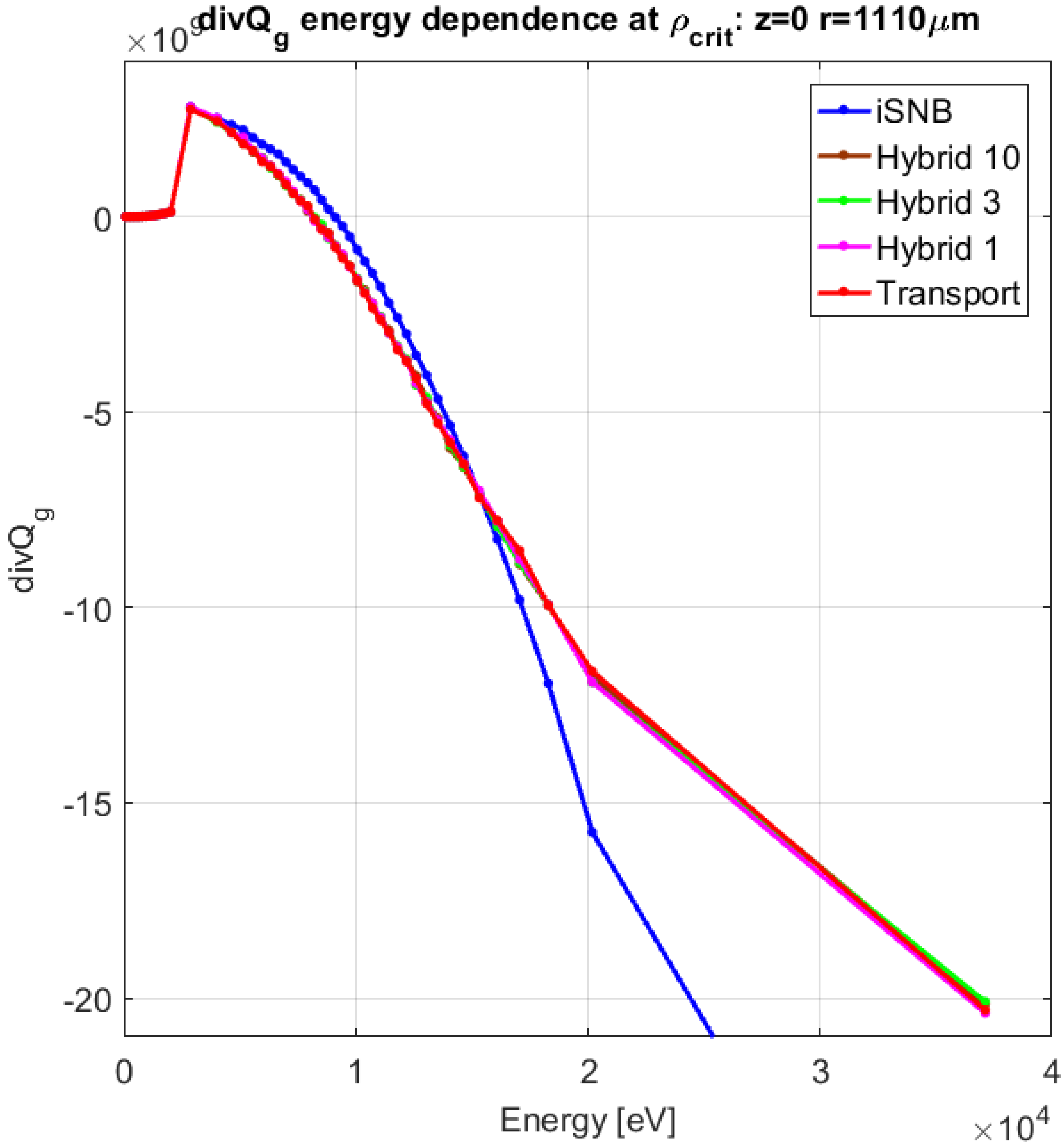

FIGURE 4.36: *Energy dependence of* $\nabla \cdot \mathbf{Q}$ *comparison for iSNB, pure transport and hybrid model with cutoffs of 1, 3, and 10 MFPs.*

Finally we turn our attention to the dense shell region of the target. Looking at the total $\nabla \cdot \mathbf{Q}$ quantity (Fig. 4.37) at the inner edge of the shell (below a radius of 910 μm) we see that the hybrid and pure transport methods match the iSNB diffusion solution as expected since the shell is optically thick and relatively cool thus producing a diffusive result. Near the outer edge of the shell at 922.7 μm, the iSNB method produces an exponentially decaying solution, which is typical of a diffusion solution. For the exponential solution $1/e$ or about 37% of the particle weight will remain after 1 MFP. The hybrid and transport methods however produce a much sharper cutoff, which is indicative of the finite range characteristic of charged particles. Looking at the energy distribution in Fig. 4.38, the iSNB method has a significantly higher contribution for groups above 10 keV to $\nabla \cdot \mathbf{Q}$ when compared to the ETTMC methods. This indicates that the iSNB solution allows more heat to enter the shell due to the exponential solution vs. the ETTMC methods which have a sharp cutoff at the particle range. The variance between the hybrid and pure transport methods in the highest energy group is likely due to statistical variation since few particles will penetrate deeply into the shell and the total $\nabla \cdot \mathbf{Q}$ is a couple orders of magnitude lower than the global peak $\nabla \cdot \mathbf{Q}$.

Overall, while the integrated solutions between the iSNB and transport methods are similar, under the hood there exists difference that may become important in future study. Furthermore, the pure transport results are well replicated by a hybrid model with a cutoff optical depth of 3 or 10. The hybrid method is thus useful since it can be used to reduce the total number of particles used (reducing runtime) or by reallocating particles to higher energy groups (improving statistics by allowing for a higher effective number of MCPs).

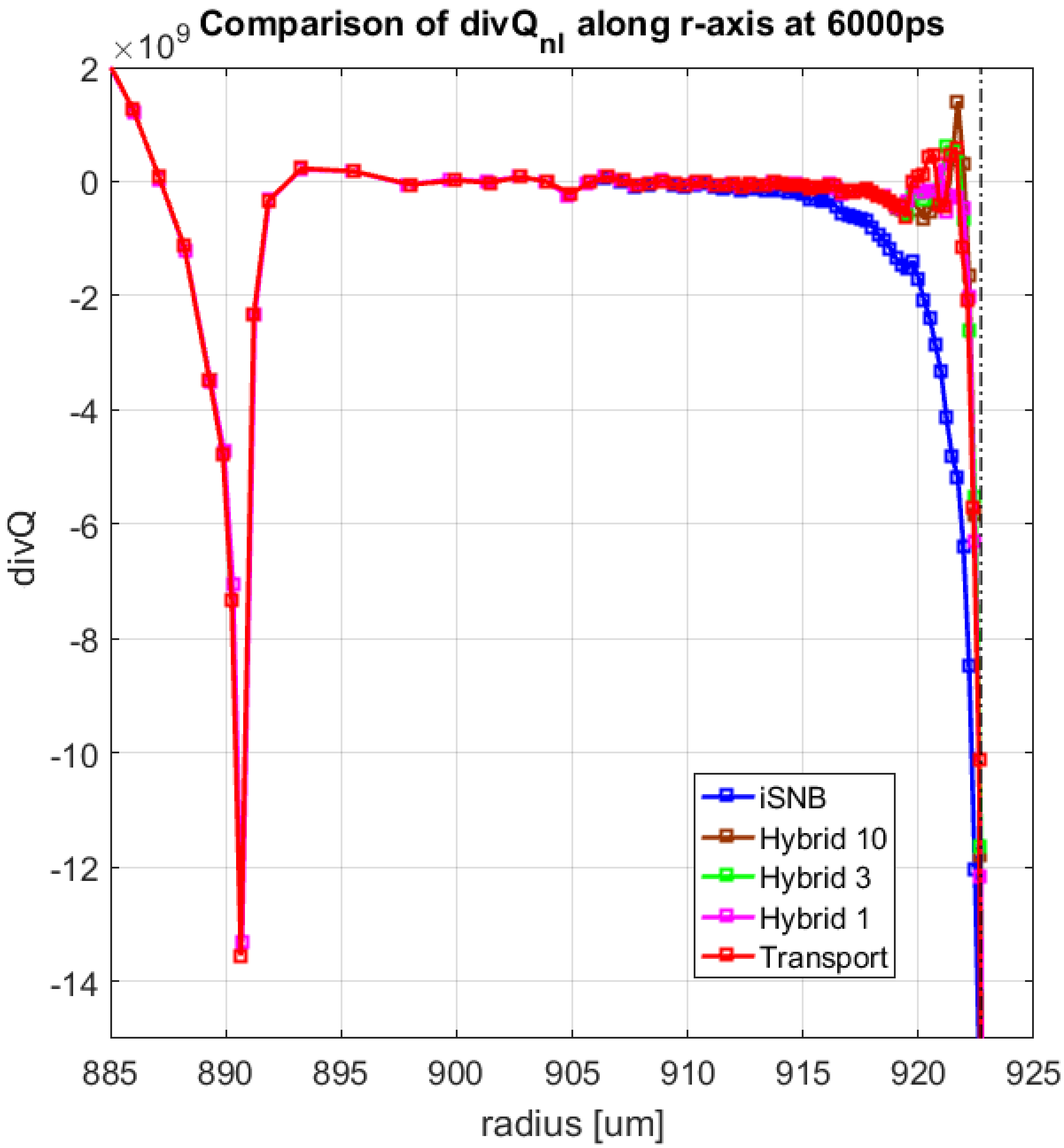

FIGURE 4.37: $\nabla \cdot \mathbf{Q}$ *along the r-axis zoomed on shell region of the phase plate asymmetry simulation at 6000ps with marked point of interest (dash dot lines) for hybrid* $\nabla \cdot \mathbf{Q}$ *comparison.*

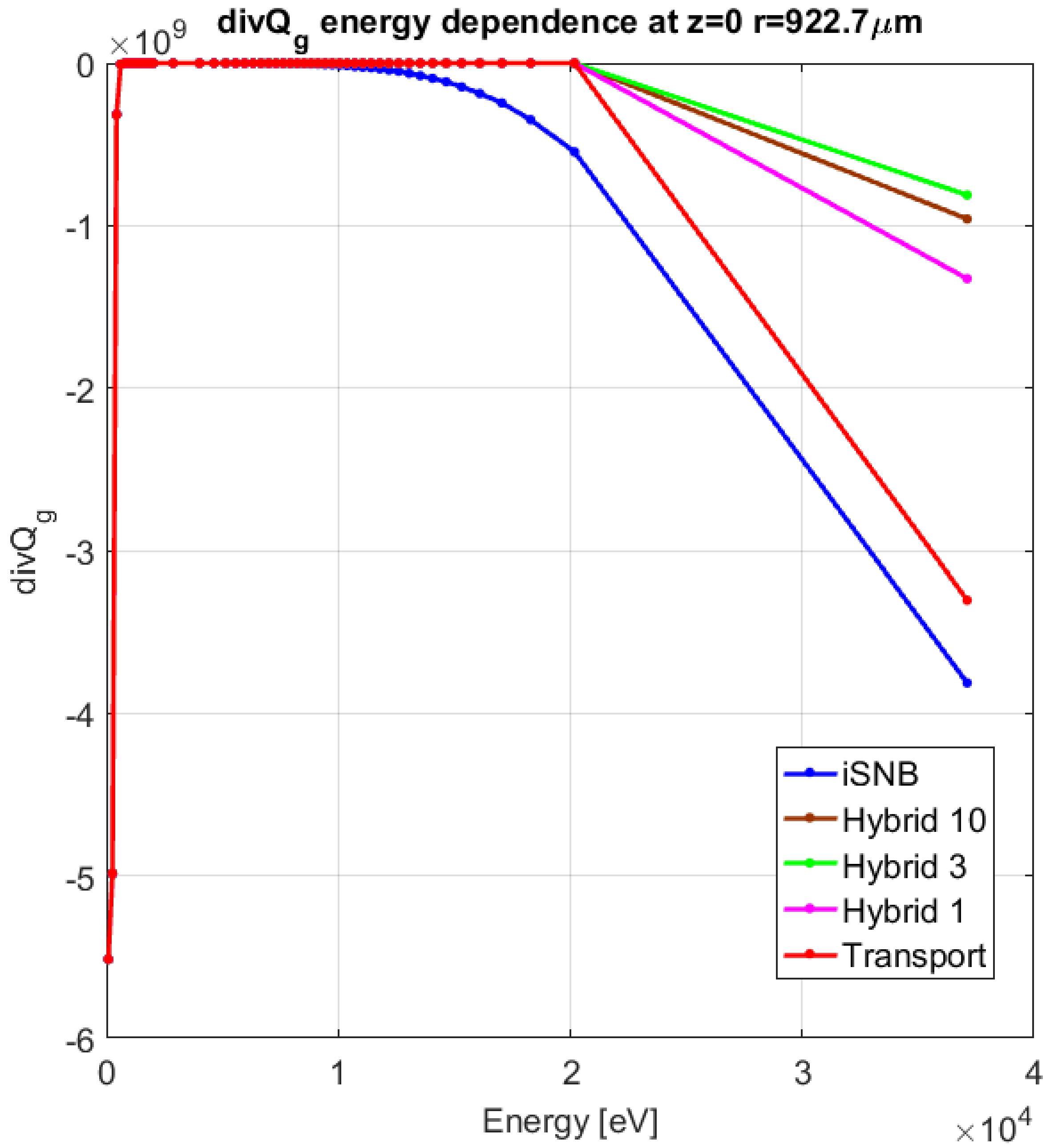

FIGURE 4.38: *Energy dependence of* $\nabla \cdot \mathbf{Q}$ *comparison for iSNB, pure transport and hybrid model with cutoffs of 1, 3, and 10 MFPs.*

Chapter 5

Conclusions

This thesis demonstrates that the ETTMC transport model can serve as a test of validity for the diffusion approximation iSNB model. Despite producing similar integrated results in the chosen test problems, there is evidence that there is a small reduction in the preheating with the ETTMC method versus the iSNB method. Looking at the energy distribution of the non-local heat flux divergence calculated by the two models the primary difference occurs at the higher energies. In the lowest energy groups the energy distributions are in agreement between the iSNB and ETTMC models. As such hybridization of the models is possible allowing the low energy end of the spectrum to be treated with the faster diffusion algorithm while allowing for additional particles to be freed up for use in the truly transport regime thus improving MC statistics (alternatively we could keep the number of particles the same in the high energy groups and reduce runtime). A series of test simulations with the NIF phase plate asymmetry simulation seem to indicate that a minimum 3 MFP per cell optical depth cutoff for diffusion is sufficient for the hybrid method to match the $\nabla \cdot \mathbf{Q}$ energy distribution for pure transport. In terms of performance, for the DRACO shot 60303 simulation the pure ETTMC method with 2.5×10^6 MCPs had 10 times longer runtime than iSNB. Furthermore, the hybrid method (cutoff 3 MFP) had a 10% shorter runtime than the pure transport method.

5.1 Future Work

Future work on the ETTMC model could delve into several avenues of research. The first is improved modeling of electromagnetic effects. Current modeling in both the ETTMC and iSNB methods ignores any contribution due to magnetic fields, which could affect electron behavior. Furthermore, only the local electric field, calculated via SH theory, is used in current modeling and may benefit from a non-local treatment. A second avenue of research is the interaction between the electron distribution function and the laser electric field. Such laser plasma interactions (LPI) are predicted to produce electrons in the 10's of keV and contribute to the high energy tail of the electron distribution function. As these LPI electrons are of high energy in comparison to the thermal temperature they will have long MFPs and can travel far from there point of origin contributing to target preheating. As such, including LPI electrons in our study of electron transport will likely improve modeling capability. Furthermore, current modeling of laser deposition is done independently of the results of electron thermal transport and there may be feedback effects that need model inclusion. Finally, theory predicts non-Maxwellian self-similar electron distributions to occur at certain laser intensities [27] and it may be beneficial to use one of these as a source energy distribution as opposed to the Maxwellian energy distribution used in the source term for the iSNB and ETTMC models.

Bibliography

[1] Jurgen Meyer ter Vehn and Stefano Atzeni. *The Physics of Inertial Fusion.* Oxford Science Publications, 2004.

[2] K.S. Krane. *Introductory Nuclear Physics.* John Wiley & Sons, Inc., New York, New York, 1988.

[3] F.F Chen. *Plasma Physics and Controlled Fusion, 2nd Ed.* Springer, New York, New York, 1983.

[4] Fusion reaction rates. `http://en.wikipedia.org/wiki/File:Fusion_rxnrate.svg`.

[5] Inertial confinement fusion: How to make a star, 2012. `https://lasers.llnl.gov/programs/nic/icf/`.

[6] E. Moses. Science and technology, 2003. `https://www.llnl.gov/str/September03/Moses.html`.

[7] E. D. Benjamin. Inertial confinement fusion, 2007. `http://en.wikipedia.org/wiki/File:Inertial_confinement_fusion.svg`.

[8] L. Spitzer and R. Harm. Transport phenomena in a completely ionized gas. *Physical Review*, 89, March 1953.

[9] J. F. Luciani, P. Mora, and J. Virmont. Nonlocal heat transport due to steep temperature gradients. *Physics Review Letter*, 51, 1983.

[10] E.D. Held, J.D Callen, C.C. Hegna, and C.R. Sovinec. Conductive electron heat flow along magnetic field lines. *Physics of Plasmas*, 8, 2001.

[11] E.D. Held, J.D Callen, and C.C. Hegna. Conductive electron heat flow along an inhomogenous magnetic field. *Physics of Plasmas*, 10, 2003.

[12] E.D. Held and et. al. Nonlocal closures for plasma fluid simulations. *Physics of Plasmas*, 11, 2004.

[13] G. P. Schurtz, Ph. D. Nicolai, and M. Busquet. A nonlocal electron conduction model for multidimensional radiation hydrodynamics codes. *Physics of Plasmas*, 7(10), October 2000.

[14] Ph. D. Nicolai, J. L. A. Feugeas, and G. P. Schurtz. A practical nonlocal model for heat transport in magnetized laser plasmas. *Physics of Plasmas*, 13, March 2006.

[15] D. Cao, J. Chenhall, E. Moll, A. Prochaska, G. Moses, J. Delettrez, and T. Collins. Nonlocal electron transport validation using 2d draco. *APS DPP Meeting*, October 2012.

[16] D. Cao, J. Chenhall, G. Moses, J. Delettrez, and T. Collins. Numerically robust and efficient nonlocal electron transport in 2d draco simulations. *APS DPP Meeting*, November 2013.

[17] D.Cao, G.A.Moses, and J.Delettrez. Improved non-local electron thermal transport for two-dimensional radiation hydrodynamics simulations. *Physics of Plasmas*, 22, 2015.

[18] T. R. Boehly, V. N. Goncharov, W. Seka, S. X. Hu, J. A. Marozas, D. D. Meyerhofer, P. M. Celliers, D. G. Hicks, M. A. Barrios, D. Fratanduono, and G. W. Collins. Multiple

spherically converging shock waves in liquid deuterium. *Physics of Plasmas*, 18, September 2011.

[19] S. Atzeni, A. Shiavi, and J.R. Davies. Stopping and scattering of relativistic electron beams in dense plasmas and requirements for fast ignition. *Plasma Physics and Controlled Fusion*, 51, 2009.

[20] V. N. Goncharov, O. V. Gotchev, E. Vianello, T. R. Boehly, J. P. Knauer, P. W. McKenty, P. B. Radha, S. P. Regan, T. C. Sangster, S. Skupsky, V. A. Smalyuk, R. Betti, R. L. McCrory, and D. D. Meyerhofer. Early stage of implision in inertial confinement fusion: Shock timing and perturbation evolution. *Physics of Plasmas*, 13, 2006.

[21] D. G. Colombant, W. M. Manheimer, and Valeri Goncharov. The development of a krook model for nonlocal transport in laser produced plasmas. i. basic theory. *Physics of Plasmas*, 15, 2008.

[22] D. G. Colombant and W.M. Manheimer. Internal tests and improvements of the krook model for nonlocal electron energy transport in laser produced plasmas. *Physics of Plasmas*, 17, 2010.

[23] A. Bendib, J.F. Luciani, and J.P. Matte. An improvement of the nonlocal heat flux formula. *Physics of Fluids*, 31, 1988.

[24] J.A.Delettrez. Omega shot 68951 lilac input deck provide by j.a. delettrez. *Personal Communication*, 2016.

[25] D. Cao, J.A. Marozas, T.J.B. Collins, P.B. Radha, and P.W. McKenty. An intermediate far-field spot design for polar direct drive at the national ignition facility. *APS DPP Meeting*, November 2015.

[26] T.J.B. Collins and et. al. A polar-drive-ignition deisgn for the national ignition facility. *Physics of Plasmas*, 19, 2012.

[27] A.B. Langdon. Nonlinear inverse bremsstrahlung and heated-electron distributions. *Physiccal Review Letters*, 44, 1980.

[28] J.A. Fleck Jr. and J.D. Cummings. An implicit monte carlo scheme for calculating time and frequency dependent radiation transport. *Journal of Computational Physics*, 8, 1971.

[29] G.C. Pomraning. *The Equations of Radiation Hydrodynamics*. Pergamon Press, Oxford, United Kingdom, 1973.

[30] J.D. Densmore and E.W. Larsen. Asymptotic equilibrium diffusion analysis of time-dependent monte carlo methods for grey radiative transfer. *Journal of Computational Physics*, 199, 2004.

[31] J.D. Densmore, G. Davidson, and D.B. Carrington. Emissivity of discretized diffusion problems. *Annals of Nuclear Energy*, 33, 2006.

[32] J.D. Densmore, T.J. Urbatsch, T.M. Evans, and M.W. Buksas. A hybrid transport-diffusion method for monte carlo radiative-transfer simulations. *Journal of Computational Physics*, 222, 2007.

[33] J.D. Densmore. Asymptotic analysis of the spatial discretization of radiation absorption and re-emission in implicit monte carlo. *Journal of Computational Physics*, 230, 2011.

[34] E. Abdikamalov, A. Burrows, C.D. Ott, F. Loffler, E. O'Connor, J.C. Dolence, and E. Schnetter. A new monte carlo method for time-dependent neutrino radiation transport. *The Astrophysical Journal*, 755, 2012.

[35] G.J. Habetler and B.J. Matkowsky. Uniform asymptotic expansions in transport theory with small mean free paths, and the diffusion approximation. *Journal of Mathematical Physics*, 16, 1975.

[36] E. Gelbard, J. Davis, and J. Pearson. Iterative solutions to the p1 and double-p1 equations. *Nuclear Science and Engineering*, 5, 1959.

[37] E.M. Gelbard. Application of spherical harmonics methods to reactor problems. *WAPD-BT-20, bettis Atomic Power Laboratory*, 1960.

[38] E.W. Larsen, J.E. Morel, and J.M McGhee. Asymptotic derivation of the multigroup p1 and simplified pn equations with anisotropic scattering. *Nuclear Science and Engineering*, 123, 1996.

[39] P.S. Brantley and E.W. Larsen. The simplified p3 approximation. *Nuclear Science and Engineering*, 134, 2000.

Appendix A

Radiative Transport

A.1 Radiative Transport Background

In contrast to the deterministic methods, Monte Carlo (MC) methods allow for greater fidelity in the treatment of particle directional dependence through scattering and allow for more complicated geometries. In the following sections, several MC techniques will be discussed as they pertain to radiative transport. The scope of the thesis project will be devoted to adapting these methods to electron thermal conduction problems.

A.1.1 Implicit Monte Carlo (IMC)

Fleck and Cummings developed an Implicit Monte Carlo (IMC) method in order to increase stability of coupling the radiation field to the electron energy equation over traditional MC methods [28]. For optically thin and non-equilibrium systems unmodified MC methods produce accurate results. However, for systems near thermodynamic equilibrium or with larger absorption cross sections, large fluctuations, energy imbalances and requirements for small time steps can occur. The IMC method developed by Fleck and Cummings attempts to remedy these issues by reformulating the radiative transport equations in terms of effective scattering and absorption cross sections, which allow for a larger time step while preserving numerical accuracy and stability.

The grey radiative transfer equations are

$$\frac{1}{c}\frac{\partial I}{dt} + \mu\frac{\partial I}{\partial x} + \sigma I = \frac{1}{2}\sigma a c T^4, \tag{A.1a}$$

$$\frac{\partial u_m}{\partial t} = \sigma\left(\int_{-1}^{1} I d\mu - acT^4\right) + S \tag{A.1b}$$

where $I(x,t,\mu)$ is the specific intensity, T is the material temperature, u_m is the material energy density, μ is the direction cosine in the x direction, a is the radiation energy density constant and S is an energy source term (Note the scattering term has been omitted for simplicity of discussion) [29]. Rewriting Eqs. (A.1) in terms of the radiation energy density variable

$$u_r = aT^4, \tag{A.2}$$

$$\frac{\partial u_m}{\partial u_r} = \beta^{-1}, \tag{A.3}$$

the equations become

$$\frac{1}{c}\frac{\partial I}{dt} + \mu\frac{\partial I}{\partial x} + \sigma I = \frac{1}{2}c\sigma u_r, \tag{A.4a}$$

$$\frac{\partial u_r}{\partial t} = \beta\sigma\left(\int_{-1}^{1} I d\mu - cu_r\right) + \beta S. \tag{A.4b}$$

The advantage of this form of the equations is that the non-linearities of the problem are contained within the multiplicative factor β. Integrating Eq. (A.4b) over a single time step from t^n to t^{n+1}

$$u_r^{n+1} - u_r^n = \int_{t^n}^{t^{n+1}} dt\beta\sigma \int_{-1}^{1} I d\mu - c\int_{t^n}^{t^{n+1}} dt\beta\sigma u_r + \int_{t^n}^{t^{n+1}} dt\beta S. \tag{A.5}$$

Rewriting the integrals in terms of time averaged values gives

$$u_r^{n+1} - u_r^n = \Delta t\bar{\beta}\bar{\sigma}\left\{\int_{-1}^{1} I^\lambda d\mu - c[\alpha u_r^{n+1}(1-\alpha)u_r^n]\right\} + \bar{\beta}S^\gamma \Delta t \tag{A.6}$$

where coefficient α and superscripts λ and γ are time centering parameters. Solving for the updated radiation energy density and suppressing the time averaging notation over β and σ for simplicity gives

$$u_r^{n+1} = \left[\frac{1-(1-\alpha)\beta c\Delta t\sigma}{1+\alpha\beta c\Delta t\sigma}\right] u_r^n + \frac{\beta\Delta t\sigma}{1+\alpha\beta c\Delta t\sigma}\int I^\lambda d\mu + \frac{\beta\Delta t S^\gamma}{1+\alpha\beta c\Delta t\sigma}. \tag{A.7}$$

Solving for a time averaged value of u_r^γ yields

$$u_r^\gamma = \alpha u_r^{n+1}(1-\alpha)u_r^n = \frac{\alpha\beta\Delta t\sigma}{1+\alpha\beta c\Delta t\sigma}\int I^\lambda d\mu + \frac{u_r^n}{1+\alpha\beta c\Delta t\sigma} + \frac{\alpha\beta\Delta t S^\gamma}{1+\alpha\beta c\Delta t\sigma}. \tag{A.8}$$

Replacing u_r in Eq. (A.4a) with the time centered u_r^γ gives

$$\frac{1}{c}\frac{\partial I}{dt} + \mu\frac{\partial I}{\partial x} + \sigma I = \frac{1}{2}\sigma\left(\frac{\alpha\beta c\Delta t\sigma}{1+\alpha\beta c\Delta t\sigma}\right)\int I^\lambda d\mu + \frac{1}{2}\left(\frac{c\sigma}{1+\alpha\beta c\Delta t\sigma}u_r^n + \frac{\sigma\alpha\beta c\Delta t S^\gamma}{1+\alpha\beta c\Delta t\sigma}\right) \tag{A.9}$$

which is assumed to be valid over Δt. The effective absorption and scattering cross sections are

$$\sigma_{ea} = \frac{1}{1+\alpha\beta c\Delta t\sigma}\sigma, \tag{A.10a}$$

$$\sigma_{es} = \frac{\alpha\beta c\Delta t\sigma}{1+\alpha\beta c\Delta t\sigma}\sigma. \tag{A.10b}$$

Integrating Eqs. (A.4) over angle and combining to describe the energy balance gives

$$\begin{aligned}\frac{1}{c}\frac{\partial}{dt}\int I d\mu + \frac{\partial F}{\partial x} &= -\,\sigma \int I d\mu + \sigma\left(\frac{\alpha\beta c\Delta t\sigma}{1+\alpha\beta c\Delta t\sigma}\right)\int I d\mu + \frac{\sigma\alpha\beta c\Delta t S^{\gamma}}{1+\alpha\beta c\Delta t\sigma} \\ &\quad + \frac{c\sigma}{1+\alpha\beta c\Delta t\sigma}u_r^n \\ &= -\,\frac{1}{\beta}\frac{\partial u_r}{\partial t} + S^{\gamma}.\end{aligned} \tag{A.11}$$

Collecting the common terms gives the energy balance equation

$$\frac{\partial u_m}{\partial t} = \frac{\sigma}{1+\alpha\beta c\Delta t\sigma}\int I d\mu - \frac{c\sigma u_r^n}{1+\alpha\beta c\Delta t\sigma} + \frac{S^{\gamma}}{1+\alpha\beta c\Delta t\sigma}. \tag{A.12}$$

Equation (A.12) is integrated over Δt to get the updated material energy density

$$u_m^{n+1} = u_m^n + \frac{\sigma}{1+\alpha\beta c\Delta t\sigma}\int_{t^n}^{t^{n+1}}\int I d\mu\, dt - \frac{c\Delta t\sigma u_r^n}{1+\alpha\beta c\Delta t\sigma} + \frac{S^{\gamma}\Delta t}{1+\alpha\beta c\Delta t\sigma}. \tag{A.13}$$

The updated temperature can be solved for by making use of the specific heat $\partial u_m/\partial T = C_v$ via

$$T^{n+1} = T^n + C_v^{-1}\left\{\frac{\sigma}{1+\alpha\beta c\Delta t\sigma}\int_{t^n}^{t^{n+1}}\int I d\mu\, dt - \frac{c\Delta t\sigma u_r^n}{1+\alpha\beta c\Delta t\sigma} + \frac{S^{\gamma}\Delta t}{1+\alpha\beta c\Delta t\sigma}\right\}. \tag{A.14}$$

The MC transport scheme can be described as followed. At time $t = t^n$, the quantities I, T, and u_r are known, starting with those values I, T, and u_r are solved for at time $t = t^{n+1} = t^n + \Delta t$. The spatial domain of the problem is divided into a discrete set of zones and the temperature within each zone is assumed to be uniform. The initial conditions are provided by a census of the MC particles in transit at the end of the previous time step.

Algorithm:

1. Starting at time t^n, quantities β and σ are evaluated for each spatial zone.

2. From S and u_r^n the source terms are computed for each spatial zone. New particles are generated from the source and are transported along with the census particles from the previous time step via the transport equation

   $$\frac{1}{c}\frac{\partial I}{dt}+\mu\frac{\partial I}{\partial x}+(\sigma_{ea}+\sigma_{es})I=\frac{1}{2}\sigma_{es}\int I d\mu+\frac{1}{2}\left(\frac{c\sigma}{1+\alpha\beta c\Delta t\sigma}u_r^n+\frac{\sigma\alpha\beta c\Delta t S^{\gamma}}{1+\alpha\beta c\Delta t\sigma}\right). \quad \text{(A.15)}$$

   The solution to Eq. (A.15) will contain the census of particles at the end of the time step at $t = t^{n+1}$. The non-scattering source terms on the RHS of Eq. (A.15) are assumed constant throughout the time step and consequently new particles will be generated uniformly within the time step.

3. In solving Eq. (A.15) the quantity

   $$\frac{\sigma}{1+\alpha\beta c\Delta t\sigma}\int_{t^n}^{t^{n+1}}\int I d\mu\, dt \quad \text{(A.16)}$$

   is tabulated by tracking the particle energy deposited via effective absorption within each zone. The temperature at $t = t^{n+1}$ can then be solved via the temperature equation (A.14).

A.1.2 Discrete Diffusion Monte Carlo (DDMC)

For optically thick problems IMC has the downside that the effective scattering term dominates particle interactions. Since scattering dominates, particle histories are longer, which results in higher computational costs. To correct for this inefficiency in optically thick regions Densmore et. al. develop a Discrete Diffusion Monte Carlo (DDMC) method [30][31][32][33]. In DDMC, the IMC formalism is approximated by a diffusion equation, which can then be solved via

MC methods. The DDMC method allows for shorter particle histories in general by replacing many small scattering steps with a single diffusion step. IMC and DDMC are combined in a hybrid model (IMC-DDMC), which allows for the flexibility of using IMC transport in optically thin regions and DDMC in optically thick models. In addition to the radiative transfer IMC-DDMC model developed by Densmore, Abdikamalov et. al. have successfully applied IMC-DDMC to neutrino transport problems [34].

The DDMC derivation starts with the angular integrated form of the IMC equations

$$\frac{1}{c}\frac{\partial \phi}{\partial t} + \frac{\partial F}{\partial x} + f_n \sigma_n \phi = f_n \sigma_n a c T_n^4, \tag{A.17}$$

$$f_n = \frac{1}{1 + \beta_n c \sigma_n \Delta t_n}, \tag{A.18}$$

$$\beta_n = \frac{4aT_n^3}{C_{v,n}} \tag{A.19}$$

where ϕ and F are the zeroth and first angular moments of radiation intensity, n refers to the time step, and f_n is the Fleck factor defining the effective cross sections. Discretizing Eq. (A.17) over spatial cell j produces

$$\frac{1}{c}\frac{d}{dt}\phi_j + \frac{1}{\Delta x_j}\left(F_{j+1/2} - F_{j-1/2}\right) + f_{n,j}\sigma_{n,j}\phi_j = f_{n,j}\sigma_{n,j} a c T_{n,j}^4, \tag{A.20}$$

$$\phi_j(t) = \frac{1}{\Delta x_j}\int_{x_{j-1/2}}^{x_{j+1/2}} \phi(x,t)dx \tag{A.21}$$

where the cell edge flux is

$$F_{j+1/2}(t) = F(x_{j+1/2}, t) \tag{A.22}$$

The flux F can be written in terms of ϕ via Fick's law

$$F(x) = -\frac{1}{3\sigma}\frac{\partial \phi}{\partial x}. \tag{A.23}$$

In order to solve Eq. (A.20) the cell edge flux values must be continuous across cell boundaries. Applying Fick's law to F gives

$$F^{-}_{j+1/2} = -\frac{2}{3\sigma^{-}_{n,j+1/2}\Delta x_j}\left(\phi_{j+1/2} - \phi_j\right) \tag{A.24}$$

for the right edge flux in cell j and

$$F^{+}_{j+1/2} = -\frac{2}{3\sigma^{+}_{n,j+1/2}\Delta x_{j+1}}\left(\phi_{j+1} - \phi_{j+1/2}\right) \tag{A.25}$$

for the left edge flux in cell $j+1$. Equating the two edge expressions gives a solution for the cell edge scalar intensity

$$\phi_{j+1/2} = \frac{1}{\sigma^{-}_{n,j+1/2}\Delta x_j + \sigma^{+}_{n,j+1/2}\Delta x_{j+1}}\left(\sigma^{+}_{n,j+1/2}\Delta x_{j+1}\phi_j + \sigma^{-}_{n,j+1/2}\Delta x_j \phi_{j+1}\right). \tag{A.26}$$

Substituting $\phi_{j+1/2}$ into F_{j+1} gives

$$F_{j+1/2} = -\frac{2}{3}\frac{1}{\sigma^{-}_{n,j+1/2}\Delta x_j + \sigma^{+}_{n,j+1/2}\Delta x_{j+1}}\left(\phi_{j+1} - \phi_j\right). \tag{A.27}$$

Plugging in $F_{j+1/2}$ and a similar expression for $F_{j-1/2}$ into Eq. (A.20) produces an equation only dependent on the cell centered scalar intensities

$$\frac{1}{c}\frac{d}{dt}\phi_j + (\sigma_{L,j} + \sigma_{R,j} + f_{n,j}\sigma_{n,j})\phi_j = f_{n,j}\sigma_{n,j}acT^4_{n,j} + \frac{1}{\Delta x_j}(\sigma_{L,j+1}\phi_{j+1}\Delta x_{j+1} + \sigma_{R,j-1}\phi_{j-1}\Delta x_{j-1}). \tag{A.28}$$

In order to simplify notation, the left and right cell leakage cross sections have been defined as

$$\sigma_{L,j} = \frac{2}{3\Delta x_j}\frac{1}{\sigma^+_{n,j-1/2}\Delta x_j + \sigma^-_{n,j-1/2}\Delta x_{j-1}}, \tag{A.29a}$$

$$\sigma_{R,j} = \frac{2}{3\Delta x_j}\frac{1}{\sigma^-_{n,j+1/2}\Delta x_j + \sigma^+_{n,j+1/2}\Delta x_{j+1}}. \tag{A.29b}$$

To give Eq. (A.28) a MC interpretation, the equation can be viewed as a time-dependent infinite-medium problem for each cell. Each DDMC particle contains information on its current cell and time, but no position or angular position is stored. A particle streams until it undergoes a collision. The time to collision τ is distributed exponentially and can be sample via

$$\tau = -\frac{1}{c}\cdot\frac{1}{\sigma_{L,j} + \sigma_{R,j} + f_{n,j}\sigma_{n,j}}\ln\xi \tag{A.30}$$

where ξ is a uniformly distributed number between 0 and 1. If the time to collision is less than the time remaining in the time step, the particle undergoes a collision and the time left in the time step is decremented appropriately. The collision type is sampled via a histogram distribution with the possible reactions being left-leakage, right-leakage, and absorption reactions. The left-leakage, right-leakage, and absorption reactions occur with probability proportional to $\sigma_{L,j}$, $\sigma_{R,j}$, and $f_{n,j}\sigma_{n,j}$ respectively. If a left or right leakage reaction occurs the particle is transferred to the proper neighboring cell and the particle history continues. If the particle is absorbed the particle history is terminated and its energy is deposited in the cell. If the time to collision is greater than the time remaining in the time step the particle is saved in the cell for simulation during the next time step. Note that as the cross section increases the leakage opacities decrease while the absorption cross section is an $O(1)$ quantity. As the absorption opacity is $O(1)$ the time to collision does not become unreasonably small and collisions are primarily absorptive. This makes particle histories relatively short.

It is recommend that the cell edge opacities $\sigma^+_{n,j+1/2}$ and $\sigma^-_{n,j+1/2}$ be evaluated at a common interpolated temperature

$$T_{n,j+1/2} = \left(\frac{T^4_{n,j} + T^4_{n,j+1}}{2}\right)^{1/4}. \tag{A.31}$$

This is done because if one of the opacities is significantly larger, the entire expression can be small resulting in the radiation not propagating. By using a common temperature, the cell edge opacities can be kept at similar magnitudes across cell boundaries.

A.1.3 Interface Conditions

In order to interface DDMC with standard MC an appropriate set of boundary conditions must be used. Considering the leftmost boundary for $j = 1$ Eq. (A.20) becomes

$$\frac{1}{c}\frac{d}{dt}\phi_1 + (\sigma_{R,1} + f_{n,1}\sigma_{n,1})\phi_1 - \frac{1}{\Delta x_1}F_{1/2} = f_{n,1}\sigma_{n,1}acT^4_{n,1} + \frac{1}{\Delta x_1}\sigma_{L,2}\phi_2\Delta x_2. \tag{A.32}$$

Densmore recommends the use of the asymptotic diffusion-limit boundary condition of Habetler and Matkowsky as opposed to the standard Marshak boundary conditions [32][35]. The asymptotic diffusion-limit boundary condition is

$$2\int_0^1 W(\mu)I_b(\mu,t)d\mu = \phi(X_L,t) - \frac{\lambda}{\sigma_n}\frac{\partial\phi}{\partial x}\bigg|_{x=X_L} \tag{A.33}$$

where $I_b(\mu,t)$ is the radiation intensity incident on the DDMC region, $\lambda \approx 0.7104$ is the extrapolation distance, and $W(\mu)$ is a transcendental function approximated by

$$W(\mu) \approx \mu + \frac{3}{2}\mu^2. \tag{A.34}$$

The function $W(\mu)$ acts to weigh the incoming MC particles in order to handle anisotropies in the distribution as opposed to the Marshak boundary conditions that treats all incoming particles with the same weight. Discretizing Eq. (A.33)

$$2\int_0^1 W(\mu)I_b(\mu,t)d\mu = \phi_{1/2} - \frac{2\lambda}{\sigma_{n,1}\Delta x_1}(\phi_1 - \phi_{1/2}) \tag{A.35}$$

and solving for $\phi_{1/2}$ yields

$$\phi_{1/2} = \frac{2\lambda}{\sigma_{n,1}\Delta x_1 + 2\lambda}\phi_1 + \frac{2\sigma_{n,1}\Delta x_1}{\sigma_{n,1}\Delta x_1 + 2\lambda}\int_0^1 W(\mu)I_b(\mu,t)d\mu. \tag{A.36}$$

Applying Fick's Law to $F_{1/2}$

$$F_{1/2} = -\frac{2}{3\sigma_{n,1}\Delta x_1}(\phi_1 - \phi_{1/2}) \tag{A.37}$$

and plugging in $\phi_{1/2}$ gives

$$F_{1/2} = -\frac{2}{3\sigma_{n,1}\Delta x_1 + 6\lambda}\left(\phi_1 - 2\int_0^1 W(\mu)I_b(\mu,t)d\mu\right). \tag{A.38}$$

The left boundary DDMC equation is

$$\frac{1}{c}\frac{d}{dt}\phi_1 + (\sigma_{L,1} + \sigma_{R,1} + f_{n,1}\sigma_{n,1})\phi_1 = f_{n,1}\sigma_{n,1}acT^4_{n,1} + \frac{1}{\Delta x_1}\left(\sigma_{L,2}\phi_2\Delta x_2 + \int_0^1 P(\mu)\mu I_b(\mu,t)d\mu\right) \tag{A.39}$$

where

$$\sigma_{L,1} = \frac{1}{\Delta x_1}\frac{2}{3\sigma_{n,1}\Delta x_1 + 6\lambda} \tag{A.40}$$

and

$$P(\mu) = \frac{4}{3\sigma_{n,1}\Delta x_1 + 6\lambda}\left(1 + \frac{3}{2}\mu\right). \tag{A.41}$$

The other variables are defined as in Eq. (A.28). The integral term on the right hand side of Eq. (A.39) has the interpretation of the number of incoming MC particles converted to DDMC particles. The radiation intensity in direction μ incident on the DDMC region is μI_b. Thus $P(\mu)$ has an interpretation as the probability that a MC particle with direction μ is converted into a DDMC particle. An incident particle that enters the DDMC region is uniformly distributed with cell $j = 1$ and transported via DDMC. Particles that do not become DDMC particles are returned to the optically thin region isotropically.

A.2 Electron Thermal Transport DDMC

A.2.1 1D Spherical Coordinates

The full Boltzmann Transport Equation for electrons is given by

$$\frac{\partial f}{\partial t} + \mathbf{v} \cdot \nabla f - \frac{e}{m_e}\mathbf{E} \cdot \frac{\partial f}{\partial \mathbf{v}} = \left(\frac{\partial f}{\partial t}\right)_{col}. \tag{A.42}$$

The Boltzmann transport equation is coupled to the electron energy equation.

$$\rho C_v \frac{\partial T}{\partial t} = -\nabla \cdot \mathbf{Q} + S_{ext}. \tag{A.43}$$

In order to derive a DDMC equivalent version of the SNB we begin with Eq. (2.13). Taking the first and second angular moments gives

$$H_g(\mathbf{r}) = -\lambda_g(\mathbf{r}) \nabla \cdot \mathbf{Q}_g(\mathbf{r}) \tag{A.44}$$

and

$$\frac{\lambda_g(\mathbf{r})}{3}\nabla H_g(\mathbf{r}) + \mathbf{Q}_g(\mathbf{r}) = \mathbf{U}_g(\mathbf{r}). \tag{A.45}$$

Rewriting the moment equations in 1D spherical geometry gives

$$H_g(r) = -\lambda_g(r)\frac{1}{r^2}\frac{\partial(r^2 Q_g(r))}{\partial r}, \tag{A.46}$$

$$\frac{\lambda_g'(r)}{3}\frac{\partial H_g(r)}{\partial r} + Q_g(r) = U_g(r). \tag{A.47}$$

Discretizing Eq. (A.46) over a spatial cell j gives

$$\frac{1}{r_j^2 \Delta r_j^c}(r_{j+1/2}^2 Q_{g,j+1/2} - r_{j-1/2}^2 Q_{g,j-1/2}) + \sigma_{g,j} H_{g,j} = 0 \tag{A.48}$$

where $\sigma_{g,j} = 1/\lambda_{g,j}$, $\sigma'_{g,j} = 1/a\lambda_e + |eE|/k_b T_e$ and cell width $\Delta r_j^c = r_{j+1/2} - r_{j-1/2}$. By requiring that Q_g and U_g be continuous across cell boundaries and applying Eq. (A.45) at the $j + 1/2$ boundary yields

$$Q_{g,j+1/2}^{+} = U_{g,j+1/2} - \frac{2}{\sigma'^{+}_{g,j+1/2}\Delta r_{j+1}}(H_{g,j+1} - H_{g,j+1/2}) \tag{A.49}$$

and

$$Q_{g,j+1/2}^{-} = U_{g,j+1/2} - \frac{2}{\sigma'^{-}_{g,j+1/2}\Delta r_{j}}(H_{g,j+1/2} - H_{g,j}). \tag{A.50}$$

Equating the two edge expressions and solving for $H_{g,j+1/2}$ gives

$$H_{g,j+1/2} = \frac{1}{\sigma^{-}_{g,j+1/2}\Delta r_j + \sigma^{+}_{g,j+1/2}\Delta r_{j+1}}\left(\sigma^{+}_{g,j+1/2}\Delta r_{j+1} H_{g,j} + \sigma^{-}_{g,j+1/2}\Delta r_j H_{g,j+1}\right) \tag{A.51}$$

and the cell edge $Q_{g,j+1/2}$ is

$$Q_{g,j+1/2} = U_{g,j+1/2} - \frac{2}{\sigma^{-}_{g,j+1/2}\Delta r_j + \sigma^{+}_{g,j+1/2}\Delta r_{j+1}}(H_{g,j+1} - H_{g,j}). \tag{A.52}$$

Plugging the $Q_{g,j+1/2}$ and a similar expression for $Q_{g,j-1/2}$ into Eq. (A.48) produces an equation only in terms of the cell centered heat fluxes

$$\begin{aligned}&(\sigma_{g,L,j} + \sigma_{g,R,j} + \sigma_{g,j})H_{g,j} \\ &= \frac{1}{r_j^2 \Delta r_j^c}[\sigma_{g,L,j+1}H_{g,j+1}r_{j+1}^2\Delta r_{j+1}^c + \sigma_{g,R,j}H_{g,j-1}r_{j-1}^2\Delta r_{j-1}^c - (r_{j+1/2}^2 U_{g,j+1/2} - r_{j-1/2}^2 U_{g,j-1/2})]\end{aligned} \tag{A.53}$$

or

$$\begin{aligned}&(\sigma_{g,L,j} + \sigma_{g,R,j} + \sigma_{g,j})H_{g,j} \\ &= \frac{1}{V_j}[\sigma_{g,L,j+1}H_{g,j+1}V_{j+1} + \sigma_{g,R,j}H_{g,j-1}V_{j-1} - (A_{j+1/2}U_{g,j+1/2} - A_{j-1/2}U_{g,j-1/2})]\end{aligned} \tag{A.54}$$

where $V_j = 4\pi r_j^2 \Delta r_j^c = 4\pi/3(r_{j+1/2}^3 - r_{j-1/2}^3)$ is the cell volume and $A_j = 4\pi r_j^2$ is the surface area of a sphere radius r_j. Note this requires that we define the cell centered radius as

$$r_j^2 = \frac{1}{3}(r_{j+1/2}^2 + r_{j+1/2}r_{j-1/2} + r_{j-1/2}^2) \tag{A.55}$$

for consistency. The left and right cell leakage cross sections have been defined as

$$\sigma_{g,L,j} = \frac{1}{3}\frac{A_{j-1/2}}{V_j}\frac{1}{\sigma'^{+}_{g,j-1/2}\Delta r_j^L + \sigma'^{-}_{g,j-1/2}\Delta r_{j-1}^R}, \tag{A.56}$$

$$\sigma_{g,R,j} = \frac{1}{3}\frac{A_{j+1/2}}{V_j}\frac{1}{\sigma'^{+}_{g,j+1/2}\Delta r_{j+1}^L + \sigma'^{-}_{g,j+1/2}\Delta r_j^R} \tag{A.57}$$

where $r_j^L = r_j - r_{j-1/2}$ and $r_j^R = r_{j+1/2} - r_j$. For 1D slab and cylindrical geometries Eq. (A.54) remains valid provided we define $A_j^{slab} = 1$, $V_j^{slab} = r_{j+1/2} - r_{j-1/2}$ and $A_j^{cylinder} = 2\pi r_j$, $V_j^{cylinder} = \pi(r_{j+1/2}^2 - r_{j-1/2}^2)$ respectively. To give Eq. (A.54) a MC interpretation, the equation can be viewed as a time independent infinite medium transport problem for each cell. Each DDMC particle contains information on its current cell, but no position, angular, or temporal information is contained. The DDMC particle is advanced by sampling interaction type via a histogram distribution with the possible reactions being left-leakage, right-leakage, and absorption reactions with probabilities proportional to $\sigma_{g,L,j}$, $\sigma_{g,R,j}$, and $\sigma_{g,j}$ respectively. If a left or right leakage reaction occurs, the particle is transferred to the appropriate neighboring cell and the particle history continues. Note that the leaked particles are distributed uniformly within their new cell. If the particle undergoes absorption the particle history terminates and the particle is added to that cells heat flux tally.

Defining:

$$S_{g,j} = -\frac{A_{j+1/2}U_{g,j+1/2} - A_{j-1/2}U_{g,j-1/2}}{V_j} \tag{A.58}$$

DDMC particles are allocated to each cell in proportion to the source term magnitude in that cell

$$N_{g,j} = N_{tot} \cdot \left\lceil \frac{|S_{g,j}|}{\sum_g \sum_j |S_{g,j}|} \right\rceil . \tag{A.59}$$

Particles weights are generated in proportion to the source value in their parent cell

$$w_{g,j} = \frac{S_{g,j}}{N_{g,j}} \cdot V_j \tag{A.60}$$

where $N_{g,j}$ is the number of DDMC particles in group g starting in cell j. When a particle undergoes absorption in a cell that particle's weight is added to that cell's flux tally and the particle is uniformly distributed within that cell. Note that particle weights can be positive or negative depending on the sign of the SH heat flux. After all particle histories are tabulated, the resultant tallies give the non-local heat flux gradient in each cell

$$-\nabla Q_j^{nl} = \frac{1}{V_j}\sum_g\sum_{j'} N_{g,j'\to j} w_{g,j'}. \tag{A.61}$$

To compute the error we note that

$$w_{g,j} \approx sign(S_{g,j})\frac{1}{N_{tot}}\sum_g\sum_{j'} |S_{g,j'}| \cdot V_j \tag{A.62}$$

only varies with cell volume. The weights are modified only by the volume ratio and sign of the source. This gives a relative MC statistical error of

$$(\text{Error})_j = \frac{\sqrt{\sum_g \sum_{j'} N_{g,j'\to j} w_{g,j'}^2}}{\sum_g \sum_{j'} N_{g,j'\to j} \left|w_{g,j'}\right|}. \tag{A.63}$$

To advance the temperature to the next time step the iSNB iterative algorithm can be applied replacing the deterministic diffusion equation of SNB with the DDMC version described in this section.

A.2.2 Test Problem

As a test of the DDMC solver an analytic single group test problem was used to test against the MC solution. For this test a simple parabola solution was used

$$H(r) = 1 - \left(\frac{r}{r_{max}}\right)^2. \tag{A.64}$$

Plugging the analytic solution into the LHS of the SNB diffusion equation with constant λ in 1D slab geometry gives a manufactured source term of

$$S(r) = \frac{2\lambda}{r_{max}^2} + \frac{1}{\lambda}\left(1 - \left(\frac{r^2}{r_{max}^2}\right)\right). \tag{A.65}$$

The test problem was run with 10^6 DDMC particles for a domain 200 MFPs wide with cells 5, 10, 20, and 40 MFPs wide. Fig. A.1 shows good agreement between the analytic solution and the DDMC solutions. The error between the analytic solution and the DDMC, shown in Fig. A.2, shows that the relative error is inversely proportional to the number of particles per cell as is expected.

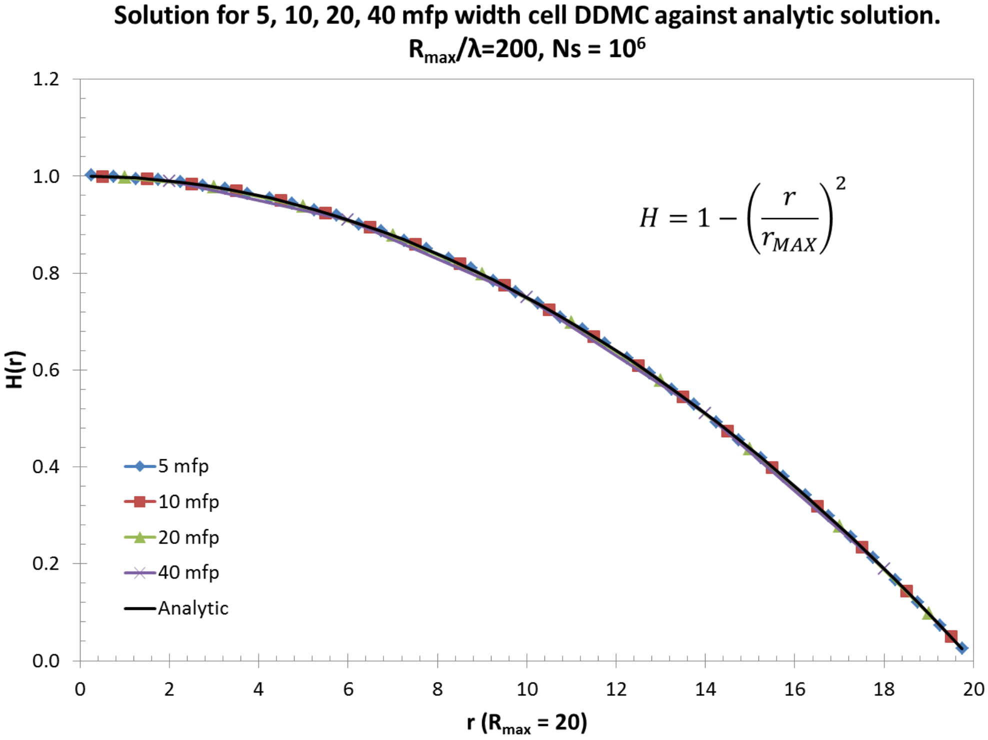

FIGURE A.1: *Comparison of analytic solution to DDMC solution for 5, 10, 20, and 40 MFP wide cells.*

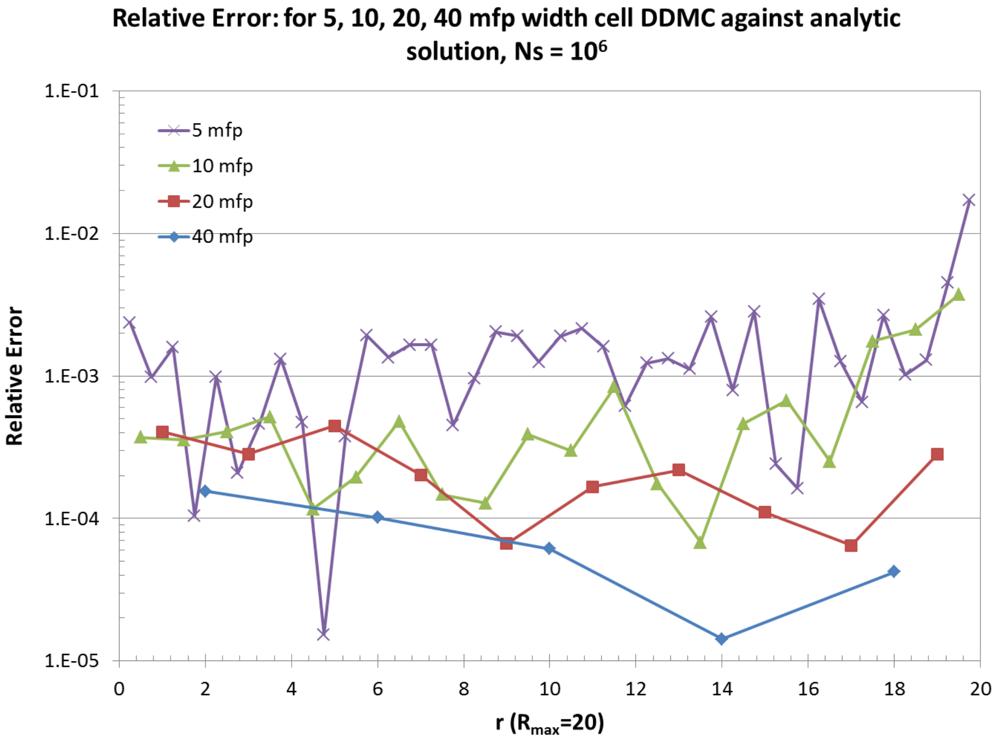

FIGURE A.2: *Error in DDMC method with respect to the analytic solution for parabola test problem. Inverse relationship between number of particles per cell and relative error is shown.*

The DDMC-iSNB algorithm (implemented in a standalone code) was tested against the deterministic iSNB method in DRACO (with hydrodynamics turned off). The problem chosen for testing was a 48 energy group relaxation problem with initial conditions

$$T(r,t=0) = 3000eV \times \exp\left[-\frac{r^2}{2\times(2.47\mu m)^2}\right] + 0.022eV \tag{A.66}$$

with $\rho(r) = 0.1$ g/cm^3, $\bar{z}(r) = 1.0$ and a material of deuterium. The test problem was run to 3 ps and temperature results are plotted in Fig. A.3. DRACO and DDMC results were largely in agreement for the relaxation problem. The minor difference between the two methods were most like caused by the differences in the gridding, DDMC-iSNB uses a 1D spherical mesh whereas DRACO uses a 2D quadrilateral mesh.

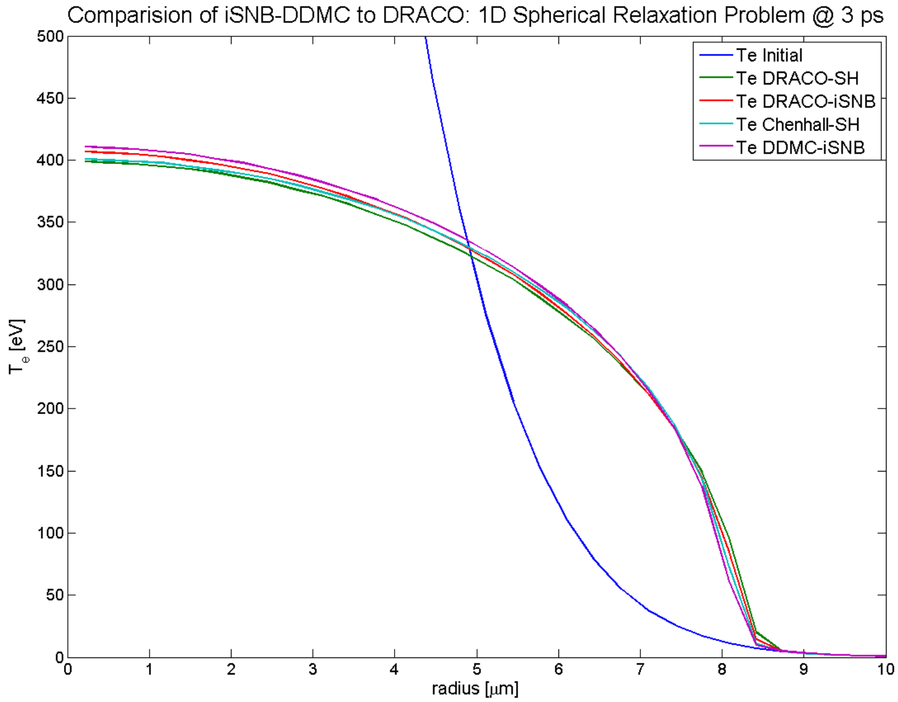

Figure A.3: *Relaxation test problem comparison showing good agreement between iSNB deterministic method in DRACO and DDMC method.*

The MC algorithm was parallelized by allocating an equal number of particles on each thread and doing a gather step of the $\nabla \cdot \mathbf{Q}$ quantity at each iteration. Parallel performance testing was performed on Ignition, a 2 Xenon X5660 processor machine (6 cores/processor). For a test problem of 2×10^6 MCP per time step the simulation showed an inverse relationship between simulation time and the number of threads used Fig. A.4. The inverse relationship indicates good parallel scaling of the MC algorithm.

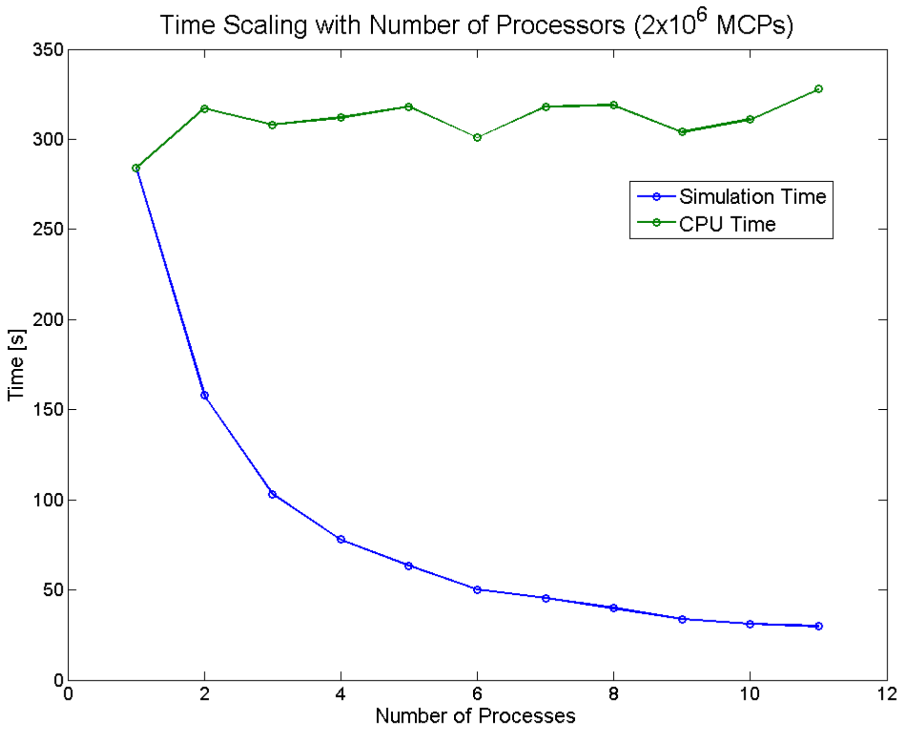

Figure A.4: *Showing inverse relationship between number of processors and simulation run time.*

Appendix B

DP1/P3 Approximation

As a stepping stone between the diffusion and full transport treatments of the electron heat flux a higher order Legendre approximation is used. For this method we began with the double P1 and P3 approximations.

B.1 The 1D Double P1 Approximation

For the double P1 (DP1) approximation the electron distribution function is expanded in 1st order Legendre expansions on each half of the angular interval $\mu = [-1, 1]$:

$$f(x, v, \mu) = \begin{cases} f_0^+(x, v) + 3(2\mu - 1)f_1^+(x, v) & \text{if } \mu > 0 \\ f_0^-(x, v) + 3(2\mu + 1)f_1^-(x, v) & \text{otherwise} \end{cases} \tag{B.1}$$

where the half angle moments can be computed via

$$f_n^{\pm}(x,v) = \pm\int_0^{\pm 1} P_n(2\mu \mp 1) f(x,v,\mu)d\mu. \tag{B.2}$$

By taking the 0^{th} and 1^{st} order half angle moments of the steady state 1D transport equation in slab coordinates

$$v\mu\frac{\partial f}{\partial x} - \mu\frac{eE}{m_e} = C(f) \tag{B.3}$$

a set of four coupled differential equations is produced:

$0^{\mathbf{th}}$ Moments:

$$\left(\frac{\partial}{\partial x} - \frac{eE}{m_e v}\frac{\partial}{\partial v}\right)\left(f_0^+ + f_1^+\right) + 2\Sigma_T f_0^+ = \Sigma_{S,0}f_0 + \frac{3}{2}\Sigma_{S,1}f_1 - \frac{7}{8}\Sigma_{S,3}f_3 \tag{B.4}$$

$$\left(\frac{\partial}{\partial x} - \frac{eE}{m_e v}\frac{\partial}{\partial v}\right)\left(-f_0^- + f_1^-\right) + 2\Sigma_T f_0^- = \Sigma_{S,0}f_0 - \frac{3}{2}\Sigma_{S,1}f_1 + \frac{7}{8}\Sigma_{S,3}f_3 \tag{B.5}$$

$1^{\mathbf{st}}$ Moments:

$$\left(\frac{\partial}{\partial x} - \frac{eE}{m_e v}\frac{\partial}{\partial v}\right)\left(\frac{f_0^+}{3} + f_1^+\right) + 2\Sigma_T f_1^+ = \frac{1}{2}\Sigma_{S,1}f_1 + \frac{5}{4}\Sigma_{S,2}f_2 + \frac{7}{8}\Sigma_{S,3}f_3 \tag{B.6}$$

$$\left(\frac{\partial}{\partial x} - \frac{eE}{m_e v}\frac{\partial}{\partial v}\right)\left(\frac{f_0^-}{3} - f_1^-\right) + 2\Sigma_T f_1^- = \frac{1}{2}\Sigma_{S,1}f_1 - \frac{5}{4}\Sigma_{S,2}f_2 + \frac{7}{8}\Sigma_{S,3}f_3 \tag{B.7}$$

The collision operator and its coefficients have been kept in terms of the full angular moments, which can be related to the half angular moments [36] via

$$f_0 = f_0^+ + f_0^- \tag{B.8}$$

$$f_1 = \frac{1}{2}\left(f_0^+ - f_0^-\right) + \frac{1}{2}\left(f_1^+ + f_1^-\right) \tag{B.9}$$

$$f_2 = \frac{3}{4}\left(f_1^+ - f_1^-\right) \tag{B.10}$$

$$f_3 = \frac{1}{8}\left(f_0^+ - f_0^-\right) + \frac{3}{8}\left(f_1^+ + f_1^-\right). \tag{B.11}$$

By taking a linear combination of the half angular moments a set of full angular moment equations is derived

$$\left(\frac{\partial}{\partial x} - \frac{eE}{m_e v}\frac{\partial}{\partial v}\right) f_1 = -\Sigma_a f_0 \tag{B.12}$$

$$\frac{1}{3}\left(\frac{\partial}{\partial x} - \frac{eE}{m_e v}\frac{\partial}{\partial v}\right)(f_0 + 2f_2) = -\Sigma_1 f_1 \tag{B.13}$$

$$\frac{2}{15}\left(\frac{\partial}{\partial x} - \frac{eE}{m_e v}\frac{\partial}{\partial v}\right)(3f_1 + 4f_3) = -\Sigma_2 f_2 \tag{B.14}$$

$$\frac{1}{3}\left(\frac{\partial}{\partial x} - \frac{eE}{m_e v}\frac{\partial}{\partial v}\right) f_2 = -\Sigma_3 f_3 \tag{B.15}$$

where

$$\Sigma_1 = \Sigma_T - \Sigma_{S,1}, \quad \Sigma_2 = \frac{16}{15}\Sigma_T - \Sigma_{S,2}, \quad \Sigma_3 = 2\Sigma_T - \frac{7}{8}\Sigma_{S,3}. \tag{B.16}$$

The system of equations F is solved via Newton's method similarly to the SNB method.

$$\left[\frac{\partial F}{\partial X}\right]_n \Delta X_n = -F(X_n) \tag{B.17}$$

where

$$F_0(f_0, f_1, f_2, f_3, E) = 0 = \left(\frac{\partial}{\partial x} - \frac{eE}{m_e v}\frac{\partial}{\partial v}\right) f_1 + \Sigma_a f_0 \tag{B.18}$$

$$F_1(f_0, f_1, f_2, f_3, E) = 0 = \frac{1}{3}\left(\frac{\partial}{\partial x} - \frac{eE}{m_e v}\frac{\partial}{\partial v}\right)(f_0 + 2f_2) + \Sigma_1 f_1 \tag{B.19}$$

$$F_2(f_0, f_1, f_2, f_3, E) = 0 = \frac{2}{15}\left(\frac{\partial}{\partial x} - \frac{eE}{m_e v}\frac{\partial}{\partial v}\right)(3f_1 + 4f_3) + \Sigma_2 f_2 \tag{B.20}$$

$$F_3(f_0, f_1, f_2, f_3, E) = 0 = \frac{1}{3}\left(\frac{\partial}{\partial x} - \frac{eE}{m_e v}\frac{\partial}{\partial v}\right) f_2 + \Sigma_3 f_3 \tag{B.21}$$

Computing the Jacobian $(\partial F/\partial X)$ and suppressing the electric field terms due to magnitude considerations gives

$$\frac{\partial F}{\partial X} = \begin{bmatrix} -\Sigma_a & -\frac{\partial}{\partial x}() & 0 & 0 \\ -\frac{1}{3}\frac{\partial}{\partial x}() & -\Sigma_1 & -\frac{2}{3}\frac{\partial}{\partial x} & 0 \\ 0 & -\frac{2}{5}\frac{\partial}{\partial x}() & -\Sigma_2 & -\frac{8}{15}\frac{\partial}{\partial x}() \\ 0 & 0 & -\frac{1}{3}\frac{\partial}{\partial x}() & -\Sigma_3 \end{bmatrix}. \tag{B.22}$$

For the initial guess we use the first order result produced by SH theory with higher order terms set equal to zero

$$X_0 = \begin{bmatrix} f_0^{mb} \\ f_1^{mb} \\ 0 \\ 0 \end{bmatrix}. \tag{B.23}$$

The residual term is

$$F(X_0) = \begin{bmatrix} -\frac{\partial f_1^{mb}}{\partial x} + \frac{eE^{mb}}{mv^3}\frac{\partial(v^2 f_1^{mb})}{\partial v} \\ 0 \\ -\frac{2}{5}\frac{\partial f_1^{mb}}{\partial x} + \frac{2}{5}\frac{eE^{mb}}{mv^3}\frac{\partial(v^2 f_1^{mb})}{\partial v} \\ 0 \end{bmatrix}. \tag{B.24}$$

Putting everything together gives

$$\frac{\partial \Delta f_1}{\partial x} + \Sigma_a \Delta f_0 = -\frac{\partial f_1^{mb}}{\partial x} + \frac{eE^{mb}}{mv^3} \cdot \frac{\partial(v^2 f_1^{mb})}{\partial v}, \tag{B.25}$$

$$\frac{1}{3}\frac{\partial}{\partial x}(\Delta f_0 + 2\Delta f_2) + \Sigma_1 \Delta f_1 = 0, \tag{B.26}$$

$$\frac{2}{15}\frac{\partial}{\partial x}(3\Delta f_1 + 4\Delta f_3) + \Sigma_2 \Delta f_2 = -\frac{2}{5}\frac{\partial f_1^{mb}}{\partial x} + \frac{2}{5}\frac{eE^{mb}}{mv^3} \cdot \frac{\partial(v^2 f_1^{mb})}{\partial v}, \tag{B.27}$$

$$\frac{1}{3}\frac{\partial \Delta f_2}{\partial x} + \Sigma_3 \Delta f_3 = 0. \tag{B.28}$$

By solving Eqs. B.26 and B.28 for Δf_1 and Δf_3 respectively and plugging into Eqs. B.26 and B.28 gives a pair of coupled diffusion in equations

$$\left[\frac{1}{\lambda(v)} - \nabla\frac{\lambda'(v)}{3}\nabla\right]\left(\frac{m_e}{2}v^5[\Delta f_0 + 2\Delta f_2]\right) = -\frac{m_e}{2}\frac{\partial(v^5 f_1^{mb})}{\partial x} + \frac{eE^{mb}}{2}v^2\frac{\partial(v^2 f_1^{mb})}{\partial v} + \frac{2\left(\frac{m_e}{2}v^5\Delta f_2\right)}{\lambda(v)}, \tag{B.29}$$

$$\left[\frac{1}{\lambda_2(v)} - \nabla\frac{\lambda_3'(v)}{3}\nabla\right]\left(\frac{m_e}{2}v^5\Delta f_2\right) = \frac{3}{4}\frac{\left(\frac{m_e}{2}v^5[\Delta f_0 + 2\Delta f_2]\right)}{\lambda(v)}. \tag{B.30}$$

Putting the diffusion equations in multigroup form and collecting terms gives

$$\left(\frac{1}{\lambda_g(x)} - \nabla\frac{\lambda_g'(x)}{3}\nabla\right)H_g(x) = -\nabla U_g(x) + \frac{2K_g(x)}{\lambda_g(x)}, \tag{B.31}$$

$$\left(\frac{1}{\lambda_{2,g}(x)} - \nabla\frac{\lambda_{3,g}'(x)}{3}\nabla\right)K_g(x) = \frac{3}{4}\frac{H_g(x)}{\lambda_g(x)}. \tag{B.32}$$

where

$$H_g = \frac{m_e v^5}{2}(\Delta f_0 + 2\Delta f_2), \tag{B.33}$$

$$K_g = \frac{m_e v^5}{2}(\Delta f_2), \tag{B.34}$$

and the MFPs are given by

$$\frac{1}{\lambda_g} = \frac{\Sigma_{1,g}}{\sqrt{Z}} = \sqrt{Z}\Sigma_{a,g}, \tag{B.35}$$

$$\frac{1}{\lambda_{2,g}} = \sqrt{Z}\left(\frac{3}{2}\Sigma_{a,g} + \frac{15}{8}\Sigma_{2,g}\right), \tag{B.36}$$

$$\frac{1}{\lambda_{3,g}} = \frac{\Sigma_{3,g}}{\sqrt{Z}}. \tag{B.37}$$

The non-local flux divergence is recovered via

$$\nabla \cdot \mathbf{Q}_{nl} = -\sum_g \frac{H_g(x) - 2K_g(x)}{\lambda_g(x)}. \tag{B.38}$$

B.1.1 MFP Treatment

$$\Sigma_S(x,\mu) = \sum_l \frac{(2l+1)}{2} \Sigma_{S,l}(x) P_l(\mu) \tag{B.39}$$

On λ_2 and λ_3 assuming a delta scattering term the following limits are imposed:

$$\lambda_2 < \frac{15}{16}\lambda_0, \tag{B.40}$$

$$\lambda_3 < \frac{1}{2}\lambda_0. \tag{B.41}$$

If instead a P3 approximation is desired:

$$\lambda_2 = \lambda_0, \tag{B.42}$$

$$\lambda_3 = \frac{81}{56}\lambda_0. \tag{B.43}$$

B.2 Curved Geometry P3

In spherical geometry the P3 equations are

$$\left[\frac{\partial}{\partial r} + \frac{2}{r}\right] f_1 + \sigma_0 f_0 = S_0, \tag{B.44}$$

$$\frac{2}{3}\left[\frac{\partial}{\partial r} + \frac{3}{r}\right] f_2 + \frac{1}{3}\frac{\partial f_0,}{\partial r} + \sigma_1 f_1 = 0 \tag{B.45}$$

$$\frac{3}{5}\left[\frac{\partial}{\partial r}+\frac{4}{r}\right] f_3+\frac{2}{5}\left[\frac{\partial}{\partial r}-\frac{1}{r}\right] f_1+\sigma_2 f_2=S_2, \tag{B.46}$$

$$\frac{3}{7}\left[\frac{\partial}{\partial r}-\frac{2}{r}\right] f_2+\sigma_3 f_3=0. \tag{B.47}$$

By solving the P3 equations for the odd moments and eliminating, a coupled set of second order equations is derived:

$$\left[\frac{1}{\lambda_0}-\frac{1}{r^2}\frac{\partial}{\partial r}\left(\lambda_1 r^2\frac{\partial}{\partial r}\right)\right] f_0=-\nabla U+2\frac{1}{r^2}\left[\frac{\partial}{\partial r}\left(\lambda_1 r^2\left(\frac{\partial}{\partial r}+\frac{3}{r}\right)\right)\right] f_2, \tag{B.48}$$

$$-\frac{3}{5}\left[\frac{\partial}{\partial r}+\frac{4}{r}\right]\lambda_3\frac{3}{7}\left[\frac{\partial}{\partial r}-\frac{2}{r}\right] f_2-\frac{2}{5}\left[\frac{\partial}{\partial r}-\frac{1}{r}\right]\left(\lambda_0\frac{2}{3}\left[\frac{\partial}{\partial r}+\frac{3}{r}\right] f_2+\frac{1}{3}\frac{\partial f_0}{\partial r}\right)+\sigma_2 f_2=S_2. \tag{B.49}$$

While in one dimension the P3 approximation is able to be simplified into a coupled set of two equations, in multiple dimensions the solution is more complicated. In particular, for P3 in RZ-cylindrical geometry there are 10 first order equations which can be reduced to four coupled second order equations. The interplay of four coupled equations combined with the issues of a discretion on a 2D mesh make a pure P3 method undesirable. As such, a simplified method, discussed in the next section, is used instead.

B.3 Simplified P3 Method

The simplified P_N (SPN) method originally developed by Gelbard in the 1960s is a second asymptotic correction to the P_1 equation [37][38][39]. The SPN method involves taking the 1D slab coordinate P_{2N} equations reduced to N second order equations and replacing the second order operator with the appropriate geometry P_1 diffusion term. Applying this to our

1D slab $\nabla \cdot \mathbf{Q}$ results for 2D cylindrical geometry gives

$$\left(\frac{1}{\lambda_g(r,z)} - \nabla \frac{\lambda'_g(r,z)}{3} \nabla\right) H_g(r,z) = -\nabla U_g(r,z) + \frac{2K_g(r,z)}{\lambda_g(r,z)}, \tag{B.50}$$

$$\left(\frac{1}{\lambda_{2,g}(r,z)} - \nabla \frac{\lambda'_{3,g}(r,z)}{3} \nabla\right) K_g(r,z) = \frac{3}{4}\frac{H_g(r,z)}{\lambda_g(r,z)} \tag{B.51}$$

where

$$\nabla_{r,z}\left(\frac{\lambda_n(r,z)}{3}\nabla_{r,z}\cdot\right) = \frac{1}{r}\frac{\partial}{\partial r}\left(r\frac{\lambda_n(r,z)}{3}\frac{\partial}{\partial r}\cdot\right) + \frac{\partial}{\partial z}\left(\frac{\lambda_n(r,z)}{3}\frac{\partial}{\partial z}\cdot\right) \tag{B.52}$$

and

$$\lambda_{2,g}(r,z) \approx \frac{8}{27}\lambda_g(r,z), \tag{B.53}$$

$$\lambda_{3,g}(r,z) \approx \frac{81}{56}\lambda_g(r,z). \tag{B.54}$$

This gives an SP_3 approximation to our earlier P_3 results. The advantage to this approximation is that there are only two coupled equations to solve and the P_1 diffusion operator discretization can be used for both equations. As such the code implementation is sped up due to reuse of components from the existing P_1 (SNB) code.

B.4 Comparison to iSNB

The SP_3 method has been implemented in the 1D LILAC multiphysics code. The SP_3 method is compared to the Goncharov and iSNB non-local methods. The three models are compared for Omega shot 60303 simulation (see Section 4.1.1). The heat flux divergence magnitudes are compared at 2400ps, just prior to the second shock convergence, in Fig. B.1. In comparison to the iSNB method the SP_3 method produces a greater amount of preheating and slightly more flux limiting behavior. The Goncharov model is considered to get the best 1D results for the 60303 simulation and displays less preheating than the iSNB model. Since the SP_3 method produces more preheating than both the iSNB and the more accurate Goncharov methods, it appears that going to higher angular alone may not be sufficient for better predictive capability. One possible cause for this is that diffusion type methods produce exponentially decaying results whereas the Goncharov transport model uses a finite range.

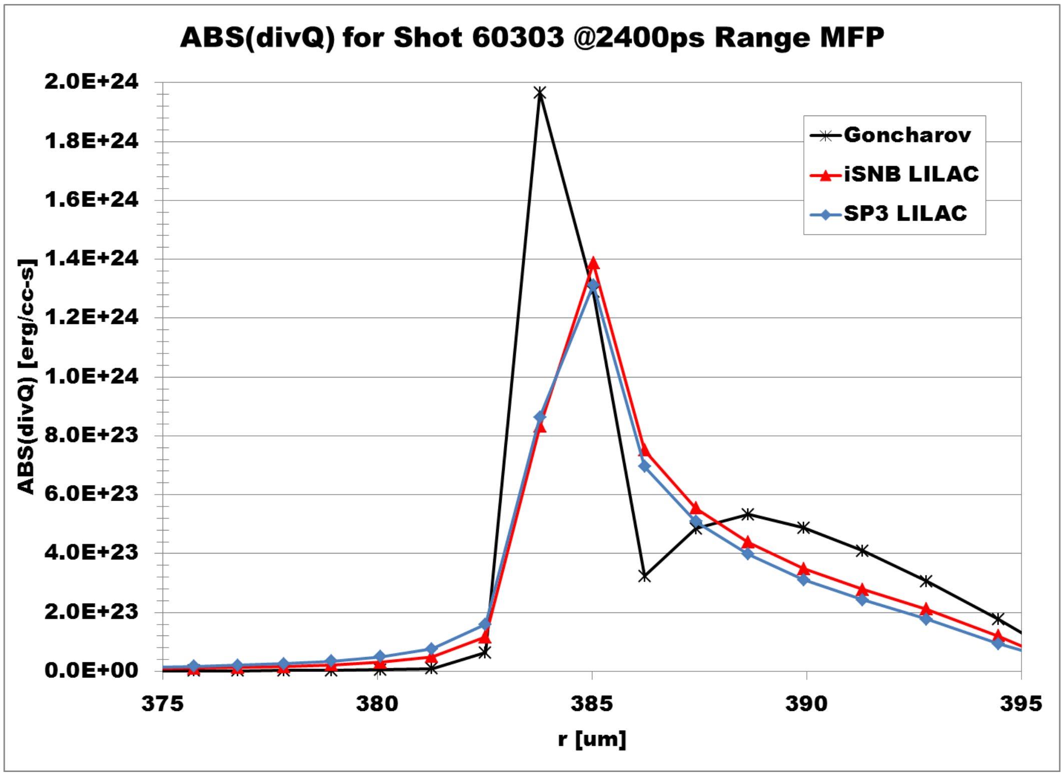

FIGURE B.1: *Heat flux magnitude comparison for Goncharov, iSNB, and* SP_3 *models in LILAC for Omega shot 60303 at 2400ps.*